# CHAPTER 3: EXPERIMENTAL PROGRAM AND DATA

This chapter provides information on the different types of bulk material used in the fluidised dense phase pneumatic conveying testing and the methods used in characterising the bulk material using basic parameter methods and air-particle characterisation methods. Also detailed are the pipeline configurations and instrumentation used in the conveying trials along with the methods used in calibrating the instrumentation.

Conveying trials were conducted on three different materials (Cement Meal, Flyash and Alumina) to initially determine their steady state fluidised dense phase capabilities with respect to the total pipeline pressure drop ($\Delta P$), the solids mass flow rate ($m_s$) and the conveying air mass flow rate ($m_a$). To obtain a larger range of fluidised dense phase data, the pneumatic conveying results for $\Delta P$, $m_s$ and $m_a$ were also analysed from the work conducted by Jones during his PhD dissertation [18] and are presented at the end of this chapter.

## *3.1 Bulk Material Testing Methods*

Basic parameter, air-particle parameter and flow property tests of each bulk material were conducted to determine their values and behaviours for later analysis. The specific parameter values for each bulk material are detailed in Chapter 3.2 with the methods used for determining these values detailed below.

### 3.1.1 Basic parameter test methods

The testing of the three fluidised capable bulk material consisted of determining basic particle parameters for each material were:

1. **mean particle diameter** – as the bulk materials were fine powders (<1000 $\mu$m), the size distribution was determined via laser diffraction and as such, the mean particle size was determined from a volumetric basis. A total of four size distribution tests were conducted on each material with the average size distribution presented in Chapter 3.2.

2. **particle density –** the particle density was determined via an air displacement pycnometer. Six readings were taken for each material with the average density determined.

3. **bulk density –** the measurement for bulk density varied and depended specifically on the volume that the bulk material occupied divided by its mass, i.e.:

   a. **'loose poured' –** a single value determined from the volume of material poured into a container. Basically, material was gently poured into a 500ml glass column at an angle of approximately 30 degrees to the horizontal. Care was taken not to compact the material and the glass column was place in the vertical position. The volume was determined from a graduated scale on the side of the column. This volume was then divided by the known mass of material to determine its bulk density. This process was repeated 3 times with the average result defining the 'loose poured' bulk density for each material.

   **b. 'tapped' –** On completion of each 'loose poured' bulk density test, the material was lightly 'tapped' using a small rubber mallet until no further reduction in material volume was observed. The 'tapped' volume of material was divided by the known weight to obtain a bulk density value. The process was also completed 3 times with the average value defining the 'tapped' bulk density for each material.

   **c. 'consolidated' –** this bulk density can vary as it is dependant on the amount of load place on the material. Generally a normal pressure is applied to the bulk material during flow property testing with the bulk density relationship to normal pressure plotted graphically. The results of the consolidated bulk density for each material can be seen in Appendix B.

**4. Hausner Ratio (*HR*) –** a single value which represents the potential compaction from the loose poured state of the material due to tapping and is defined as:

$$HR = 1 - \frac{\rho_{blp}}{\rho_{bt}} \tag{3.1}$$

5. **voidage ($\varepsilon$) –** a single parameter value that represents the interstitial voids within the bulk material and for air at ambient conditions can be approximated as:

$$\varepsilon = 1 - \frac{\rho_b}{\rho_s} \tag{3.2}$$

### 3.1.2 Air-particle parameter test methods

The air-particle parameters were measured via fluidisation and de-aeration tests using a 0.155 m ID Chamber (Figure 23). The superficial gas velocity was measured via a series of rotameters (Figure 24), with the associated pressure drop for each superficial gas setting measured via a Furness FC-001 micro-manometer. The bulk material bed height was determined from a vertical length scale located on the side of the chamber. The basic methods used in conducting these air-particle tests were as follows:

1. **fluidisation –** The superficial gas velocity was manually adjusted via an air speed controller and was increased in regular increments from zero to a velocity approximately twice the value of the minimum fluidisation velocity. The superficial gas velocity was then reduced in the same increments to zero. The steady state pressure drop and bed height were recorded for each superficial gas setting. This testing provided information on the permeability value and steady state fluidisation pressure.

2. **de-aeration –** The superficial gas velocity was increased so that the steady state pressure was achieved. The airflow was then stopped via a quick (< 1 second) shut-off valve and the pressure reading was recorded. This testing provided the de-aeration behaviour for the bulk material based on a pressure decay analysis.

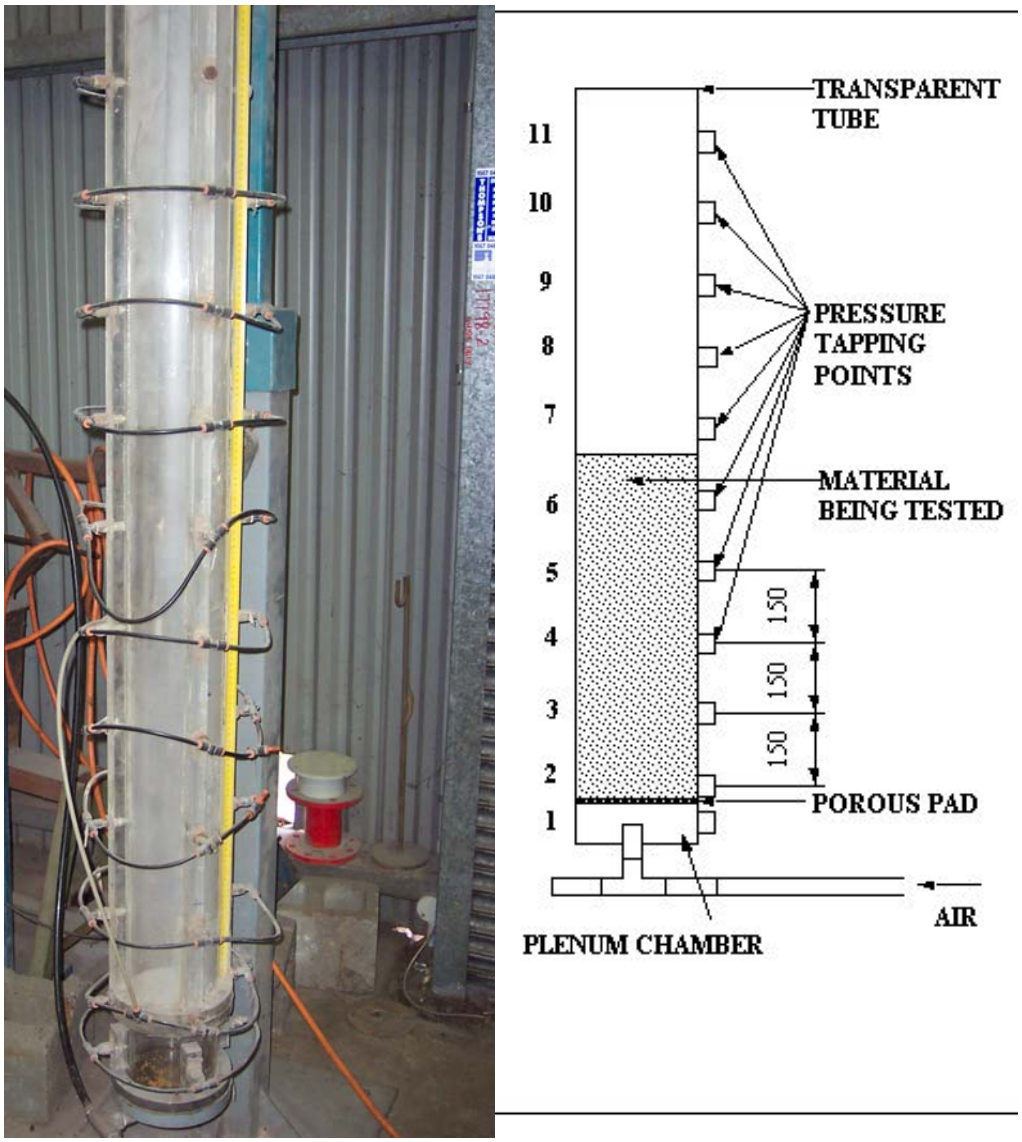


Figure 23, picture and schematic of 0.155m ID chamber used for the fluidisation and de-aeration tests


Figure 24, rotameters used in fluidisation tests

### 3.1.3 Flow property tests

Generally the consolidated stress states for a bulk material can be defined by applying the results of flow property tests utilising the yield loci of the Mohr-coulomb relationship. This approach to stress state analysis has been successfully used in bin flow analysis and design [42] and defines the stress state of a bulk material through its normal and shear stress behaviour within a shear cell. The Flow property tests conducted utilised the linear shear testing system originally designed by Jenike. Basically, Jenike’s system uses two circular rings which contain the bulk material with a normal load placed on the top of the rings. A lateral force is then applied to the top ring and the steady state shear stress response of the material is measured. These shear

tests subsequently defined the ‘consolidated’ bulk density, internal friction ($\delta$) and flow function (ff) of the bulk material.

Wall shear tests were also conducted to determine the wall friction angle on mill scale mild steel (MSMS) which defined the wall friction angle relationship of the bulk material with consolidation load. The wall shear tests used a similar system to the internal friction shear tests except that the base ring was removed and the mild steel plate was placed under the top ring prior to the start of the tests. A special thank you must be extended to TUNRA Bulk Solids at the University of Newcastle for conducting the flow property and wall shear tests.

## *3.2 Bulk Material Data*

The parameters of the three bulk materials used in the conveying tests are detailed in the following sub-chapters. Generally, the Cement Meal was in a degraded state and showed no significant reduction in size distribution or mean particle diameter during the tests. However, the Flyash and Alumina were initially in the ‘as supplied’ state and, as such, were used in a smaller number of conveying trials so that the reduction of mean particle diameter due to product degradation was less than 10% from the original value. The variation in mean particle size was determined from laser diffraction of a sample of material used in the conveying tests.

The fluidisation and de-aeration test plots, in conjunction with the flow property graphs for each of the bulk material, are shown in Appendix B. The de-aeration method as defined by Mainwaring and Reed [24] in Equation 2.15 was used to determine the de-aeration value. The data for the flow property results were determined from the flow property graphs (Appendix B) at approximately a zero normal stress condition.

### 3.2.1 Cement Meal

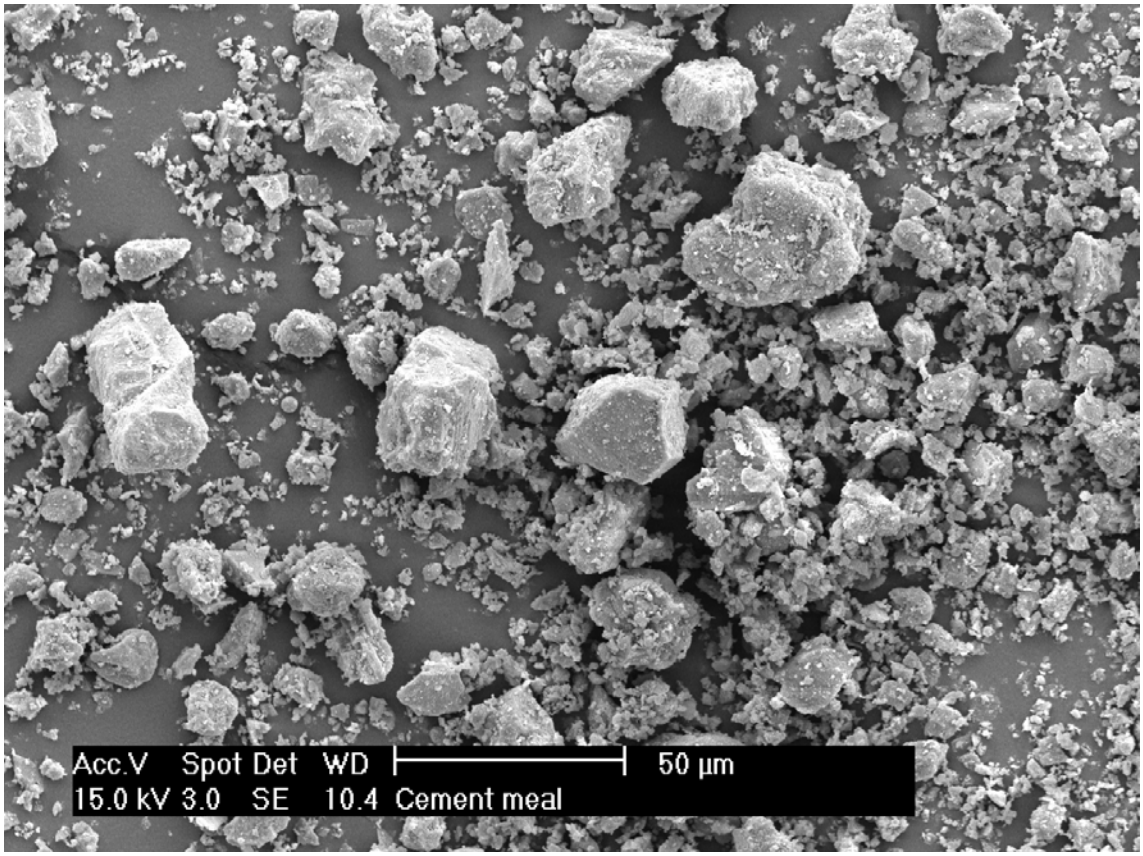


Figure 25, SEM picture of the 'degraded' Cement Meal

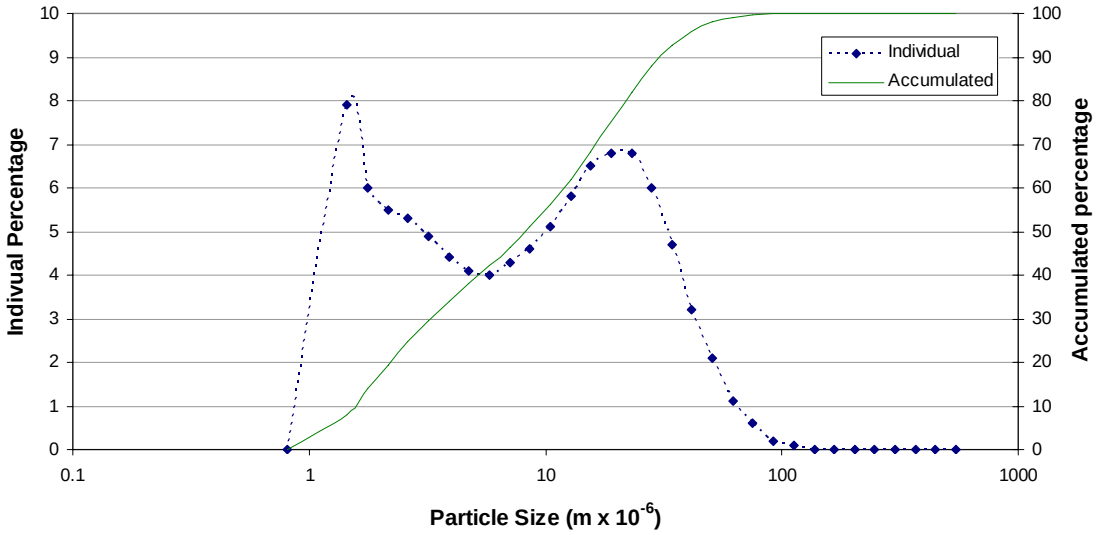


Figure 26, size distribution analysis of 'degraded' Cement Meal

The scanning electron microscope (SEM) picture of the Cement Meal (Figure 25) supports the general assumption that this material was degraded prior to the start of the conveying trials, as the particles display worn rounded edges. Generally, the Cement Meal shape is polygonic in nature with a significant number of finer particles present. The Cement Meal size distribution (Figure 26) shows a bi-model structure which is also indicative of the large amount of fine particles displayed in the SEM picture. The Cement Meal is a Geldart 'C' type powder and minor channelling was observed during the initial bed expansion during the 'increasing airflow' fluidisation tests. As the airflow was increased, the formed channels collapsed and the material subsequently exhibited homogenous fluidisation behaviour. The Cement Meal de-aeration value indicates that this material has a high air retention capability with its permeability value being in the low range. As expected, the basic and air-particle parameters of the Cement Meal places this material in the 'fluidised dense phase' region in all the diagrams discussed in Chapter 2. The Cement Meal parameters were:

| | | | | |
|---|---|---|---|---|
| *Average particle diameter* | $d_p$ | = | $11 \times 10^{-6}$ | *m* |
| *Particle Density* | $\rho_s$ | = | *3000* | $kg/m^3$ |
| *'Tapped' Bulk Density* | $\rho_{bt}$ | = | *1390* | $kg/m^3$ |
| *'Loose Poured' Bulk Density* | $\rho_{bl}$ | = | *930* | $kg/m^3$ |
| *Hausner Ratio* | *HR* | = | *1.49* | - |
| *'Loose Poured' Voidage* | $\varepsilon_{bl}$ | = | *0.690* | - |
| *Permeability* | $\Psi$ | = | $0.08 \times 10^{-6}$ | $m^3$ *s/kg* |
| *De-aeration* | $A_F$ | = | *13* | *kPa s/m* |
| *'Steady State' Fluidisation Pressure* | $\Delta P_{ss}/L$ | = | *8.5* | *kPa/m* |
| *Minimum Fluidisation Velocity* | $v_{mf}$ | = | $32 \times 10^{-3}$ | *m/s* |
| *Wall friction angle* | $\phi_w$ | = | *31 ° (at 0.5 kPa normal load)* | |
| | | = | *24 ° (at 4.0 kPa normal load)* | |
| *Effective Angle of Internal friction* | $\delta$ | = | *47 ° (at 4.0 kPa normal load)* | |

### 3.2.2 Flyash

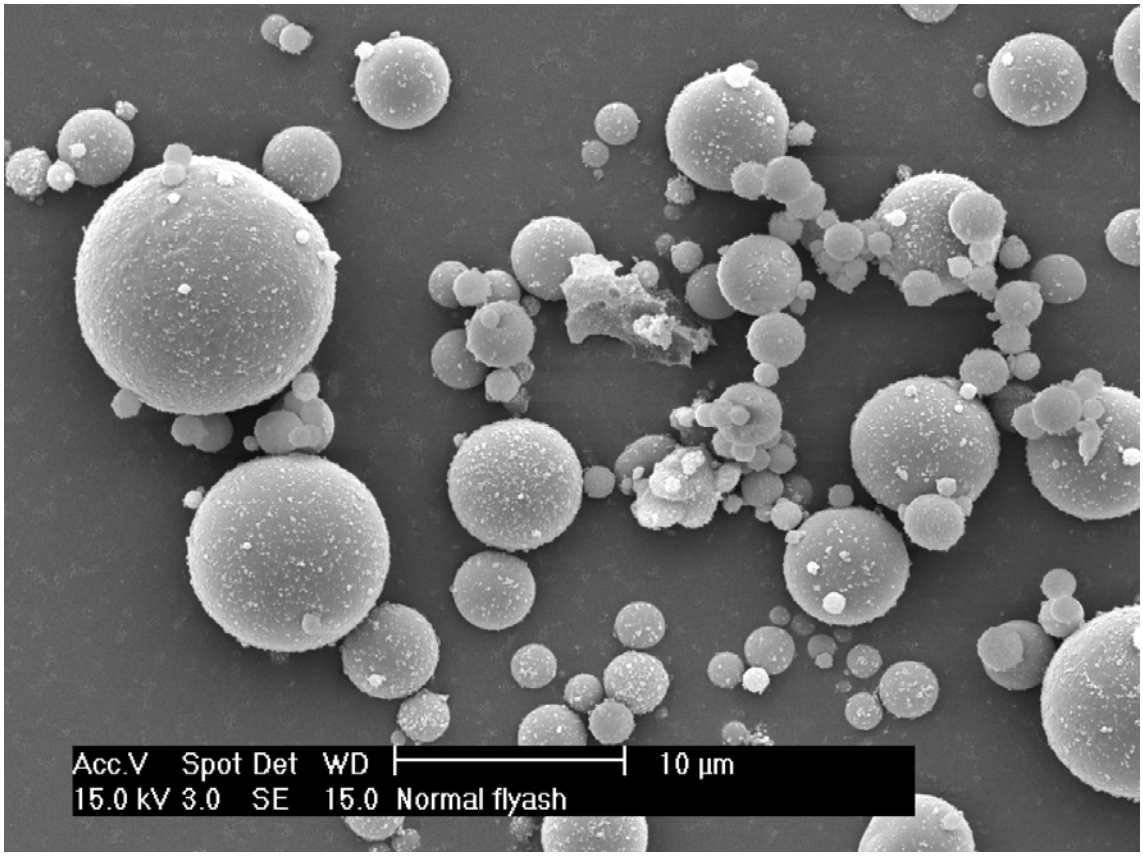


Figure 27, SEM picture of 'as supplied' Flyash

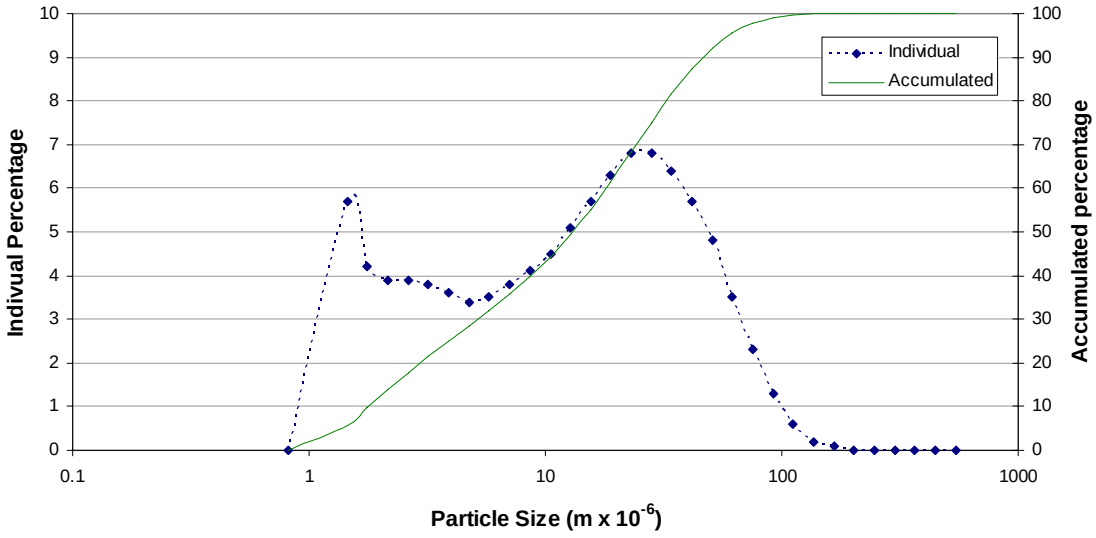


Figure 28, size distribution analysis of 'as supplied' Flyash

Generally, the parameters of the Flyash were similar to the Cement Meal except that the shape was spherical rather than polygonic. The SEM picture of the Flyash (Figure 27) shows the natural sphericity associated with the formation of this coal combustion by-product. The Flyash size distribution (Figure 28) also shows a bi-model structure which is associated with finer particles displayed in the SEM picture. The Flyash is a Geldart 'C' type powder with major channelling occurring during the initial stages of the fluidisation tests. 'Tapping' on the chamber during the fluidisation tests was required to break down the channelling. The major parameters of permeability, minimum fluidisation velocity and steady state fluidisation pressure were determined from regions of the fluidisation tests unaffected by the channelling. As expected, the basic and air-particle parameters of the Flyash also placed this material in the 'fluidised dense phase' region in all the diagrams discussed in Chapter 2. The Flyash parameters were:

| | | | | |
|---|---|---|---|---|
| *Average particle diameter* | $d_p$ | = | $19 \times 10^{-6}$ | *m* |
| *Particle Density* | $\rho_s$ | = | *2530* | $kg/m^3$ |
| *'Tapped' Bulk Density* | $\rho_{bt}$ | = | *1180* | $kg/m^3$ |
| *'Loose Poured' Bulk Density* | $\rho_{blp}$ | = | *810* | $kg/m^3$ |
| *Hausner Ratio* | *HR* | = | *1.46* | - |
| *'Loose Poured' Voidage* | $\varepsilon_{blp}$ | = | *0.680* | - |
| *Permeability* | $\Psi$ | = | $0.23 \times 10^{-6}$ | $m^3$ *s/kg* |
| *De-aeration* | $A_F$ | = | *20* | *kPa s/m* |
| *'Steady State' Fluidisation Pressure* | $\Delta P_{ss}/L$ | = | *5.1* | *kPa/m* |
| *Minimum Fluidisation Velocity* | $v_{mf}$ | = | $39 \times 10^{-3}$ | *m/s* |
| *Wall friction angle* | $\phi_w$ | = | *33° (at 0.5 kPa normal load)* | |
| | | = | *27° (at 4.0 kPa normal load)* | |
| *Effective Angle of Internal friction* | $\delta$ | = | *36° (at 4.0 kPa normal load)* | |

### 3.2.3 Alumina

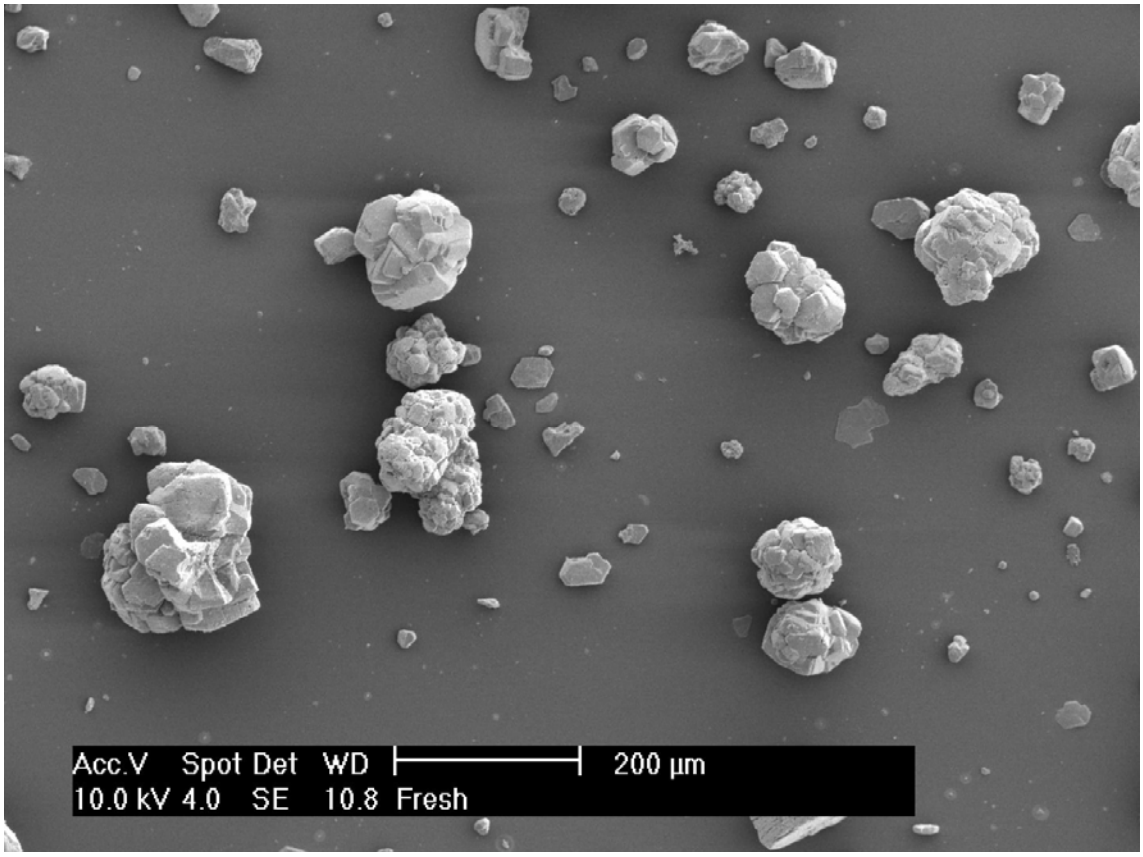


Figure 29, SEM Picture of 'as supplied' Alumina

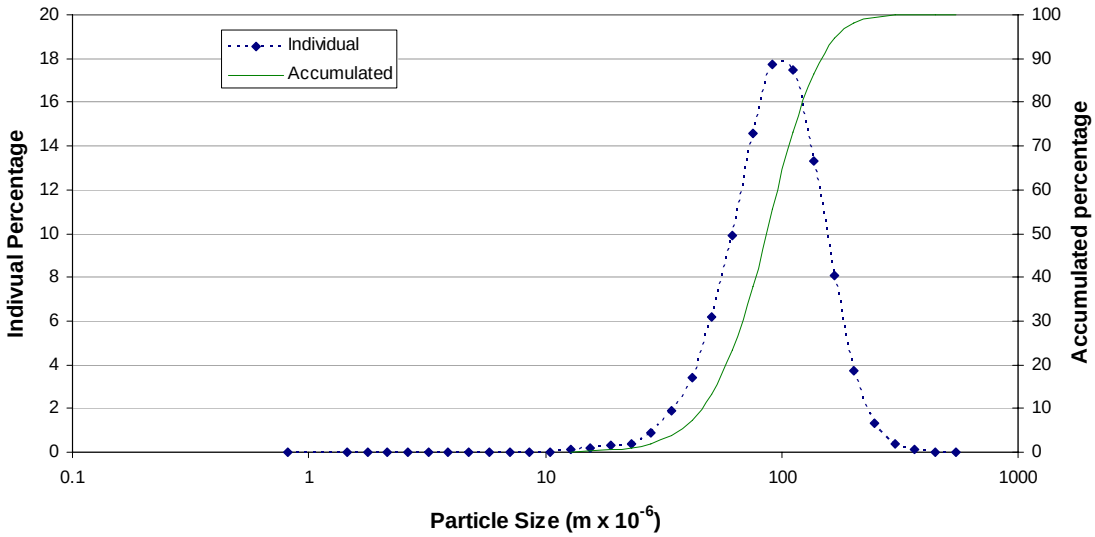


Figure 30, size distribution analysis of 'as supplied' Alumina

The Alumina exhibits a distinct agglomerated form as shown in Figure 29. The Alumina size distribution analysis (Figure 30) shows a single mode structure and a much narrower size distribution when compared to the Cement Meal and Flyash. On the basic material mode of flow diagrams, the prediction of the pneumatic conveying capabilities of this Alumina varies between fluidised dense phase conveying and dilute phase only capable material. It is significant to note that this material was conveyed successfully in a fluidised dense phase flow through a pneumatic conveying system of 53 mm ID pipe with a length of 173 m (lowest average velocity of 5.2 m/s – Chapter 3.3). Also of particular note is that Jones [18] defined a similar Alumina product as Dilute Phase only capable as the material could only be conveyed at an average pipeline velocity greater than 15 m/s (Jones pipeline was 50 m long with a 53 mm ID). The reasons between the different conveying performance is not clearly understood as these products have similar parameters.

| | | | | |
|---|---|---|---|---|
| *Average particle diameter* | $d_p$ | = | $79 \times 10^{-6}$ | *m* |
| *Particle Density* | $\rho_s$ | = | *3300* | $kg/m^3$ |
| *'Tapped' Bulk Density* | $\rho_{bt}$ | = | *1220* | $kg/m^3$ |
| *'Loose Poured' Bulk Density* | $\rho_{blp}$ | = | *1050* | $kg/m^3$ |
| *Hausner Ratio* | *HR* | = | *1.16* | - |
| *'Loose Poured' Voidage* | $\varepsilon_{blp}$ | = | *0.682* | - |
| *Permeability* | $\Psi$ | = | $0.39 \times 10^{-6}$ | $m^3$ *s/kg* |
| *De-aeration* | $A_F$ | = | *1.8* | *kPa s/m* |
| *'Steady State' Fluidisation Pressure* | $\Delta P_{ss}/L$ | = | *8.2* | *kPa/m* |
| *Minimum Fluidisation Velocity* | $v_{mf}$ | = | $13 \times 10^{-3}$ | *m/s* |
| *Wall friction angle* | $\phi_w$ | = | *22° (at 0.5 kPa normal load)* | |
| | | = | *22° (at 4.0 kPa normal load)* | |
| *Effective Angle of Internal friction* | $\delta$ | = | *34° (at 4.0 kPa normal load)* | |

## *3.3 Conveying Tests*

### 3.3.1 Feeding and receiving systems

The conveying tests were conducted utilising a pressurised $1m^3$ blow tank with a top discharge configuration as shown in Figure 31. A two line airflow feeding system was utilised to transport the bulk material with the primary air fluidising and transporting the material from the blow tank. At approximately 2 metres above the pipe feeding point in the blow tank, a lance type configuration provided the access point for the secondary airflow injection. The pressure associated with the primary air (and blow tank) and secondary air injection point was measured utilising pressure transducers which were subsequently recorded via a data acquisition system. The blow tank feeding system also incorporated three load cells on each of the support legs which provided information to the data computer on the mass loss of bulk material from the blow tank.

The bulk material was collected in the receival bin (Figure 31). On the top of the receiving bin was a bag type air filter (max rating 0.2 kg/s airflow) which provided the air separation mechanism. The receiving bin also incorporated 3 load cells on its support legs which measured the bulk material mass gain in the bin. The results of the mass loss from the blow tank and the mass gain from the bin ultimately provided the global solids mass flow rate during each conveying test.

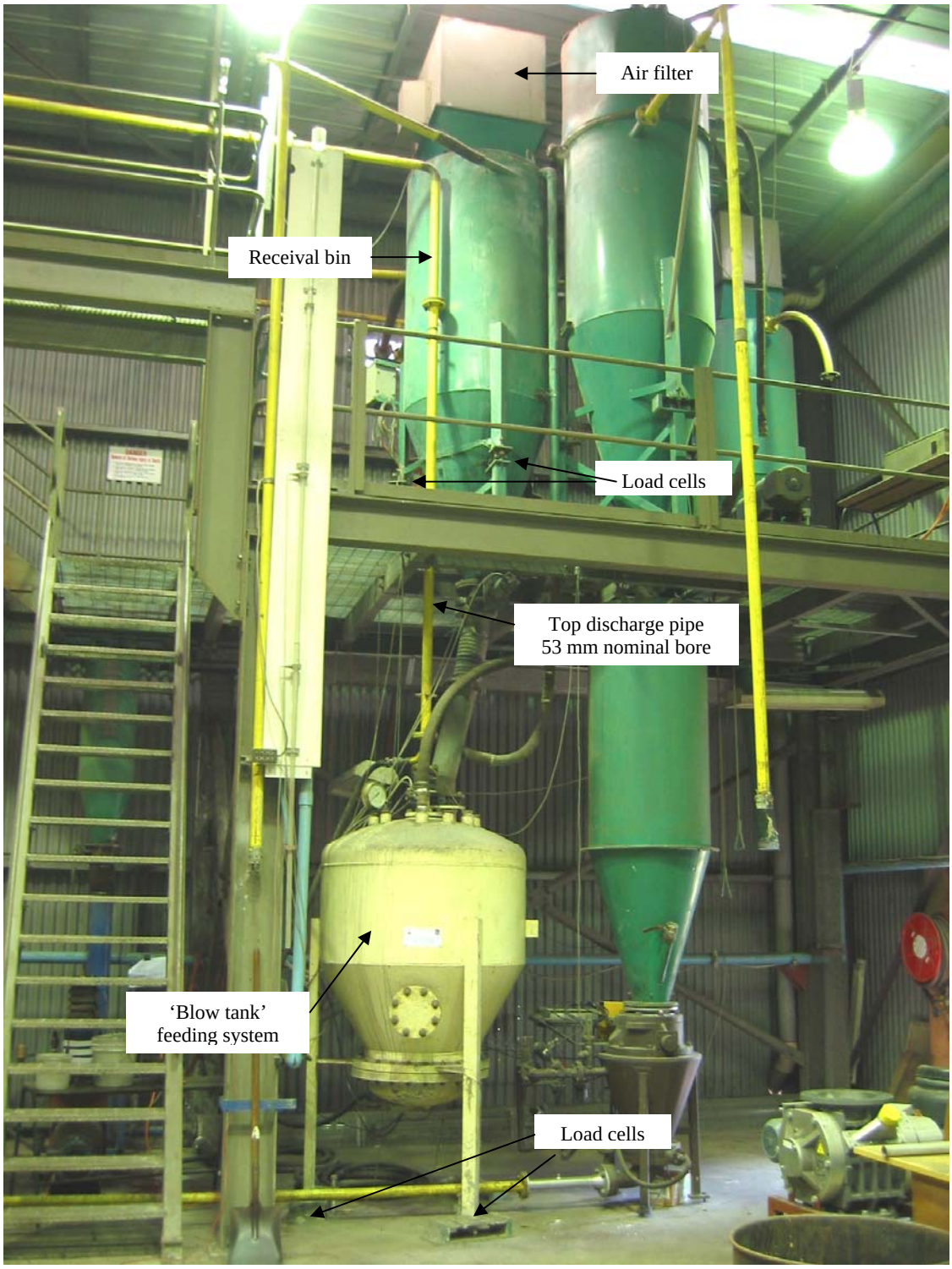


Figure 31, pneumatic conveying feeding and receival systems used in the conveying trials

### 3.3.2 Calibration of instruments

To ensure the information provided to the data acquisition system was accurate, the pressure transducers and load cells where calibrated prior to the conveying tests.

**Load cell calibration –** The calibration consisted of placing known weights on each of the load cells and measuring the resultant voltage. This was repeated for a range of weights (excluding weight of blow tank or receival bin) between 0 and 90 kg for each 3 load cell configuration, as shown in Figure 32. The calibration was completed by utilising the gain and offset values determined from the load cell/voltage plots.

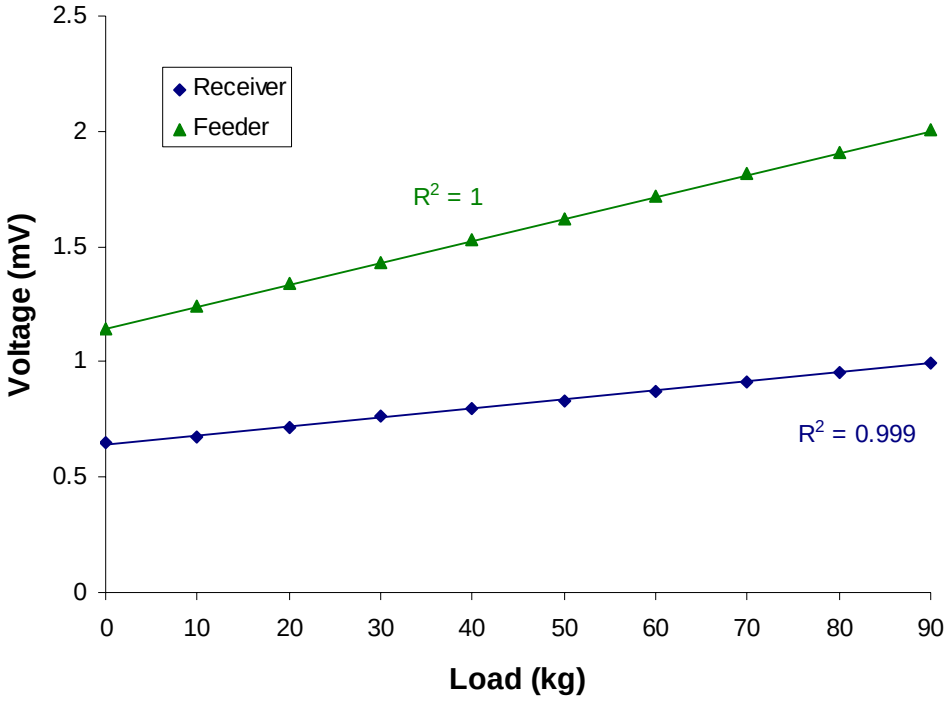


Figure 32, the load cell calibration for the feeding and receiving systems

**pressure transducer calibration –** each pressure transducer was calibrated using a Barnett 'dead weight' tester shown in Figure 33. The calibration technique required each transducer to be screwed to the dead weight tester and any air trapped in the oil was expunged using the screw rotating wheel. Specific weights which correlated to between 0-60 psi in increments of 10 psi were then placed on the dead weight tester and the voltage recorded via the data acquisition system for each individual weight. The average results where then used in the data acquisition program to convert from voltage to kPa. Barksdale 0-100 psi (0-695 kPa) pressure transducers where used during the conveying tests.


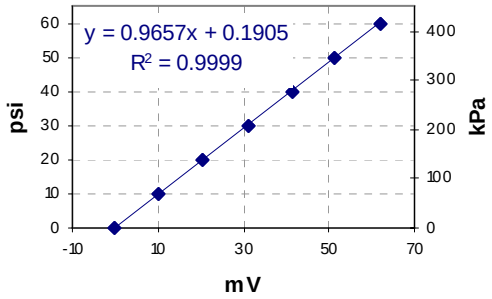


Figure 33, picture of the Barnett 'dead weight' tester used for calibrating the pressure transducers and calibration plot

### 3.3.3 Air mass flow rate calibration

The conveying tests utilised an existing sonic nozzle configuration for delivering a constant air mass flow to the primary and secondary air lines, as shown in Figure 34. The sonic nozzles system consisted of 2 separate arrays of 6 sonic nozzle inputs. The digital configuration of each 6 input channel allowed 63 air mass flow settings to be available per array.

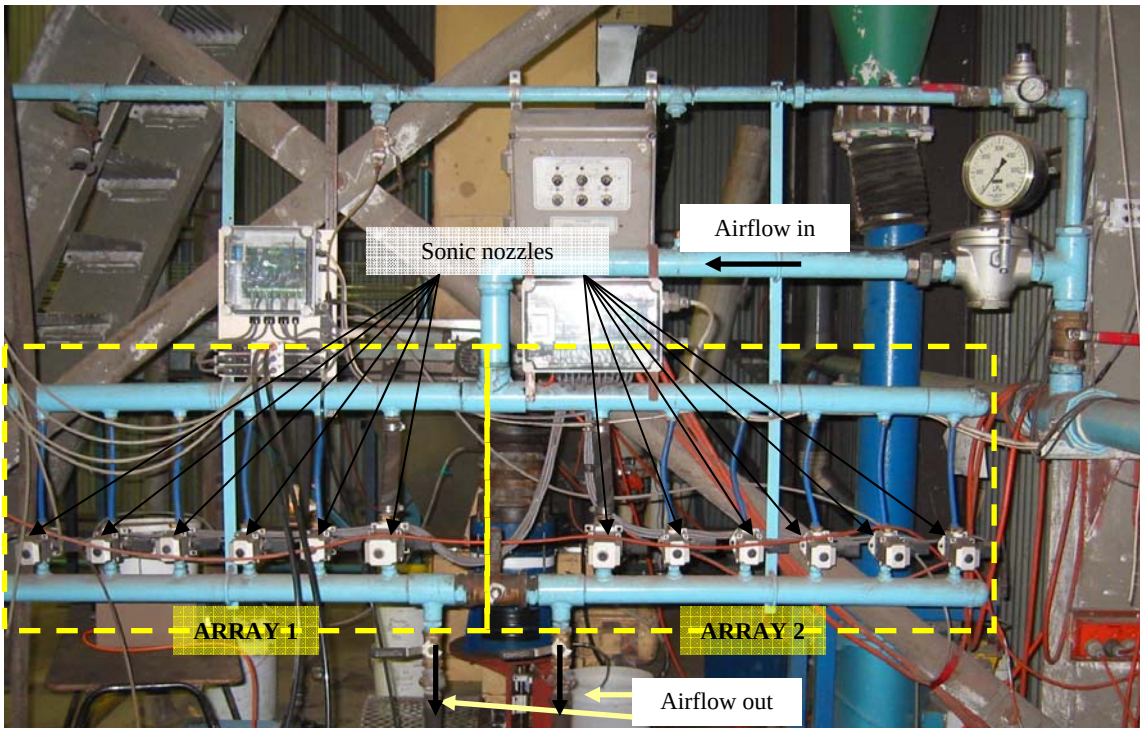


Figure 34, picture of the two sonic nozzle arrays

Prior to the conveying trials, the air mass flow from each sonic nozzle was calculated to ensure that the correct values were used for subsequent modelling. The technique used to calculate the air mass flow rate required a pitot tube to be traversed across a pipe outlet ensuring that the centre of the pipe was in the traverse path. At regular intervals (usually 1 or 2 mm), the difference in pressure between the dynamic pitot tube pressure and static ambient pressure ($\Delta P_{pitot}$) was recorded using a Furness FC-014 micro-manometer at either the 3% scale (0-29.4 Pa) or the 1% scale (0-9.81 Pa). Each streamline air velocity ($v_{a.s}$) calculated using the following dynamic relationship:

$$\Delta P_{pitot} = \frac{1}{2}\rho_a v_{a,s}^2 \tag{3.3}$$

From the pitot tube tests, the velocity profile across the pipe was determined for each array and are shown in Figure 35 for array 1 and Figure 36 for array 2.

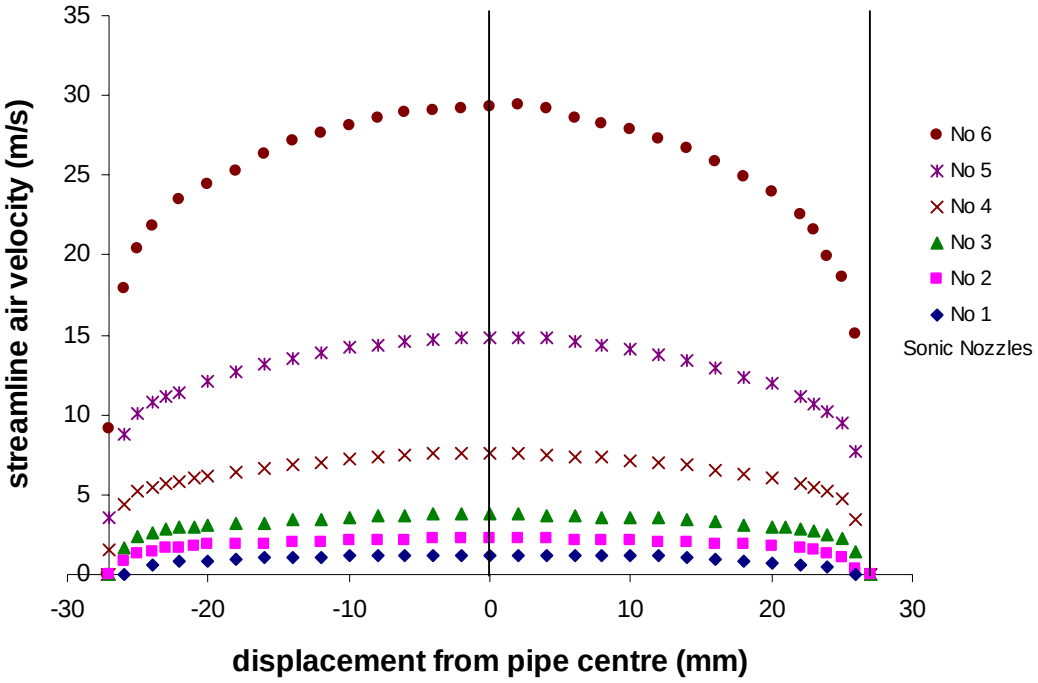


Figure 35, sonic nozzle array 1 velocity profile

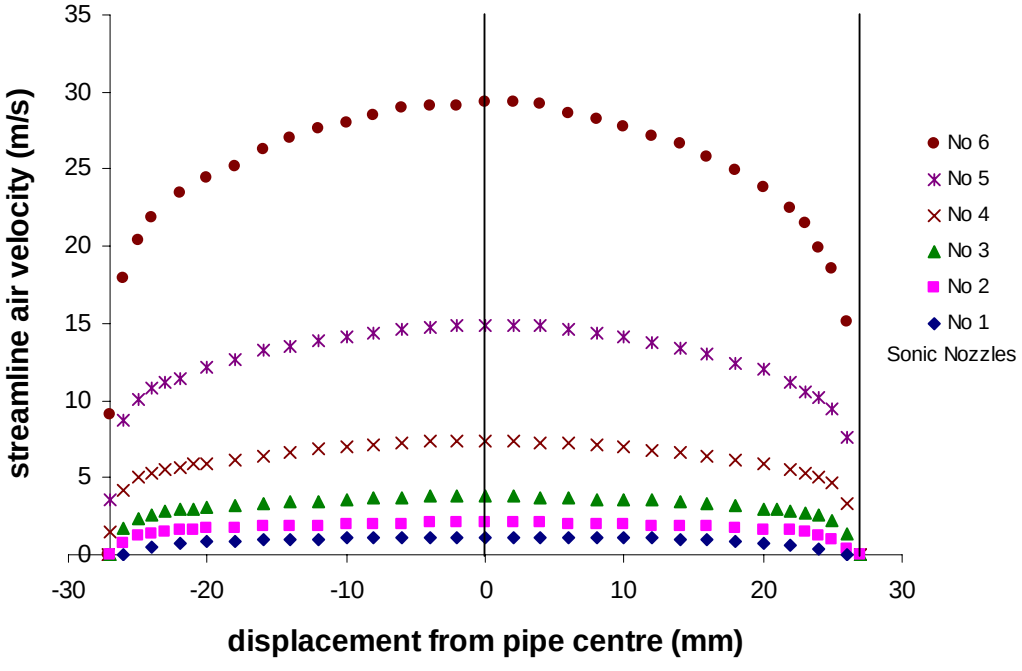


Figure 36, sonic nozzle array 2 velocity profile

The volumetric flow rate ($Q$) (and ultimately the air mass flow rate) was found through the addition of the half annulus area for each average streamline velocity segment. This addition process is basically an application of the Simpson's rule integration technique, i.e:

$$\frac{M_a}{\rho_a} = Q = \sum_{i=-R}^{R} \frac{\pi}{4} ABS\left|r_{i+1}^2 - r_i^2\right| \left[\left(v_{a,s}\right)_i + \left(v_{a,s}\right)_{i+1}\right] \tag{3.4}$$

where $r$ is the displacement from the pipe centre ($r_{i=0}$), $R$ is the pipe radius and subscript $i$ refers to a data point of a particular sonic nozzle, as displayed in either Figure 35 or Figure 36. The sonic nozzle array 1 was used for the primary airflow with sonic nozzle array 2 utilised for the secondary airflow. The results of the air mass flow rate calibration for each sonic nozzle can be seen in Table 10. It is relatively easy to then adjust the flow rate to any of the 63 possible air mass flow settings available in each sonic nozzle array. The settings for each array have the capability to be varied from approximately 0.0020 kg/s to a potential maximum of approximately 0.128 kg/s.

Table 10, air mass flow rates for each sonic nozzle

| **Array 1 (Primary air)** | | **Array 2 (Secondary air)** | |
|---|---|---|---|
| *No.* | *Flow Rate (kg/s)* | *No.* | *Flow Rate (kg/s)* |
| 1 | 0.0021 | 1 | 0.0020 |
| 2 | 0.0046 | 2 | 0.0042 |
| 3 | 0.0079 | 3 | 0.0079 |
| 4 | 0.0162 | 4 | 0.0157 |
| 5 | 0.0324 | 5 | 0.0324 |
| 6 | 0.0648 | 6 | 0.0647 |

### 3.3.4 Conveying pipeline configurations

Three different 53mm (2 inch) bore pipeline configurations were used for the conveying tests which varied from a 130 m short radius bend pipeline (Figure 37), 176 m short radius bend pipeline (Figure 38) and a 173m multi radius bend pipeline (Figure 39). The bend radius and total pipeline length were changed so that the effects of differences in pipeline length and bend geometry could be compared to the pneumatic conveying models presented in Chapters 4 and 5. The major features that are similar in all the

pipeline configurations are that the majority of the pipeline is horizontal with the vertical up segments at the start and at the end of the pipeline.

The 173 m pipeline was the last pipeline configuration used in the conveying trials and extra pressure transducer access plugs were added to correlate pressure readings to newer pressure drop models. Initially 8 pressure transducer access plugs were incorporated into a straight length of pipe (transducer position T8-T15 as shown in Figure 39). Sight glasses (Figure 40) were also situated at each end of the T8-T15 access points. A further 4 transducers access points were added at a likely blockage point (Figure 40) around a bend near the beginning of the pipeline (T1-T4) with 3 more transducers access points placed on a bend near the end of the pipeline (T5-T7). The exact location of each transducer access point is detailed in Table 11. The pressure results from transducers placed in these access points are detailed and discussed in Chapters 4 and 5.

Table 11, transducer access point location

| No. | Distance from start of 130 m pipeline (m) | Distance from start of 173 m pipeline (m) | Distance from bend (m) |
|---|---|---|---|
| T1 | | 37.5 | 0.25 before bend |
| T2 | | 39.2 | 0.25 after bend |
| T3 | | 40.2 | 1.25 after bend |
| T4 | | 41.2 | 2.25 after bend |
| T5 | | 130.3 | 0.25 before bend |
| T6 | | 132.0 | 0.25 after bend |
| T7 | | 135.2 | 3.45 after bend |
| T8 | 81.5 | 141.4 | Straight section |
| T9 | 82.1 | 142.9 | Straight section |
| T10 | 83.1 | 143.9 | Straight section |
| T11 | 84.1 | 144.9 | Straight section |
| T12 | 85.1 | 145.9 | Straight section |
| T13 | 86.1 | 146.9 | Straight section |
| T14 | 87.1 | 147.9 | Straight section |
| T15 | 87.7 | 148.4 | Straight section |

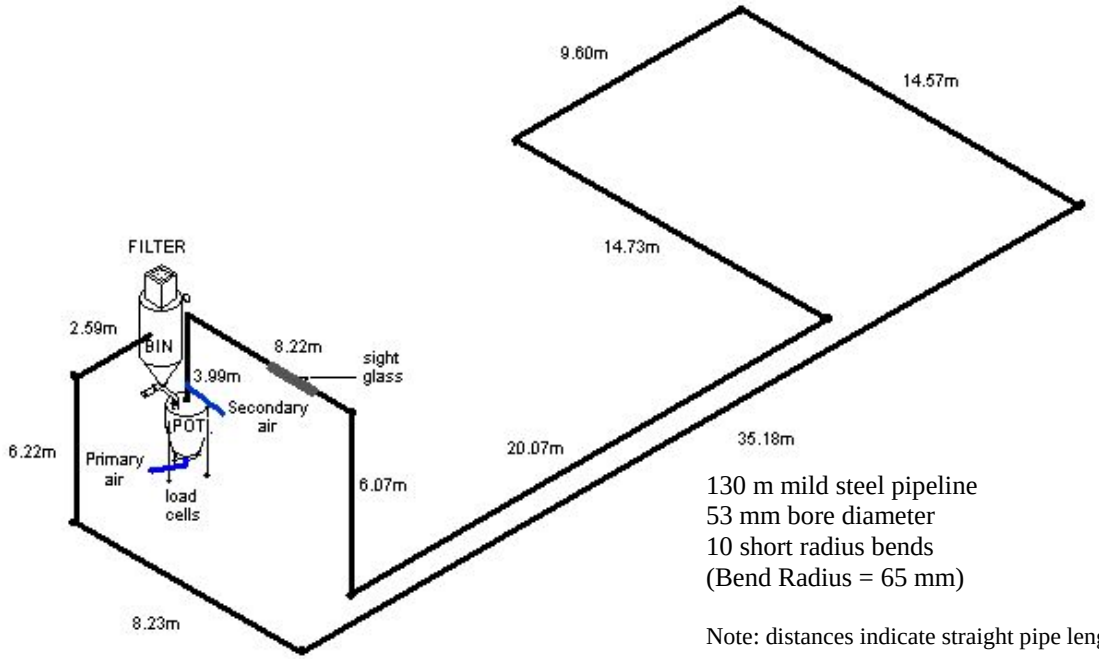


130 m mild steel pipeline
53 mm bore diameter
10 short radius bends
(Bend Radius = 65 mm)

Note: distances indicate straight pipe lengths

Figure 37, diagram of 130 m short radius pipeline

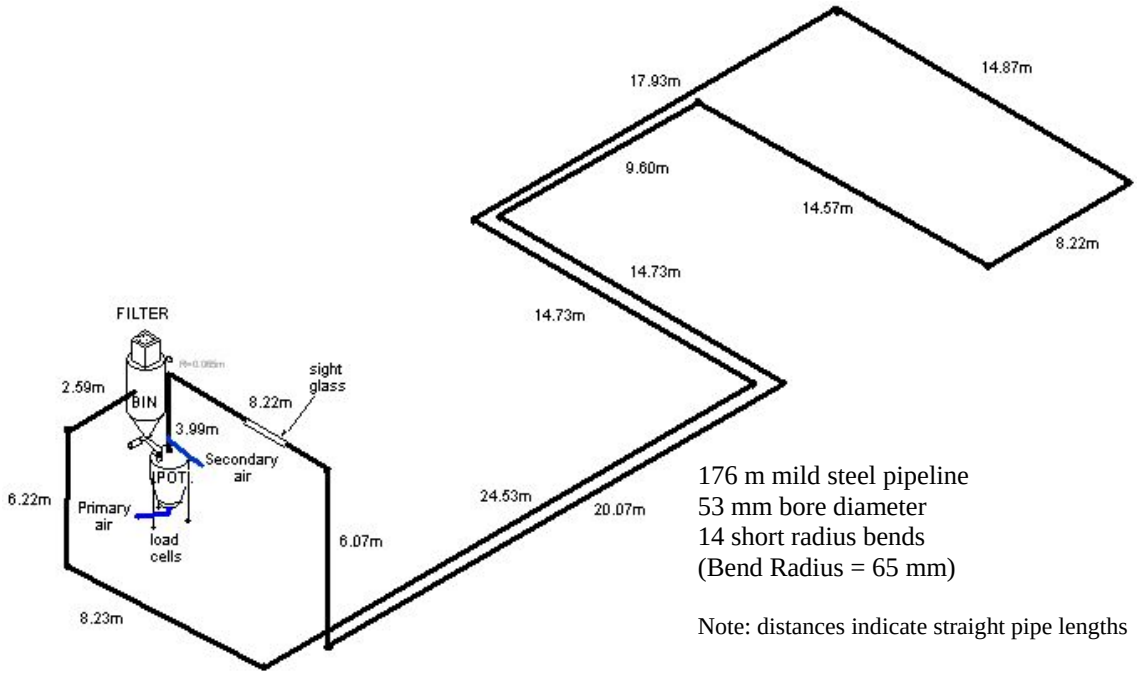


176 m mild steel pipeline
53 mm bore diameter
14 short radius bends
(Bend Radius = 65 mm)

Note: distances indicate straight pipe lengths

Figure 38, diagram of 176 m short radius pipeline

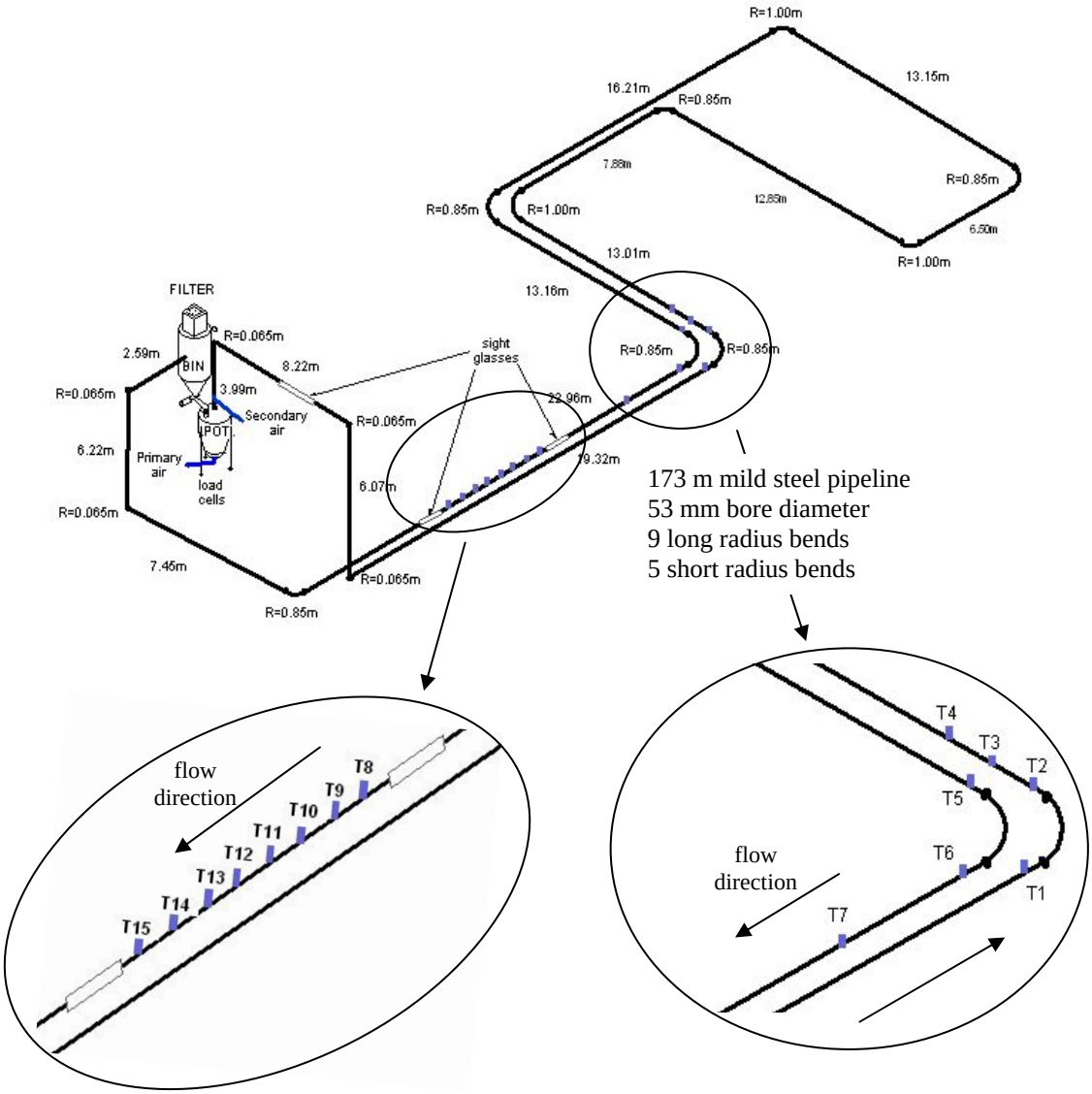


Figure 39, diagram of 173 m variable radius pipeline


Figure 40, pictures of transducer and pipe blockage access points and sight glass

### 3.3.5 test procedure and analysis

As stated earlier, the conveying tests were conducted for Cement Meal, Flyash and Alumina to determine and compare each material's fluidised dense phase conveying parameters and capabilities. Initially the majority of the conveying tests were conducted on Cement Meal in the 130 m pipeline. The pipeline was then increased in length to the 176m configuration with the number of bends increasing from 9 to 14, which basically gave a similar total pipeline length to bend ratio. Finally, the bend radius was changed to long radius bends at the horizontal to horizontal connections to investigate the effect of bend radius on the pressure model. The changes in bend radius also effectively shortened the 176 m configuration to the 173 m total length pipeline. Finally, both the Flyash and Alumina were conveyed in the 173 m pipeline to further investigate the pressure model for different bulk materials.

#### *3.3.5.1 test procedure*

Approximately 0.7 $m^3$ of bulk material was transferred via an eductor vacuum conveyor to the blow tank. After loading, the pinch valve was closed and the material was fluidised with the fluidising air exiting via a vent in the blow tank. After fluidisation, the vent valve was closed, the data acquisition system was activated and the blow tank was pre-pressurised to a value between 10 to 20 kPa above the expected steady state conveying pressure via the primary air. The secondary air was then set and turned on. Once pre-pressurisation was completed, the pinch valve was then opened to start the conveying test. The test was continually monitored and, if successful, was allowed to continue until all the material was emptied from the blow tank. Once the test was completed, the bottom of the receival bin was opened to allow the bulk material to flow back into the blow tank for the next test.

#### *3.3.5.2 test analysis*

For each conveying test, an analysis was conducted to determine if there was an observable steady state period, which is characterised by constant pressure in the blow tank, as shown in Figure 41 and Figure 42. If no steady state period was observed in the test, the results were not used for any subsequent analysis. The usual reason for discarding a conveying test data set was that the pressure in the blow tank continued to

rise above or descend below the pre-pressurisation value. The test was subsequently repeated by pre-pressurising the blow tank to a higher or lower value.

During each successful conveying test, initially there was a surge of material from the blow tank when the pinch valve was opened. Generally, the duration of ‘surging’ was longer at a higher solids flow rate. This surging was associated with the sudden decrease in pressure from the pre-pressurised value in the blow tank which initially increased the air mass flow rate above the steady state setting through the pipeline. After this initial surge, a period of steady state material discharge from the blow tank occurred while the pressure increased until it attained a steady state value. At the end of the conveying cycle, the feeding capabilities of the blow tank reduced due to the lower material level and feeding behaviour of the bulk material in the blow tank. During the slower dense phase pneumatic conveying tests, there was typically an increased rate of bulk material discharged into the receival bin at the end of the conveying cycle, as shown in Figure 42. This higher solids flow rate can be attributed to the pressure decay in the feeding blow tank, which increased the overall air mass flow rate in the pipeline, thus providing more energy to convey the material at a higher flow rate. At the end of each test there was a certain amount of material left in the blow tank which was indicative of its dead capacity. Typically, 80 kg of Cement Meal, 40 kg of Flyash and 20 kg of Alumina remained in the blow tank.

Generally, the analysis of each test consisted of determining the steady state region within each conveying test. The steady state region was then analysed to determine the global conveying parameters of pressure drop and solids mass flow rate. The solids mass flow rate was determined from the average of the slope from the mass loss from the feeder (blow tank) and mass gain to the receival bin, versus time. The steady state air mass flow rate was determined from the pre-set sonic nozzle values. An example of an analysis of two successful tests can be seen in Figure 41 and Figure 42. The steady state global conveying conditions determined for the pneumatic conveying tests in the 130 m, 176 m and 173 m pipeline are shown in Table 12, Table 13 and Table 14 respectively.

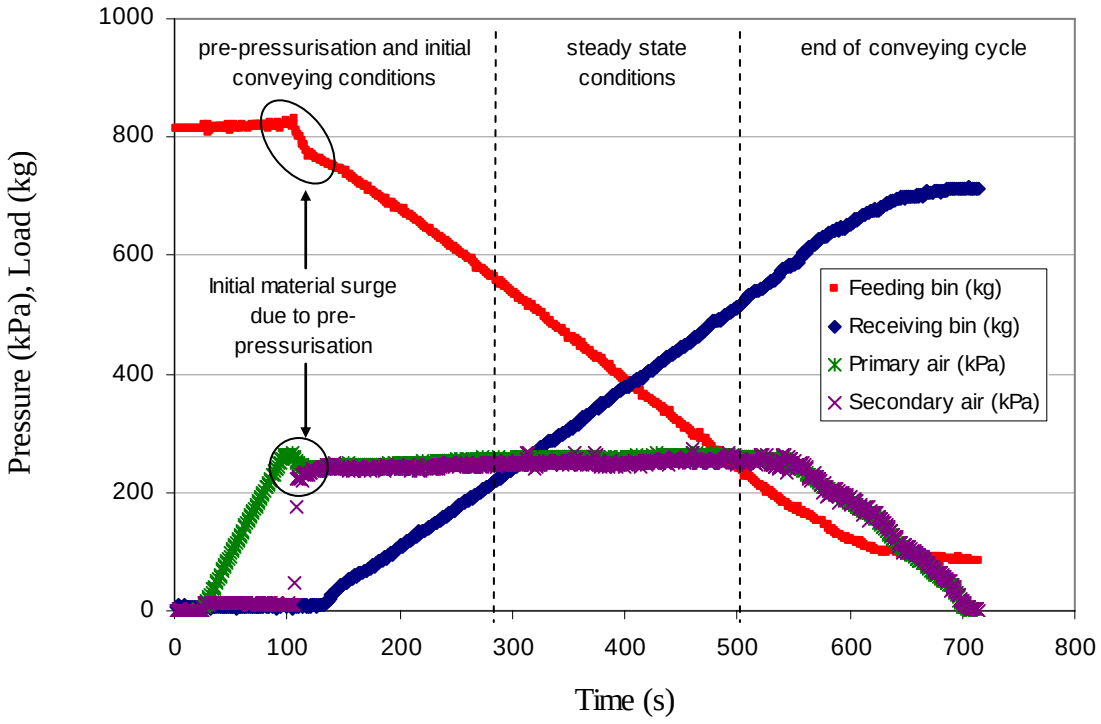


Figure 41, conveying test data for Cement Meal with a primary airflow of 0.0100 kg/s and a secondary airflow of 0.0403 kg/s

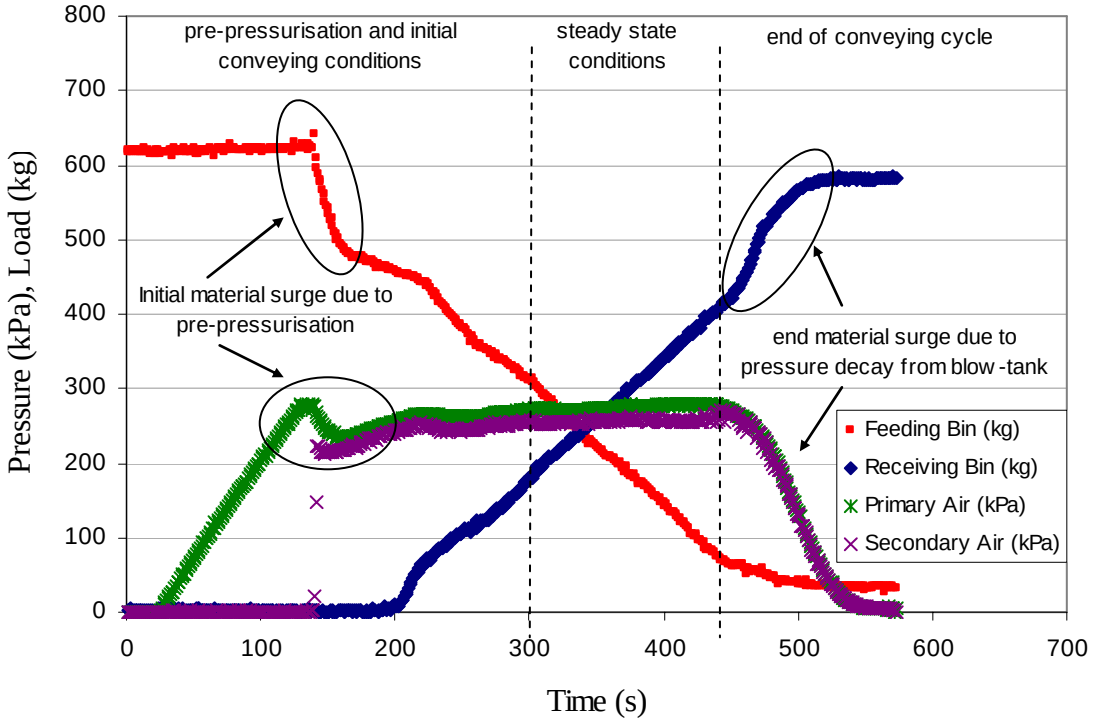


Figure 42, conveying test data for Flyash with a primary airflow of 0.0100 kg/s and a secondary airflow of 0.0121 kg/s

Table 12, 130 m short radius bend pneumatic conveying test data

| Material | Test number | Primary Air Mass Flow rate [kg/s] | Secondary Air Mass Flow rate [kg/s] | Total Air Mass Flow Rate [kg/s] | Solids Mass Flow Rate [kg/s] | m* | Pipeline Pressure Drop [kPa] |
|---|---|---|---|---|---|---|---|
| Cement Meal | CM130-1 | 0.0403 | 0.0403 | 0.0806 | 4.09 | 50.7 | 405 |
| | CM130-2 | 0.0345 | 0.0366 | 0.0711 | 3.99 | 56.1 | 387 |
| | CM130-3 | 0.0345 | 0.0324 | 0.0669 | 4.09 | 61.1 | 380 |
| | CM130-4 | 0.0308 | 0.0403 | 0.0711 | 3.50 | 49.2 | 355 |
| | CM130-5 | 0.0287 | 0.0278 | 0.0565 | 3.46 | 61.2 | 355 |
| | CM130-6 | 0.0287 | 0.0256 | 0.0543 | 3.79 | 69.7 | 358 |
| | CM130-7 | 0.0262 | 0.0366 | 0.0628 | 3.52 | 56.1 | 344 |
| | CM130-8 | 0.0262 | 0.0219 | 0.0481 | 3.68 | 76.5 | 360 |
| | CM130-9 | 0.0241 | 0.0236 | 0.0477 | 3.14 | 65.8 | 338 |
| | CM130-10 | 0.0208 | 0.0403 | 0.0611 | 3.05 | 50.0 | 318 |
| | CM130-11 | 0.0208 | 0.0298 | 0.0506 | 2.90 | 57.4 | 310 |
| | CM130-12 | 0.0208 | 0.0256 | 0.0464 | 3.02 | 65.1 | 314 |
| | CM130-13 | 0.0208 | 0.0199 | 0.0407 | 2.72 | 66.8 | 294 |
| | CM130-14 | 0.0183 | 0.0366 | 0.0549 | 2.82 | 51.4 | 295 |
| | CM130-15 | 0.0183 | 0.0177 | 0.0360 | 2.54 | 70.6 | 308 |
| | CM130-16 | 0.0146 | 0.0157 | 0.0303 | 1.92 | 63.3 | 270 |
| | CM130-17 | 0.0146 | 0.0141 | 0.0287 | 1.90 | 66.2 | 285 |
| | CM130-18 | 0.0100 | 0.0199 | 0.0299 | 1.81 | 60.5 | 227 |
| | CM130-19 | 0.0067 | 0.0141 | 0.0208 | 1.18 | 56.7 | 217 |

Table 13, 176 m short radius bend pneumatic conveying test data

| Material | Test number | Primary Air Mass Flow rate [kg/s] | Secondary Air Mass Flow rate [kg/s] | Total Air Mass Flow Rate [kg/s] | Solids Mass Flow Rate [kg/s] | m* | Pipeline Pressure Drop [kPa] |
|---|---|---|---|---|---|---|---|
| Cement Meal | CM176-1 | 0.0208 | 0.0602 | 0.0810 | 2.12 | 26.2 | 315 |
| | CM176-2 | 0.0208 | 0.0602 | 0.0810 | 2.38 | 29.4 | 348 |
| | CM176-3 | 0.0100 | 0.0403 | 0.0503 | 1.48 | 29.4 | 249 |
| | CM176-4 | 0.0100 | 0.0366 | 0.0466 | 1.56 | 33.5 | 257 |
| | CM176-5 | 0.0100 | 0.0324 | 0.0424 | 1.49 | 35.1 | 247 |
| | CM176-6 | 0.0100 | 0.0278 | 0.0378 | 1.53 | 40.5 | 259 |
| | CM176-7 | 0.0100 | 0.0403 | 0.0503 | 1.55 | 30.8 | 260 |
| | CM176-8 | 0.0100 | 0.0236 | 0.0336 | 1.55 | 46.1 | 273 |
| | CM176-9 | 0.0100 | 0.0199 | 0.0299 | 1.50 | 50.2 | 275 |
| | CM176-10 | 0.0100 | 0.0157 | 0.0257 | 1.30 | 50.6 | 277 |
| | CM176-11 | 0.0100 | 0.0403 | 0.0503 | 1.58 | 31.4 | 267 |
| | CM176-12 | 0.0100 | 0.0121 | 0.0221 | 1.10 | 49.8 | 298 |
| | CM176-13 | 0.0125 | 0.0366 | 0.0491 | 1.86 | 37.9 | 285 |
| | CM176-14 | 0.0125 | 0.0199 | 0.0324 | 1.75 | 54.0 | 297 |
| | CM176-15 | 0.0067 | 0.0121 | 0.0188 | 0.89 | 47.3 | 259 |

Table 14, 173 m variable radius bend pneumatic conveying test data

| Material | Test number | Primary Air Mass Flow rate [kg/s] | Secondary Air Mass Flow rate [kg/s] | Total Air Mass Flow Rate [kg/s] | Solids Mass Flow Rate [kg/s] | m* | Pipeline Pressure Drop [kPa] |
|---|---|---|---|---|---|---|---|
| Cement Meal | CM173-1 | 0.0208 | 0.0602 | 0.0810 | 2.68 | 33.1 | 367 |
| | CM173-2 | 0.0125 | 0.0366 | 0.0491 | 1.94 | 39.6 | 337 |
| | CM173-3 | 0.0125 | 0.0199 | 0.0324 | 1.87 | 57.6 | 345 |
| | CM173-4 | 0.0100 | 0.0403 | 0.0503 | 1.60 | 31.8 | 254 |
| | CM173-5 | 0.0100 | 0.0366 | 0.0466 | 1.65 | 35.3 | 253 |
| | CM173-6 | 0.0100 | 0.0324 | 0.0424 | 1.63 | 38.4 | 262 |
| | CM173-7 | 0.0100 | 0.0278 | 0.0378 | 1.61 | 42.5 | 261 |
| | CM173-8 | 0.0100 | 0.0236 | 0.0336 | 1.58 | 47.1 | 269 |
| | CM173-9 | 0.0100 | 0.0199 | 0.0299 | 1.55 | 51.8 | 280 |
| | CM173-10 | 0.0100 | 0.0157 | 0.0257 | 1.47 | 57.2 | 288 |
| | CM173-11 | 0.0067 | 0.0121 | 0.0188 | 0.99 | 52.5 | 273 |
| Flyash | FA173-1 | 0.0308 | 0.0501 | 0.0809 | 3.60 | 44.4 | 377 |
| | FA173-2 | 0.0241 | 0.0344 | 0.0585 | 3.14 | 53.6 | 343 |
| | FA173-3 | 0.0208 | 0.0602 | 0.0810 | 2.77 | 34.2 | 332 |
| | FA173-4 | 0.0208 | 0.0445 | 0.0653 | 3.02 | 46.2 | 327 |
| | FA173-5 | 0.0183 | 0.0543 | 0.0726 | 2.75 | 37.9 | 314 |
| | FA173-6 | 0.0183 | 0.0278 | 0.0461 | 2.72 | 58.9 | 317 |
| | FA173-7 | 0.0162 | 0.0602 | 0.0764 | 2.51 | 32.9 | 307 |
| | FA173-8 | 0.0162 | 0.0177 | 0.0339 | 2.35 | 69.2 | 308 |
| | FA173-9 | 0.0146 | 0.0366 | 0.0512 | 2.38 | 46.5 | 280 |
| | FA173-10 | 0.0146 | 0.0141 | 0.0287 | 2.13 | 74.4 | 308 |
| | FA173-11 | 0.0125 | 0.0236 | 0.0361 | 2.08 | 57.7 | 270 |
| | FA173-12 | 0.0100 | 0.0501 | 0.0601 | 1.79 | 29.7 | 232 |
| | FA173-13 | 0.0100 | 0.0403 | 0.0503 | 2.02 | 40.1 | 253 |
| | FA173-14 | 0.0100 | 0.0298 | 0.0398 | 1.93 | 48.4 | 251 |
| | FA173-15 | 0.0100 | 0.0199 | 0.0299 | 1.79 | 59.8 | 251 |
| | FA173-16 | 0.0100 | 0.0157 | 0.0257 | 1.67 | 64.9 | 260 |
| | FA173-17 | 0.0100 | 0.0121 | 0.0221 | 1.63 | 73.9 | 278 |
| | FA173-18 | 0.0100 | 0.0099 | 0.0199 | 1.49 | 75.1 | 294 |
| | FA173-19 | 0.0100 | 0.0079 | 0.0179 | 1.52 | 85.1 | 317 |
| | FA173-20 | 0.0067 | 0.0501 | 0.0568 | 1.37 | 24.2 | 197 |
| | FA173-21 | 0.0067 | 0.0121 | 0.0188 | 1.37 | 72.9 | 248 |
| | FA173-22 | 0.0046 | 0.0177 | 0.0223 | 1.18 | 53.0 | 186 |
| Alumina | AL173-1 | 0.0183 | 0.0602 | 0.0785 | 2.53 | 32.2 | 349 |
| | AL173-2 | 0.0146 | 0.0501 | 0.0647 | 2.23 | 34.4 | 316 |
| | AL173-3 | 0.0100 | 0.0602 | 0.0702 | 1.74 | 24.8 | 257 |
| | AL173-4 | 0.0100 | 0.0501 | 0.0601 | 1.37 | 22.7 | 235 |
| | AL173-5 | 0.0100 | 0.0501 | 0.0601 | 1.73 | 28.8 | 266 |
| | AL173-6 | 0.0100 | 0.0445 | 0.0545 | 3.26 | 59.8 | 432 |
| | AL173-7 | 0.0100 | 0.0403 | 0.0503 | 2.97 | 59.0 | 431 |
| | AL173-8 | 0.0067 | 0.0403 | 0.0470 | 3.00 | 63.7 | 408 |
| | AL173-9 | 0.0067 | 0.0403 | 0.0470 | 1.37 | 29.2 | 237 |
| | AL173-10 | 0.0046 | 0.0366 | 0.0412 | 2.91 | 70.7 | 404 |
| | AL173-11 | 0.0046 | 0.0366 | 0.0412 | 1.34 | 32.5 | 238 |

## *3.4 Jones Pneumatic Conveying Test Data [18]*

Many thanks must go to my supervisor, Professor M.G. Jones for data supplied on three more products which exhibited fluidised dense phase capabilities which were ‘Pulverised Fuel Ash’, ‘Democrat Flour’ and ‘Iron Powder’. The three bulk materials were conveyed in a 165 ft (approx 50 m) long pipeline with a 2 inch (approx 53mm) nominal bore. The pipeline also consisted of 9 long radius bends, a blow tank feeder and a receival bin, as shown in Figure 43. This conveying system is similar to the previous pipeline configurations described in Chapter 3.3.4 as the majority of the pipeline is horizontal and the bulk material is fed into the pipeline via a top discharge blow tank. The bulk material parameters and steady state global pneumatic conveying data are detailed for the three bulk materials in the following sub-chapters. These three materials were also part of the material data set used by Jones in his PhD dissertation [18].

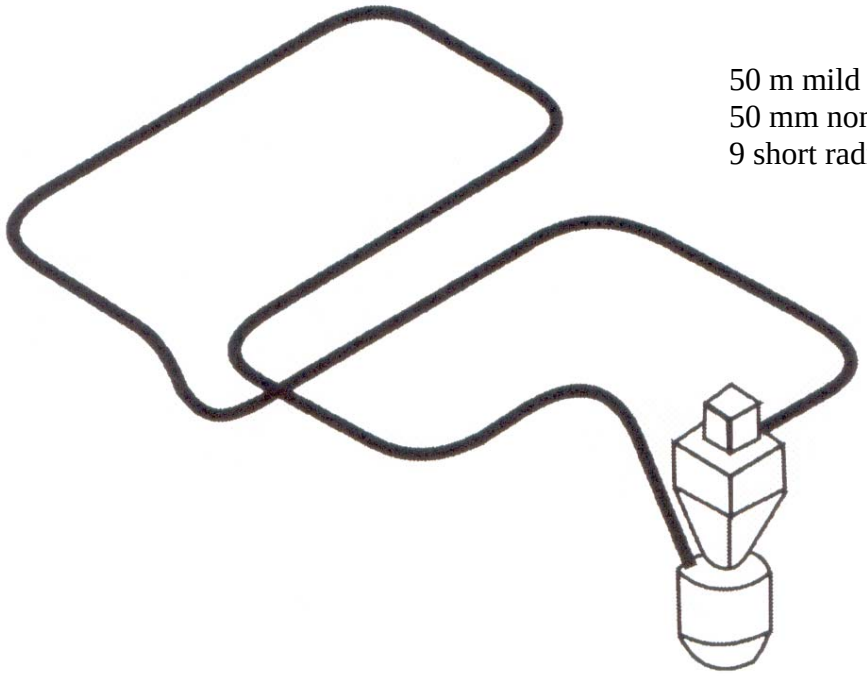


Figure 43, schematic of pneumatic conveying pipeline utilised by Jones

### 3.4.1 Pulverised Fuel Ash data sheet

| | | | | |
|---|---|---|---|---|
| *Average particle diameter* | $d_p$ | = | $25 \times 10^{-6}$ | *m* |
| *Particle Density* | $\rho_s$ | = | *2446* | $kg/m^3$ |
| *'Tapped' Bulk Density* | $\rho_{bt}$ | = | *1456* | $kg/m^3$ |
| *'Loose Poured' Bulk Density* | $\rho_{bl}$ | = | *979* | $kg/m^3$ |
| *Hausner Ratio* | *HR* | = | *0.328* | - |
| *'Loose Poured' Voidage* | $\varepsilon_{bl}$ | = | *0.600* | - |
| *Permeability* | $\Psi$ | = | $0.60 \times 10^{-6}$ | $m^3\ s/kg$ |

Table 15, fluidised dense phase global conveying data for Pulverised Fuel Ash

| Material | Test number | Total Air Mass Flow Rate [kg/s] | Solids Mass Flow Rate [kg/s] | m* | Pipeline Pressure Drop [kPa] | Test number | Total Air Mass Flow Rate [kg/s] | Solids Mass Flow Rate [kg/s] | m* | Pipeline Pressure Drop [kPa] |
|---|---|---|---|---|---|---|---|---|---|---|
| Pulverised Fuel Ash | PA50-1 | 0.028 | 3.68 | 130 | 150 | PA50-14 | 0.048 | 1.94 | 40.5 | 100 |
| | PA50-2 | 0.022 | 0.764 | 34.3 | 40 | PA50-15 | 0.051 | 1.79 | 35.1 | 115 |
| | PA50-3 | 0.028 | 1.39 | 48.9 | 70 | PA50-16 | 0.051 | 1.82 | 35.5 | 100 |
| | PA50-4 | 0.03 | 1.53 | 51.7 | 80 | PA50-17 | 0.051 | 1.67 | 32.5 | 100 |
| | PA50-5 | 0.03 | 1.00 | 33.4 | 55 | PA50-18 | 0.051 | 1.54 | 30.3 | 90 |
| | PA50-6 | 0.035 | 1.78 | 50.4 | 85 | PA50-19 | 0.060 | 3.44 | 57.0 | 140 |
| | PA50-7 | 0.037 | 1.74 | 47.0 | 90 | PA50-20 | 0.073 | 3.52 | 48.4 | 190 |
| | PA50-8 | 0.036 | 1.43 | 39.8 | 75 | PA50-21 | 0.056 | 1.67 | 29.6 | 100 |
| | PA50-9 | 0.038 | 1.76 | 46.2 | 90 | PA50-22 | 0.068 | 2.85 | 41.9 | 160 |
| | PA50-10 | 0.037 | 1.11 | 29.8 | 60 | PA50-23 | 0.05 | 0.78 | 15.7 | 60 |
| | PA50-11 | 0.037 | 0.868 | 23.2 | 60 | PA50-24 | 0.06 | 1.94 | 32.2 | 110 |
| | PA50-12 | 0.042 | 1.53 | 36.3 | 80 | PA50-25 | 0.06 | 2.13 | 35.3 | 105 |
| | PA50-13 | 0.048 | 1.94 | 40.6 | 100 | | | | | |

### 3.4.2 Democrat Flour

| | | | | |
|---|---|---|---|---|
| *Average particle diameter* | $d_p$ | = | $90 \times 10^{-6}$ | *m* |
| *Particle Density* | $\rho_s$ | = | *1470* | $kg/m^3$ |
| *'Tapped' Bulk Density* | $\rho_{bt}$ | = | *700* | $kg/m^3$ |
| *'Loose Poured' Bulk Density* | $\rho_{bl}$ | = | *510* | $kg/m^3$ |
| *Hausner Ratio* | *HR* | = | *0.271* | - |
| *'Loose Poured' Voidage* | $\varepsilon_{bl}$ | = | *0.653* | - |
| *Permeability* | $\Psi$ | = | $0.23 \times 10^{-6}$ | $m^3$ *s/kg* |

Table 16, fluidised dense phase global conveying data for Democrat Flour

| Material | Test number | Total Air Mass Flow Rate [kg/s] | Solids Mass Flow Rate [kg/s] | m* | Pipeline Pressure Drop [kPa] | Test number | Total Air Mass Flow Rate [kg/s] | Solids Mass Flow Rate [kg/s] | m* | Pipeline Pressure Drop [kPa] |
|---|---|---|---|---|---|---|---|---|---|---|
| Democrat Flour | DF50-1 | 0.013 | 0.640 | 51.2 | 70 | DF50-18 | 0.050 | 2.62 | 52.9 | 170 |
| | DF50-2 | 0.012 | 1.32 | 107 | 60 | DF50-19 | 0.046 | 2.05 | 44.2 | 140 |
| | DF50-3 | 0.018 | 1.28 | 71.1 | 100 | DF50-20 | 0.066 | 3.59 | 54.2 | 240 |
| | DF50-4 | 0.021 | 1.88 | 89.0 | 120 | DF50-21 | 0.065 | 3.07 | 47.5 | 220 |
| | DF50-5 | 0.020 | 1.22 | 62.0 | 90 | DF50-22 | 0.050 | 1.59 | 31.8 | 120 |
| | DF50-6 | 0.022 | 0.969 | 44.0 | 70 | DF50-23 | 0.058 | 2.39 | 41.1 | 170 |
| | DF50-7 | 0.029 | 1.99 | 68.7 | 125 | DF50-24 | 0.056 | 1.95 | 34.8 | 150 |
| | DF50-8 | 0.029 | 1.62 | 56.9 | 110 | DF50-25 | 0.083 | 4.61 | 55.6 | 300 |
| | DF50-9 | 0.037 | 2.73 | 73.6 | 160 | DF50-26 | 0.083 | 3.84 | 46.5 | 290 |
| | DF50-10 | 0.036 | 2.43 | 67.1 | 150 | DF50-27 | 0.077 | 3.07 | 40.0 | 230 |
| | DF50-11 | 0.029 | 0.969 | 33.8 | 70 | DF50-28 | 0.082 | 3.07 | 37.4 | 260 |
| | DF50-12 | 0.035 | 1.59 | 45.4 | 110 | DF50-29 | 0.050 | 0.933 | 18.7 | 70 |
| | DF50-13 | 0.038 | 2.18 | 57.0 | 135 | DF50-30 | 0.066 | 1.89 | 28.7 | 155 |
| | DF50-14 | 0.036 | 1.49 | 41.0 | 100 | DF50-31 | 0.086 | 3.33 | 38.8 | 260 |
| | DF50-15 | 0.047 | 3.28 | 70.5 | 185 | DF50-32 | 0.074 | 2.43 | 32.7 | 190 |
| | DF50-16 | 0.061 | 4.35 | 71.5 | 260 | DF50-33 | 0.060 | 1.42 | 23.6 | 110 |
| | DF50-17 | 0.048 | 2.39 | 50.0 | 160 | | | | | |

### 3.4.3 Iron Powder data sheet

| | | | | |
|---|---|---|---|---|
| *Average particle diameter* | $d_p$ | = | $64 \times 10^{-6}$ | *m* |
| *Particle Density* | $\rho_s$ | = | *5710* | $kg/m^3$ |
| *'Tapped' Bulk Density* | $\rho_{bt}$ | = | *3190* | $kg/m^3$ |
| *'Loose Poured' Bulk Density* | $\rho_{bl}$ | = | *2380* | $kg/m^3$ |
| *Hausner Ratio* | *HR* | = | *0.254* | - |
| *'Loose Poured' Voidage* | $\varepsilon_{bl}$ | = | *0.583* | - |
| *Permeability* | $\Psi$ | = | $0.34 \times 10^{-6}$ | $m^3\ s/kg$ |

Table 17, fluidised dense phase global conveying data for Iron Powder

| Material | Test number | Total Air Mass Flow Rate [kg/s] | Solids Mass Flow Rate [kg/s] | m* | Pipeline Pressure Drop [kPa] |
|---|---|---|---|---|---|
| Iron Powder | IP50-1 | 0.030 | 2.98 | 101 | 170 |
| | IP50-2 | 0.038 | 5.47 | 143 | 220 |
| | IP50-3 | 0.037 | 3.73 | 101 | 200 |
| | IP50-4 | 0.040 | 3.15 | 79.5 | 180 |
| | IP50-5 | 0.048 | 5.64 | 118 | 240 |
| | IP50-6 | 0.037 | 2.49 | 66.7 | 140 |
| | IP50-7 | 0.049 | 3.36 | 68.2 | 175 |
| | IP50-8 | 0.048 | 2.88 | 60.1 | 160 |
| | IP50-9 | 0.068 | 5.97 | 87.6 | 245 |
| | IP50-10 | 0.068 | 5.47 | 80.2 | 245 |
| | IP50-11 | 0.060 | 3.48 | 58.4 | 180 |
| | IP50-12 | 0.068 | 5.17 | 76.3 | 210 |
| | IP50-13 | 0.085 | 5.60 | 65.9 | 290 |
| | IP50-14 | 0.085 | 6.47 | 75.8 | 285 |
| | IP50-15 | 0.085 | 4.85 | 57.2 | 260 |
| | IP50-16 | 0.077 | 3.36 | 43.7 | 210 |
| | IP50-17 | 0.068 | 2.16 | 31.5 | 160 |
| | IP50-18 | 0.079 | 3.68 | 46.5 | 215 |

# CHAPTER 4: SOLIDS FRICTION CORRELATIONS – REVIEW AND ANALYSIS

When designing pneumatic conveying systems, the two primary aims are, firstly, to ensure the system operates reliably and secondly, to ensure the system is as efficient as possible (i.e. optimised). Certainly the ultimate aim of the user of the pneumatic conveying system is that they desire both reliability and performance while the designer is limited by the available knowledge on pneumatic conveying behaviour to ensure optimum efficiency. Also, the optimisation parameters may vary, and are dependant on the user specifications which can limit available pipeline geometry options like pipeline routing and/or bend configuration. Further design constraints for the solids mass flow rate (or tonnage) requirements may also be imposed of the user or the airflow rate and pressure capability may be restricted due to the available equipment.

However, once the geometric limits and tonnage requirements are known, determining the optimal pressure drop and air flow settings are the final challenge for the designer to determine the most economic air mover systems. For instance, if the combination of air mass flow rate and pressure drop is too low, then the solids may block in the pipeline. Excessively high airflow rates and pressure drop will use excessive power for the flow required, increase particle degradation and/or pipeline wear or convey a dense phase capable material in a dilute phase mode.

For determining the most accurate or optimal combination of pressure drop and air and solids (or particle) mass flow rate, typically the approach has been to use either scale-up techniques utilising experimental test rig data or to use empirical based equations to predict the operating parameters. Generally, pressure prediction models use a superposition technique where the individual pressure losses are calculated separately and are then subsequently added together. The most common individual pressure losses relate to the initial acceleration of the solids into the pipe, the frictional forces of the air and solids, the resistance due to the pipe bends and finally the gravitational effect due to vertical upward flow geometries. Also, although the flow is compressible along the pipeline, these techniques generally employ average or global conveying parameters. This average parameter approach includes singular air density and velocity values

which essentially means that the flow is treated as incompressible, which greatly simplifies the pressure drop calculation.

In fluidised dense phase conveying, the most dominant pressure drop component is due to the solids friction losses. Typically, an empirically based friction factor has been used to determine the associated frictional pressure losses in the fluidised dense phase pneumatic conveying. These friction factors are dominated by a power law relationship and it is the values of the exponents associated with the power law, and the resultant pressure drop that are the focus of this chapter.

## *4.1 Current Pressure Models*

This sub-chapter describes the two common pressure drop prediction techniques previously mentioned; the scale-up method and empirically based models. Generally, a scale-up technique utilises the results of pneumatic conveying tests through a test (or pilot size) pipeline. The results from the test pipeline are then utilised to predict the operating parameters for the actual or plant pipeline and are based on geometric changes and/or frictional parameters. Another significant aspect in the scale–up technique is that the same (or nearly similar) material is used in both the test and actual pipeline. Empirically based methods typically use equations which describe the frictional parameters for the air and solids flow commonly termed as friction factors. While these parameters are based on experimental results, they differ from the scale-up technique as they aim to be generic rather than specific to one material.

### 4.1.1 Scale-up methods

One of the early forms of scale-up techniques was developed by Mason *et al* [26] and Mills *et al* [27] who assumed that the ratio of the solids flow rate from test to plant pipeline was inversely proportional to the pipeline lengths and proportional to the cross-sectional area. This assumption was based on the criteria that the air mass flow rate per cross sectional area and the pressure drop remained constant (i.e. constant $m_f D^{-2}$ and $\Delta P_s$) which gives the following solids mass flow relationship to the two pipeline geometries:

$$\frac{m_{s2}}{m_{s1}} = \frac{L_1}{L_2}\left(\frac{D_2}{D_1}\right)^2 \tag{4.1}$$

Further investigation by Wypych and Arnold [55] found that Equation 4.1 significantly underestimated the scale-up of the solids mass flow rate ($m_{s2}$) when conveying in large bore pipelines and developed a modified scale-up technique from which the diameter ratio exponent (or power index) increases from 2 to 2.8. It is important to note that this increase in diameter ratio exponent suggest that the frictional resistance of the solids per unit area decreases as diameter increases.

Scale up techniques moved towards determining a specific solids friction values with Pan and Wypych [32] in 1992. Pan's technique determined the pressure drop by experimentally calculating the friction parameters of the air and solids in straight pipes and bends separately. Most recently in 2003, Datta and Ratnayaka [7] developed a pressure drop technique which suggested a simplified scale up approach as it combined the resistive forces due to air and solids in the pipeline into a single factor and utilised a similar technique to Bradley's [4] bend technique to compute the bend losses.

### 4.1.2 Empirical methods

Weber [51] in 1981 developed a pneumatic conveying pressure drop technique which calculated the pressure drop due to frictional losses of the fluid ($\lambda_f$) and the solid particles ($\lambda_s$), and the associated increase in pressure requirements due to gravitational effect in vertical upward conveying. Chambers and Marcus [5] in 1986 further developed Webers technique to include the pressure drop due to bends and the initial acceleration of the particles at the feed point. Unfortunately, as Chambers states, the pressure drop prediction can differ by up to a factor of 2 using this technique. Bradley [4] in 1990 further developed a bend pressure model which defined the bend pressure drop for each individual bend within the pipeline using a 'piece-wise' method which sequentially calculated the pressure drop for each individual section of the pipeline (i.e. straight sections and bends). To achieve the 'piece-wise' approach, Bradley commenced the pressure calculations at the pipe exit and started the move away from the averaging techniques.

## *4.2 Solids Friction and Two Phase Fluid Pressure Model*

Generally, the approach used for determining the pressure drop due to frictional resistance utilises a two-phase fluid model. One phase relates the losses due to air alone, while the second phase accounts for the resistance and collisions of solids (or particles) in the pipeline. The two-phase fluid model most commonly used to model pneumatic conveying was first proposed by Weber [51] (from the theories developed from Muschelknautz [30]), which applies a global approach in calculating the pressure drop components. Generally, Weber's model has been used with success for predicting the total frictional pressure drop in dilute phase systems. Equation 4.2 for the air and Equation 4.3 for the solids details the basic form of this model.

$$\Delta P_{fa} = \lambda_a \frac{\rho_a v_a^2}{2} \frac{L}{D} \tag{4.2}$$

$$\Delta P_{fs} = m^* \lambda_s \frac{\rho_a v_a^2}{2} \frac{L}{D} \tag{4.3}$$

where $\Delta P_{fa}$ is the frictional pipeline pressure drop due to air, $\Delta P_{fs}$ is the frictional pipeline pressure drop due to the solids, $L$ is the length of the pipe, $D$ is the pipe diameter and $\rho_a$ and $v_a$ are the average conveying air density and velocity respectively. The solids loading ratio, $m^*$, represents the non-dimensional relationship between the mass flow of the particles ($M_s$) and the mass flow of the air ($M_a$) and is defined by Equation 4.4.

$$m^* = \frac{M_s}{M_a} \tag{4.4}$$

### 4.2.1 Air friction factors

In Equation 4.1, $\lambda_a$ defines the air friction factor which assumed to be a function of Reynolds Number. In pneumatic conveying, $\lambda_a$ can be determined by the Blasius Equation for smooth turbulent flow:

$$\lambda_a = \frac{0.316}{\mathrm{Re}_a^{0.25}} \text{ and } \mathrm{Re}_a = \frac{\rho_a v_a D}{\mu} \tag{4.5}$$

where $\mathrm{Re}_a$ is the average superficial air Reynolds number and $\mu$ is the air viscosity. Alternatively, the equation developed by Streeter and Wylie has been used (and is used in this thesis) which is defined as:

$$\lambda_a = \frac{1.325}{\ln\left(\frac{5.74}{\mathrm{Re}_a^{0.9}}\right)^2} \tag{4.6}$$

It is significant to note that the air only pressure drop for the fluidised dense phase experiments detailed in Chapter 3 make up less than 10% of the total pressure drop of the pipeline and, as such, is not the focus of this thesis. However, the reader is directed to the work of Wypych and Pan [57] who have investigated the air only pressure drop in pneumatic conveying systems.

### 4.2.2 Solids friction factors

In Equation 4.2, $\lambda_s$ defines the solids friction factor and represents the most important pressure component in fluidised dense phase conveying. Correlations for $\lambda_s$ have been developed in the literature for dilute phase flow with the resistive mechanism generally well defined. The dominating components of dilute phase resistance are due to particle-particle and particle-wall collisions and the associated drag forces of the gas flow around the particle. Molerus [29] critically reviewed the physical meaning of the basic form of dilute flow friction correlations for horizontal straight pipes. Rautiainen and Sarkomaa [37] also compared previous correlations and presented a correlation for solids friction factor in vertical (upward) dilute-phase flows.

In fluidised dense phase flow, there is generally a layer of dense material moving along the lower part of the pipeline with dilute-phase flow occurring in the upper layer. This two layer flow is assumed to exhibit a shear like separation between the two flows, but a

homogenous transient full bore pulse of material flow has also been observed. As a result of this complex flow behaviour, the resistive mechanisms of fluidised dense phase flow are not fully understood and are still being investigated, and as such empirically based parameters have dominated the solids pressure drop models.

For dense-phase conveying, success in calculating solids friction factors have been achieved through scale-up procedures (as discussed in Chapter 4.1.1) with Pan and Chambers [34] specifically describing two scale-up techniques. The scale-up friction calculation method involves conveying the material in a test rig and subsequently calculating the solids friction factor specific to the material to estimate the total pipeline pressure drop for the full installation pipeline.

Empirically based correlations have been developed with Weber [51][52] detailing the work on fine powders of Stegmaier [47] which had the form:

$$\lambda_s = \frac{2.1 Fr_s^{0.5}}{m^{*0.3}\, Fr^2}\left(\frac{D}{d_p}\right)^{0.1} \tag{4.7}$$

Wypych [56] also compared the work of Stegmaier with experimental data for a variety of fine powders (7 different types of Flyash, a Cement/Flyash mix and Pulverised Coal). Wypych added the gas density and pipeline length to Stegmaier's correlation and found an improvement in accuracy of the solids friction correlation. Unfortunately, as stated by Wypych, it was found during his research that there was poor convergence of the correlation in predicting the pressure drop. As a result, Wypych's 'best fit' correlation will not be analysed. Further work by Weber [53] compared and modified the work of Seigel [46] and Szksay [49] for coarse materials. Weber developed a mathematical technique to reduce the subsequent variation (errors) between the actual pressure drop to the predicted pressure drop when determining the solids friction correlation. Using this technique, Weber randomly generated simulated pneumatic conveying data to further develop generic solids friction factors, with the correlation found defined as:

$$\lambda_s = \frac{2.98}{m^{*0.69}\, Fr^{1.6}} \tag{4.8}$$

This researcher in conjunction with Jones [20] investigated the use of a pipe inlet velocity Froude number ($Fr_i$) for solids friction correlations specifically for fluidised dense phase conveying which was of the form:

$$\lambda_s = \frac{83}{m^{*0.9}\, Fr_i^{\,2}} \tag{4.9}$$

But subsequent pipe scale up analysis found that the pressure solution did not converge to a solution, so further investigation was conducted on the behaviour of this non-convergence associated with the correlation technique (and is detailed later in this chapter and in Chapter 5).

These reviews and research indicate that the solids friction factor correlations are a function of some or all of the non-dimensional parameters detailed in Equation 4.10, with the superficial gas velocity based Froude number ($Fr$) and $m^*$ the most dominant parameters for horizontal conveying:

$$\lambda_s = f\left( m^*, Fr, Fr_s, \frac{d_s}{D} \right) \tag{4.10}$$

$$Fr = \frac{v_f}{(gD)^{0.5}} \text{ and } Fr_s = \frac{v_t}{(gd_s)^{0.5}} \tag{4.11}$$

where $Fr_s$ is the solids Froude number based on particle settling velocity ($v_t$), $d_s$ is the mean particle diameter, and $\rho_s$ and $\rho_f$ are the solids and fluid densities, respectively. Inspection of these non-dimensional parameters shows that there is certainly justification in using some of these parameters in estimating the resistance of fluidised dense phase conveying, namely:

1. The Solids Loading Ratio ($m^*$) gives proportionality to the mass coupling between the mass of material moved with the air mass input to the system. For fluidised dense phase conveying, this ratio is significantly higher than for dilute phase systems.

2. The Froude Number (*Fr*) is a representation of the kinetic forces of the conveying gas through the superficial gas velocity with respect to the gravitational forces and pipe diameter. For a constant pipe diameter, the Froude number is lower for fluidised dense phase flows when compared to the dilute phase flows.

3. The solids Froude number ($Fr_s$) is a parameter which represents the kinetic forces of a particle compared to the gravitational force. The significance of the solids Froude number is that it is representative of single particle behaviour rather than a bulk effect and therefore there is limited difference in this parameter between dense and dilute flows.

4. The particle diameter to pipe diameter ratio ($d_p$ / $D$) gives proportionality of the solids to the pipeline. This parameter may be more applicable to dilute phase flows where the particles are generally more dispersed and the resistance behaviour is dominated by discrete particle events.

Obviously, there is a large variation in the constants and exponents of the solids friction correlation defined in Equations 4.7, 4.8 and 4.9 as they are strongly based on the range of material and pipe conditions used by the researcher. The technique used to determine the value of these exponents and coefficients also contribute to their respective values. As will be discussed later in this chapter, although there may be slight differences in values between coefficients and exponents, these variations can cause significant differences in the resulting pressure drop prediction or no prediction capability at all occurs.

### 4.2.3 Effect on pressure drop

For further illustration of the effect of the solids friction correlations on pressure drop prediction, Equations 4.7, 4.8 and 4.9 were incorporated into the solids pressure formula detailed by Equation 4.3. The resulting pressure drop equations (Equations 4.12, 4.13, 4.14) were presented as functions of pipeline diameter ($D$), pipeline length ($L$), air mass flow rate ($m_a$) and solids mass flow rate ($m_s$). Therefore, for a specific bulk material, a straight pipe length and neglecting air pressure losses (i.e. $\Delta P_{fs}=\Delta P$), the pressure equations were expressed as:

$$\Delta P_{fs} = \frac{A_1\left(\Delta P_{fs} + 2P_0\right)m_s^{\,0.7} D^{0.1} L}{m_a^{0.7}} \qquad \text{(from Eq. 4.7)} \qquad (4.12)$$

$$\Delta P_{fs} = \frac{B_1\left(\Delta P_{fs} + 2P_0\right)^{0.6} m_s^{0.31} m_a^{0.09} L}{D} \qquad \text{(from Eq. 4.8)} \qquad (4.13)$$

$$\Delta P_{fs} = \frac{C_1\left(\Delta P_{fs} + P_0\right)^2 m_s^{0.1} L}{\left(\Delta P_{fs} + 2P_0\right)m_a^{0.1}} \qquad \text{(from Eq. 4.9)} \qquad (4.14)$$

where $A_1$, $B_1$ and $C_1$ are constants which represent a bulk materials particle settling velocity, gravitational component and pipe exit air conditions ($P_0$ is the absolute exit pressure) with the average pipe air density ($\rho_a$), average superficial air velocity ($v_a$), inlet air density ($\rho_{ai}$) and inlet air superficial velocity ($v_{ai}$) defined as:

$$v_a = \frac{4m_a}{\rho_a \pi D^2} \;,\; \rho_a = \frac{\rho_0}{2P_0}\left(\Delta P + 2P_0\right), \qquad (4.15)$$

$$v_{ai} = \frac{4m_a}{\rho_{ai} \pi D^2} \;,\; \rho_{ai} = \frac{\rho_0}{P_0}\left(\Delta P + P_0\right), \qquad (4.16)$$

where $\rho_0$ is the pipe exit air density.

As expected, the structure of the pressure drop in Equations 4.12 to 4.14 are polynomic, (Equation 4.14 showing a binomial form) which generally requires an iterative process to solve. However, the resulting solutions to the iterative process will be affected by the constants and exponents, which in turn, will affect the rate of change of the pressure component when scaled-up for pipeline diameter and/or length.

Further analysis of the polynomial equations were conducted via program *Maple 9.5* from which the intrinsic function *solve* (which utilises a recursive algorithm) was used to determine the solids pressure drop solutions for Equations 4.12 to 4.14 with the results as follows:

$$\Delta P_{fs} = \frac{A_2 D^{0.1} L}{A_3 - A_4 D^{0.1} L} \qquad \text{(from Eq. 4.12)} \qquad (4.17)$$

$$\Delta P_{fs} = \frac{B_2 L}{D^{2.5}\left(B_3 L^3 + B_4\right)} \qquad \text{(from Eq. 4.13)} \qquad (4.18)$$

$$\Delta P_{fs} = \frac{-P_0\sqrt{C_2 - C_3 L} - C_2^{0.5}}{\sqrt{C_2 - C_3 L}} \qquad \text{(from Eq. 4.14)} \qquad (4.19)$$

where $A_i$, $B_i$ and $C_i$ ($i$ = 2, 3 or 4) are constants which again are representative of a particular bulk material's particle settling velocity, gravitational component and pipe exit air conditions in conjunction with a solids mass flow rate and an air mass flow rate.

#### *4.2.3.1 diameter scale-up analysis*

Firstly, with respect the pipe diameter, Equations 4.17 to 4.19 indicate that the resultant pressure drop behaviour can be quite different, especially Equation 4.19 (and Equation 4.14) which is independent of pipe diameter. To further illustrate the effect of pipe diameter variations and the resulting magnitude of the pressure prediction of Equations 4.17 to 4.19, three dense phase tests from the Cement Meal (Table 12) were used, which were:

i. Flow condition S-1 (CM130-1), $m_s$ =4.09 kg/s, $m_a$ = 0.0806 kg/s

ii. Flow condition S-2 (CM130-8), $m_s$ =3.68 kg/s, $m_a$ = 0.0481 kg/s

iii. Flow condition S-3 (CM130-19), $m_s$ =1.18 kg/s, $m_a$ = 0.0208 kg/s

The Cement Meal air and solids mass flow rates were then 'scaled-up' using the dimensionless relationship defined in Equation 4.1 (and therefore a constant solids loading ratio is used) and plotted for variations in likely pneumatic conveying pipe diameters (i.e. from 0.05 to 0.54 mm) for a 50 m straight length of pipe. The results of the diameter variation analysis are shown in Figure 44 for Test S-1 ($m$* = 50.7), Figure 45 for Test S-2 ($m$* = 76.5) and Figure 46 for Test S-3 ($m$* = 56.7) with an extract of the diameter scale-up part of the code used in *Maple* displayed below:

```
> # The base diameter (d1),
# base air mass flow rate (Ma1) and
# base solids mass flow rate (Ms1)
Ms1:=3.68;
Ma1:=0.0481;
d1:=0.053;

# initial pipe diameter (d) value
d:=0.04;

 > #do loop to evaluate Pressure for different pipe diameters
for i from 1 by 1 to 50 do
   d:=d+0.01:
   Ma:=Ma1/d1^2*d^2;
   Ms:=Ms1/d1^2*d^2;

   # Evaluate the resulting pressure matrix 'X'
   # at length 'i' metres
   X[i]:=evalf(P):
end do:
```

*Extract of *MAPLE* software code used for diameter scale up analysis.

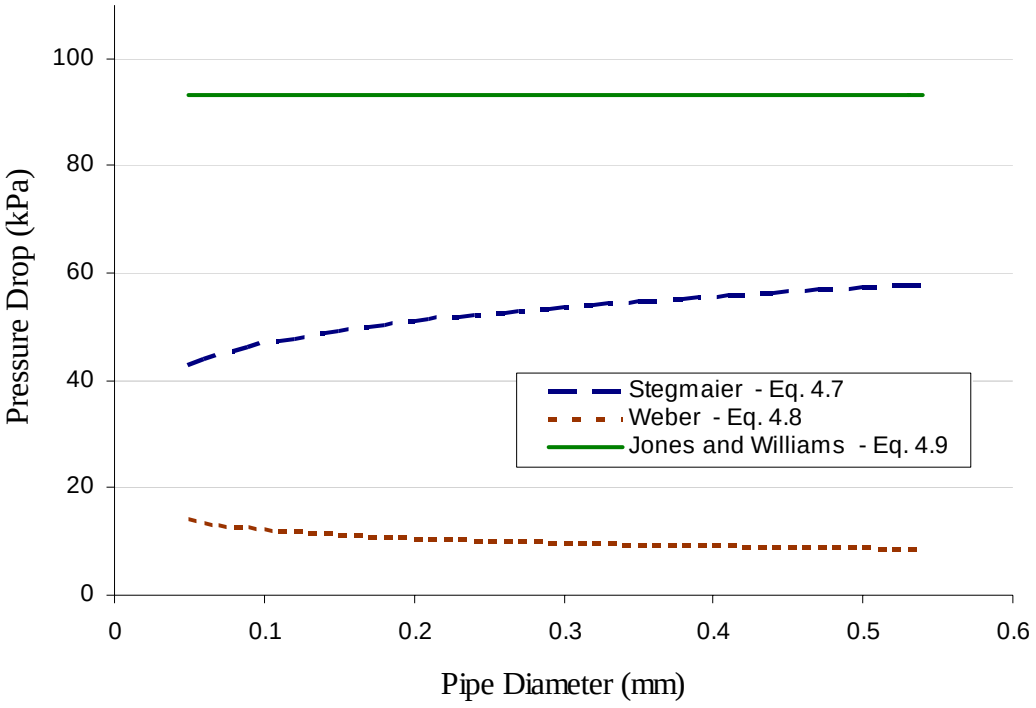


Figure 44, plot of pressure drop diameter scale up analyses S-1 for an $m^* = 50.7$ and $L = 50$m

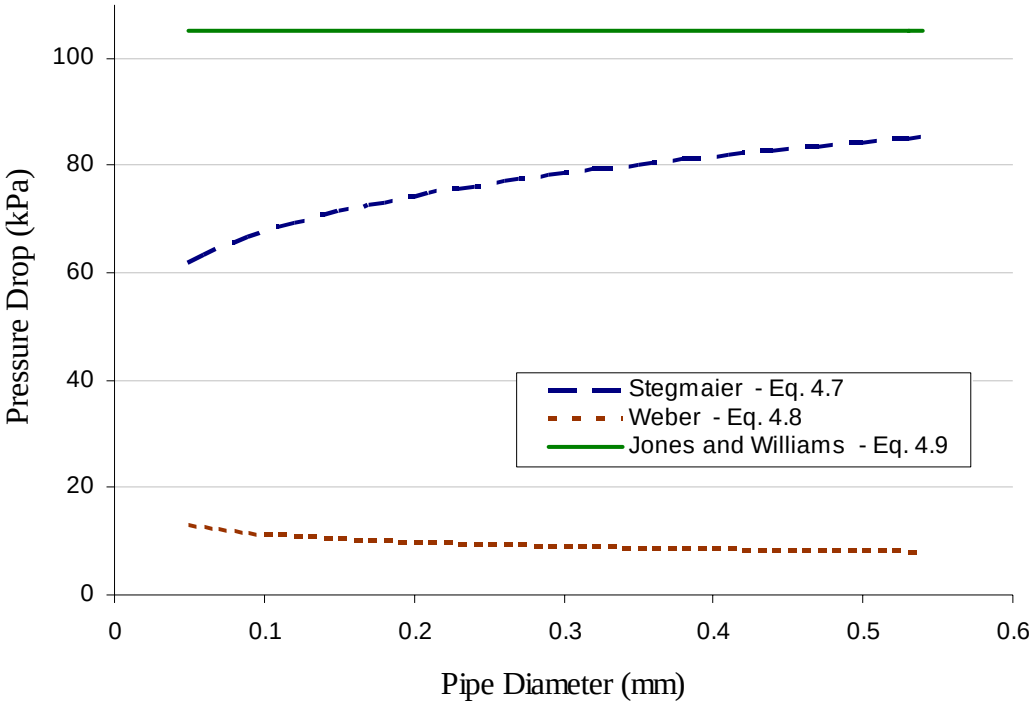


Figure 45, plot of pressure drop diameter scale up analyses S-2 for an $m^*$ = 76.5 and $L$ = 50m

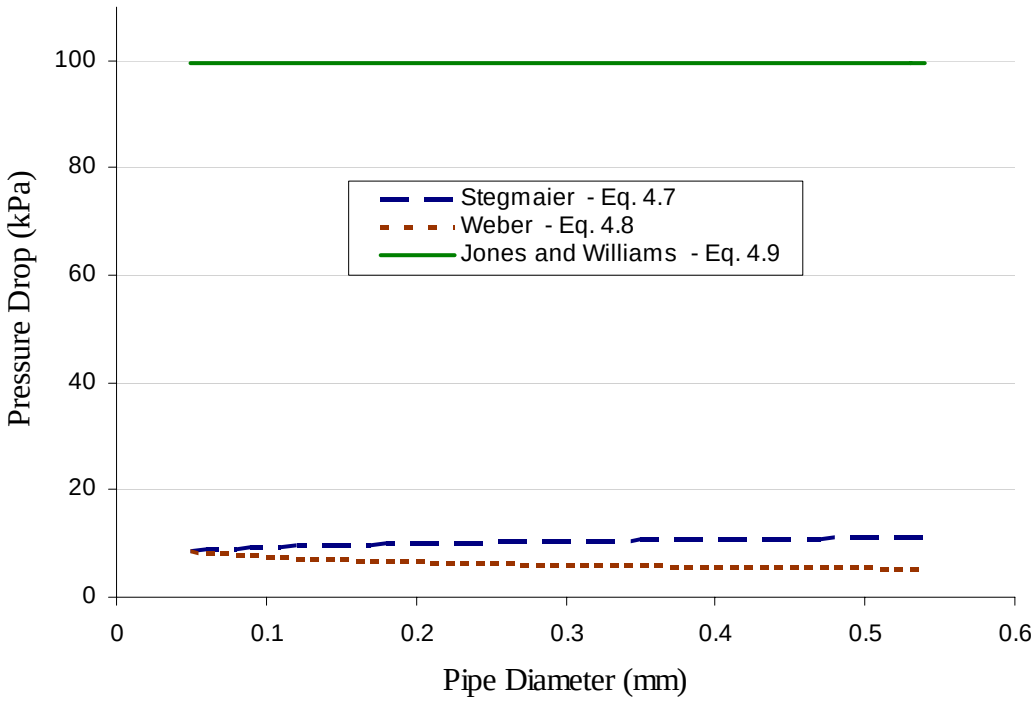


Figure 46, plot of pressure drop diameter scale up analyses S-3 for an $m^*$ = 56.7 and $L$ = 50m

For the pipe diameters analysed, the behaviour of the resultant pressure prediction for the Jones and Williams correlation is, as expected, constant with the pressure and comparatively large at around 100 kPa. However, the Weber correlation pressure drop analysis is relatively low in comparison, with all the predicted pressures below 20 kPa. The Weber results also show a slight pressure decrease with increasing pipe diameter during each analysis. Lastly, the Stegmaier pressure based analysis shows a wider variation in pressure drop prediction between the three tests with the general trend of increasing pressure drop prediction for increasing diameter. These differences in the pressure values and behaviour between the three solids friction correlations show the variation that different exponents can have on the resulting pressure drop. It is interesting to note that the Stegmaier correlation varies the most with changing diameter which means that this correlation diverges the most from the Equation 4.1 premise of constant pressure. Also, assuming that a constant pressure is available for increasing pipe diameter, the Weber correlation aligns more with the Wypych and Arnold [55] research which suggest that Equation 4.1 underestimates the tonnage rate for fine powders.

#### *4.2.3.2 length scale-up analysis*

The second part of the scale-up analysis behaviour investigates the effect of length on the pressure solutions. As for the diameter scale-up analysis, the same fluidised dense phase Cement Meal test data for air and solids mass flow rate were used (i.e. flow conditions S-1, S-2 and S-3). The conveying pipe diameter of 0.053 m was used for variations in pipeline length from 1 to 1000 m. The resulting solution for these tests can be found in Figure 47 for S-1 data analysis, Figure 48 for S-2 data analysis and Figure 49 for S-3 data analysis.

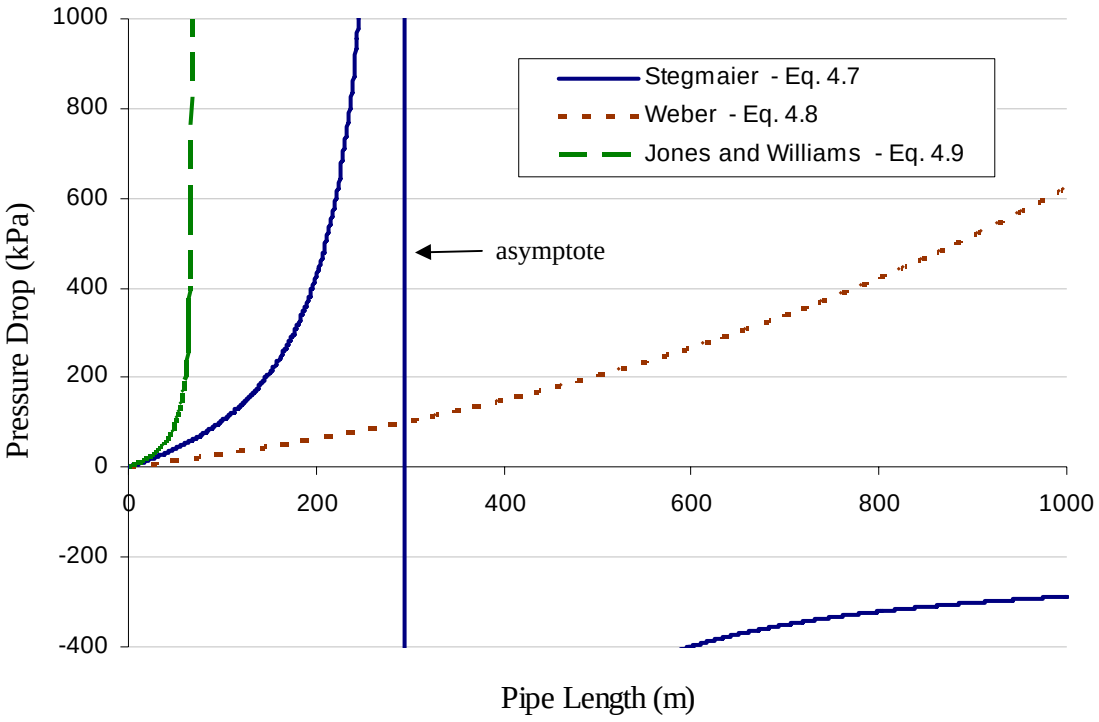


Figure 47, plot of pressure drop length scale up analyses S-1 for $m_s$ = 4.09 and $m_a$ = 0.0806 kg/s for $D$ = 0.053m.

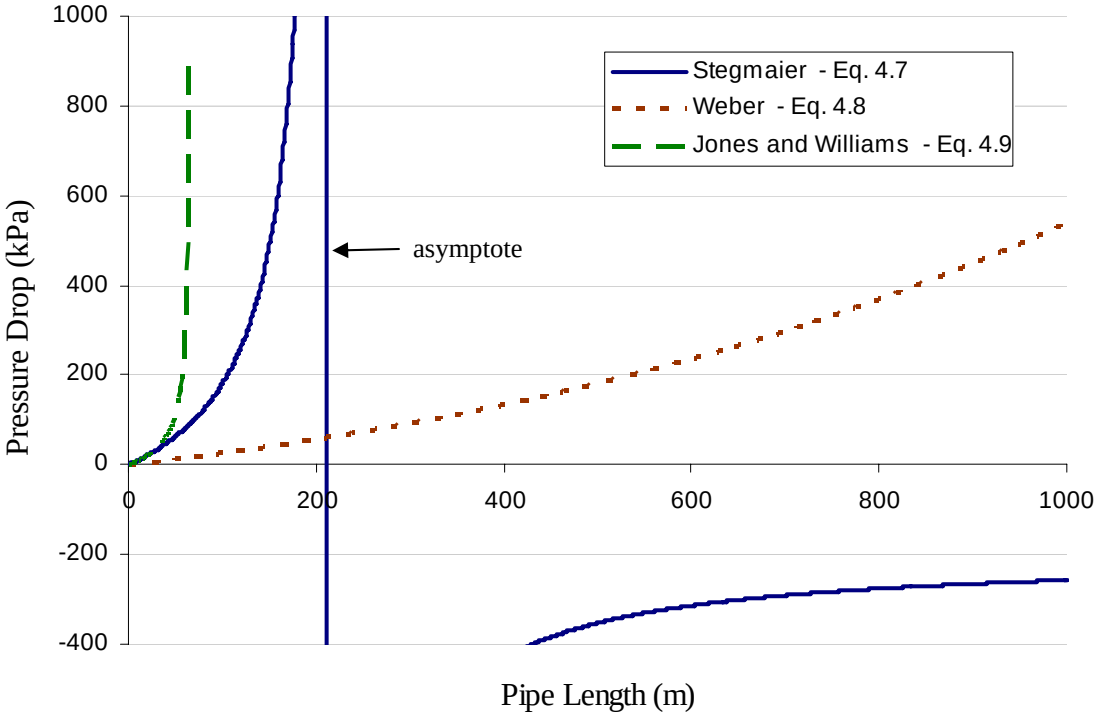


Figure 48, plot of pressure drop length scale up analyses S-1 for $m_s$ = 3.68 and $m_a$ = 0.0481 kg/s for $D$ = 0.053m.

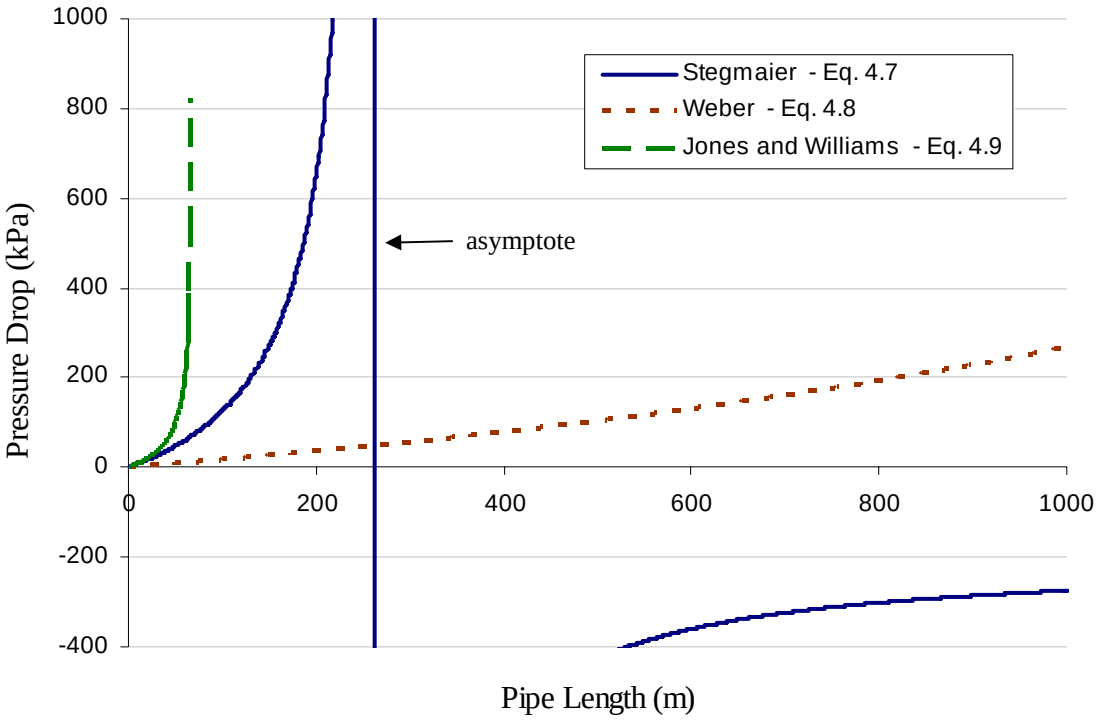


Figure 49, plot of pressure drop length scale up analyses S-1 for $m_s$ = 1.18 and $m_a$ = 0.0208 kg/s for $D$ = 0.053m.

The behaviour of the length based pressure drop solutions show that even though the behaviour in the Figure 47, Figure 48 and Figure 49 is similar for a particular solids friction correlation, significant differences in pressure prediction occurs between the correlations. For instance, the Jones and Williams based pressure drop response becomes unsolvable from 60 m to 70 m in length, while the Stegmaier based analysis shows asymptotic pressure behaviour between 200 to 300 m. The results of the Weber based pressure analysis shows that there are positive solutions for all the lengths and therefore Webers solids friction correlation remains relatively stable.

These differences in behaviour can be attributable to the different forms of the solids friction correlation. Firstly, it is relatively easy to see that the form of the Stegmaier pressure polynomial (Equation 4.17) has a vertical asymptote at $L = A_3/(A_4\ D^{0.1})$ and that the pressure solutions above this length are therefore negative. There is also a vertical asymptote for the Weber based pressure at $L = (-B_4/B_3)^{1/3}$, however, as this is a negative input (rather than a negative response as seen in the Stegmaier results), it is not relevant for the length analysis. Finally, the Jones and Williams correlation has a

vertical asymptote at $L = C_2/C_3$, however, due to the square root in the denominator, there are no real pressure solutions for $L > C_2/C_3$. Importantly, these results suggest that any correlation developed must be tested for asymptotic behaviour as this information may define scale-up limitations when using a specific correlation.

## *4.3 Comparison of Pressure Analysis with Experimental Tests*

As a final comparison of the pressure analysis behaviour, the solids friction correlations were used to predict the total pipeline pressure for the test data detailed in Chapter 3. This pressure analysis required equations to be used for the pressure components in vertical sections and bends. Briefly, for vertical sections, the additional pressure due to gravity will only occur in the upward flow sections of the pipeline. The technique to account for the vertical upward pressure component is generally either to choose an equivalent length approach or use a specific energy model. Similarly, equivalent length and specific energy based pressure models have typically been used for bends, which reflect the pressure required to re-accelerate the particles in and after the bend. For this study, the energy model technique for vertical sections and bends suggested by Chambers and Marcus [5] was used. The friction pressure drop components were determined using Equation 4.2 for the air and Equation 4.3 for the solids, with Equation 4.6 used to determine the air friction factor. The energy based bend pressure drop component is defined in Equation 4.20 with Equation 4.21 showing the equation for the vertical upward flow pressure.

$$\Delta P_b = (1 + m^*) N_b B \frac{\rho_a v_a^2}{2} \tag{4.20}$$

where $N_b$ is the number of bends and $B$ is the bend loss coefficient defined in Table 18.

Table 18, Bend Loss coefficients [5]

| Ratio of bend radius to pipe diameter | Bend loss coefficient |
|---|---|
| T-bends | 1.5 |
| 2 | 1.5 |
| 4 | 0.75 |
| 6 or greater | 0.5 |

$$\Delta P_v = m^* \rho_a g L_v \frac{v_a}{v_s} \tag{4.21}$$

where $L_v$ is the vertical upward flow length and $v_s/v_a$ is the solids to air slip velocity defined as:

$$\frac{v_s}{v_a} = 1 - 0.008 d_p^{0.3} \rho_{bl}^{0.5}, \text{ (note: } d_p \text{ is in mm)} \tag{4.22}$$

The results of the analysis for the Stegmaier correlation (Figure 50) show that the pressure is under predicted for all the data with the largest scatter occurring from 200 to 350 kPa (especially for the Cement Meal and the Flyash conveying tests). However, all the pressure results converge to a solution which is not too surprising as the Stegmaier results for variation in length (Figure 47 to Figure 49) suggested that unstable results for a 0.053 m diameter pipeline occurred at lengths greater than 200m and all the test pipeline lengths were less than 200m (i.e. 176m, 173m, 130m and 50m).

The results of the analysis for the Weber correlation (Figure 51) also shows an under prediction of the pressure with slightly lower prediction when compared to the Stegmaier results. The results of this pressure analysis correlates to the previous length scale up (Figure 47 to Figure 49) and diameter scale up (Figure 44 to Figure 46) analysis where the Weber pressure solutions are generally lower than the Stegmaier based pressure at pipe lengths below 200m.

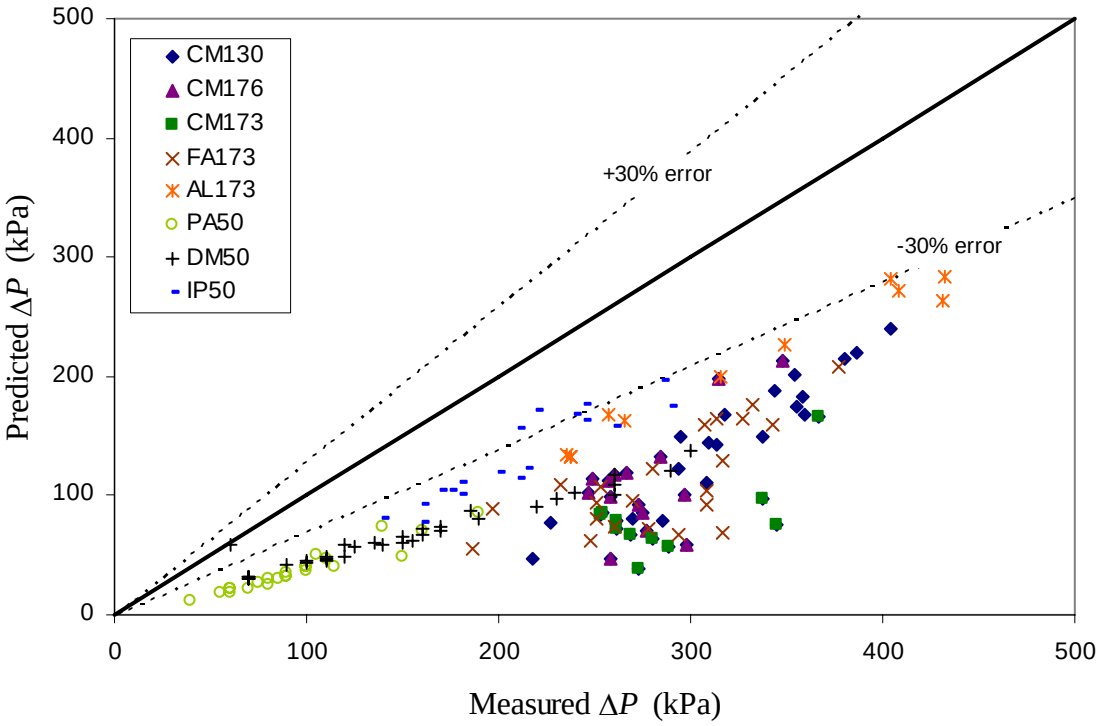


Figure 50, Stegmaier solids friction correlation based pressure drop analysis for Chapter 3 test data

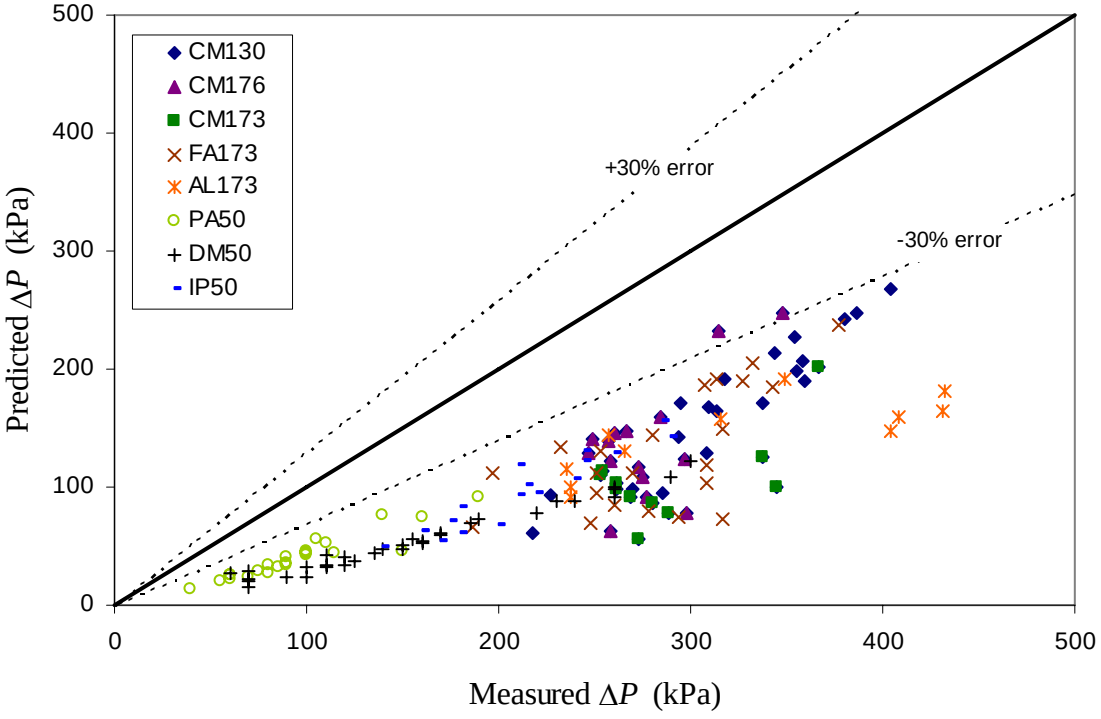


Figure 51, Weber solids friction correlation based pressure drop analysis for Chapter 3 test data

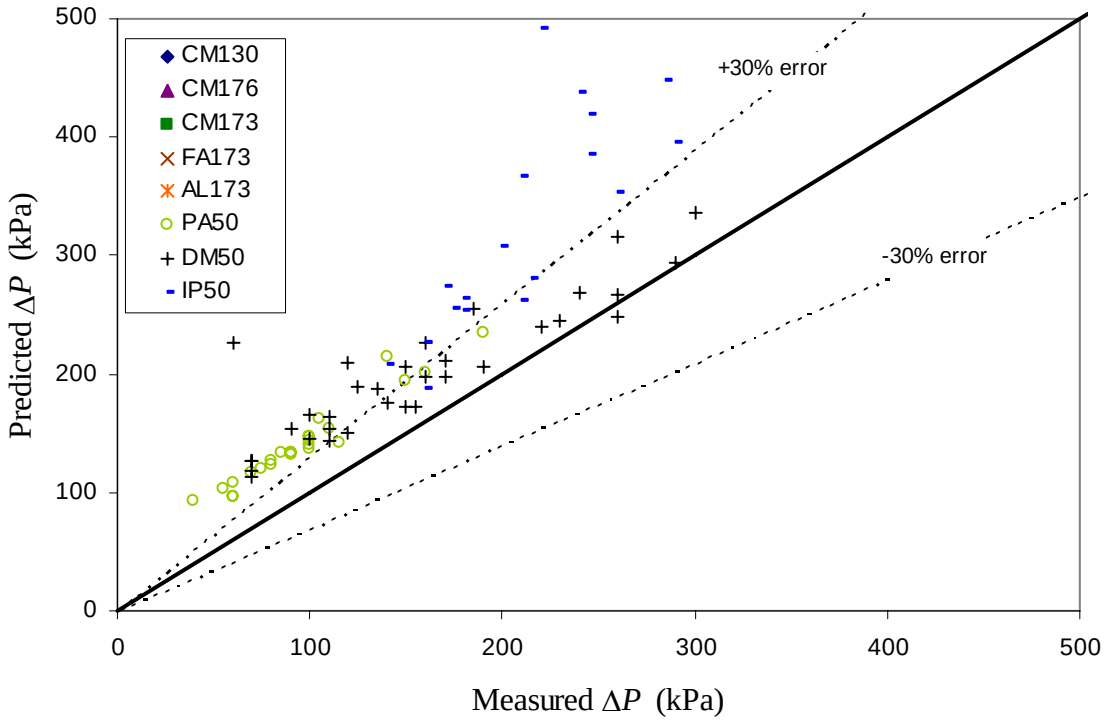


Figure 52, Jones and Williams solids friction correlation based pressure drop analysis for Chapter 3 test data

The response of the Jones and Williams based pressure prediction displayed in Figure 52 also follow the length and diameter scale up analysis (Figure 44 to Figure 49) as the pressure has significantly higher values than for the other two correlations for the tests in the 50m pipeline. Also, as suggested by the previous length scale up analysis (unsolvable at lengths greater than about 70m), the pressure prediction using the this solids friction correlation does not converge to any solutions for the 130m, 173m and 176m conveying tests.

Overall, the variation in pressure drop response behaviour between the solids friction correlations analysed can be quite different in structure, magnitude and stability even though the correlations themselves were generally quite accurate with respect to the test data (or simulated data) from which they were derived. This can be due to the range of test data used (e.g., dilute phase data used for the Stegmaier correlation), different material type (e.g., coarse material used as a basis by Weber) and/or limited variation in pipe geometry (e.g. data from only a 2 inch bore, 50 m length pipe used by Jones and

Williams) which can limit the range of pressure drop prediction that they can be utilised for, namely:

i. Different pipe geometries – particularly length and diameter scale up, and/or,

ii. Different flow conditions – i.e. dilute or either types of dense phase flow.

What can be seen from this analysis is that investigating the effect of variations in pipe diameter and length could possibly give insight into the limitations of the correlation on subsequent scale-up predictions. Finally, the value of the coefficients and exponents of the solids friction correlations can have a significant effect on the subsequent pressure drop and the changes in these values for both $m^*$ and $Fr$ is the focus of the following Chapter.

# CHAPTER 5: SOLIDS FRICTION – POWER LAW

As was seen in the previous chapter, even though the pressure drop calculations using the Stegmaier (Figure 50) and Weber (Figure 51) solids friction factors underestimated the actual pressure drop, the grouping behaviour of the calculated pressure drop showed aspects of proportionality (approximately 1:2) with the actual pressure drop. Also, for the Weber friction factor based scale-up analysis, solutions to the pressure equations always occurred and for this correlation (sees Figure 47 to Figure 49). These results provide some evidence that a similar approach for using a solids friction factor may provide a suitable parameter to describe solids resistance in fluidised dense phase conveying.

The aim of this Chapter was to ultimately develop a generic solids friction factor for fluidised dense phase conveying. Initially test data was used to determine a solids friction factor for each different material. A power law based friction factor was developed from the two non-dimensional parameters assumed to be most dominant in fluidised dense phase conveying; the Froude Number ($Fr$) and the solids loading ratio ($m^*$). The two parameters were also solely used in the Weber solids friction correlation.

The analysis conducted in the previous chapter has also shown that the values of the constants and exponents in each correlation will affect the subsequent calculated pressure drop value. Subsequently, an analysis of how the optimum coefficient and exponent values might be able to be established was conducted. The analysis of the effect of changes in solids friction power law co-efficient and exponents included diameter and length scale up analysis, in conjunction with a comparison between predicted and experimental pressure data. Finally, a generic solids friction factor was developed and compared with the experimental data.

## *5.1 Back Calculation of the Power Law*

The approach used in this analysis for determining the frictional resistance of the particles utilised the typical superposition technique defined by Equations 4.2 and 4.3 for the solids and air friction, Equation 4.20 for the bend effect and Equation 4.21 for the vertical upward flow (gravitational effect). Also, a global approach to the pressure

drop was used with the total pipeline pressure ($\Delta P$) calculated through the addition of the pressure components, i.e.:

$$\Delta P = \Delta P_{fs} + \Delta P_{fa} + \Delta P_b + \Delta P_v \tag{5.1}$$

To determine $\lambda_s$, a back calculation technique was used by subtracting the pressure drop components due to the bends, vertical section and friction due to air from the measured pressure drop, from which the pressure drop due to the solids friction (as defined by Equation 4.2) was obtained. The solids friction factor was then calculated by rearranging Equation 4.2 into the form:

$$\lambda_s = \frac{2D\Delta P_{fs}}{m^* \rho_a v_a^2 L} \tag{5.2}$$

Using the most dominant non-dimensional parameters for the solids friction correlation an empirically based friction factor was developed and found to have a power law relationship of:

$$\lambda_s = \frac{C}{m^{*a}\, Fr_a^b} \tag{5.3}$$

### 5.1.1 Co-efficient and exponent behaviour

To examine the effect of the coefficient and exponents of the solids friction power law correlation on subsequent pressure drop prediction, Equation 5.2 and Equation 5.3 were combined which expressed the solids frictional pressure drop as:

$$\Delta P_{fs} = C m^{*(1-a)} \frac{\rho_a v_a^{(2-b)}}{2} g^{\frac{b}{2}} D^{\frac{b-2}{2}} L \tag{5.4}$$

By initially looking at the structure of Equation 5.4, it is apparent that the value of exponent '*a*' should be between zero and one. This is because an '*a*' value of zero incorrectly suggest that the solids loading ratio is not a parameter of $\lambda_s$ and when $a = 1$

this incorrectly suggests that $\Delta P_{fs}$ is also independent of solids loading. Also, it can be seen that the value of exponent '*b*' will affect the kinetic weighting of the air flow energy because when '*b*' becomes larger the weighting of the velocity component decreases, which implies that momentum effect increases. The exponent '*b*' also has an impact on pipeline scale-up values when changes in pipeline diameter occur, however, the effect of the changes in this exponent value and pipe diameter on subsequent pressure values are less clear. For instance, if exponent '*b*' is less than two, then for a constant air and solids mass flow, an increase in diameter suggests a decrease in pressure drop, while the reverse is true if exponent '*b*' is greater than 2. A unique solution occurs (as was seen in the Jones and Williams correlation in Chapter 4.2.) when $b = 2$ as the solution to the pressure equation is a binomial and is independent of variations in pipe diameter. The final unknown parameter derived from Equation 5.4 is the co-efficient '*C*' which defines the scalar magnitude of the solids friction pressure drop equation (and the solids friction value as defined in Equation 5.3).

The pneumatic conveying tests detailed in Chapter 3 were used for the 'back-calculation' from which $\lambda_s$ was determined using Equation 5.2. Subsequently, the $\lambda_s$ correlation coefficient and exponents defined in Equation 5.3 were then evaluated for exponent '*a*' values from 0.1 to 0.9. Using a least square approximation, the corresponding co-efficient '*C*' and exponent '*b*' values were determined for each exponent '*a*' value. Also, the analysis showed how well the data fits the correlation through the use of the square of the 'Pearson's product' ($R^2$). The results of the coefficient for all the material analysis are shown in Appendix C. The Cement Meal pneumatic tests conveyed in the three different pipeline configurations are displayed on a semi-log plot below (Figure 53).

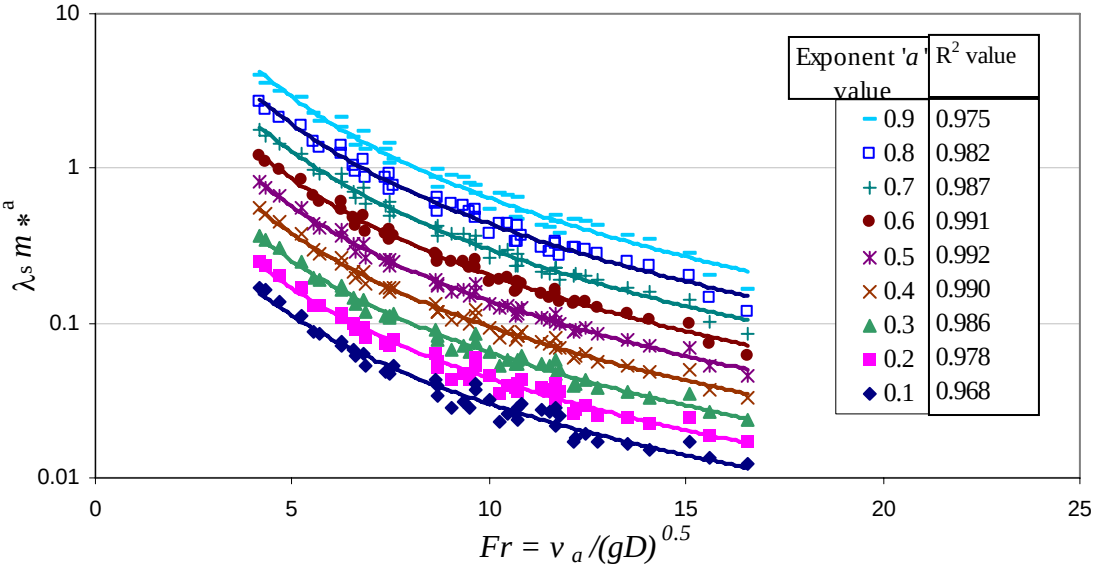


Figure 53, Cement Meal $\lambda_s$ relationship with $m*$ and $Fr$ with variations in the exponent 'a' value

From the results of the solids correlation analysis, it was found that there was a range of exponent '*a*' values which corresponded to the highest $R^2$ value (these $R^2$ values are displayed in Table 20, sub-chapter 5.2.1 and will also be discussed in sub-chapter 5.2.1). The other interesting feature from the analysis is that the trend lines representing the different '*a*' value correlations appear to be represented by a family curves on the semi-log axis. This observation suggested that a relationship may exist between the coefficient and exponents. Subsequently, the coefficient '*C*' and exponent '*b*' values were then compared to the variation in exponent 'a' from 0.1 to 0.9. The results for the relationship between the exponents and coefficient for Cement Meal shown in Figure 54 with the results for the other material shown in Appendix C.

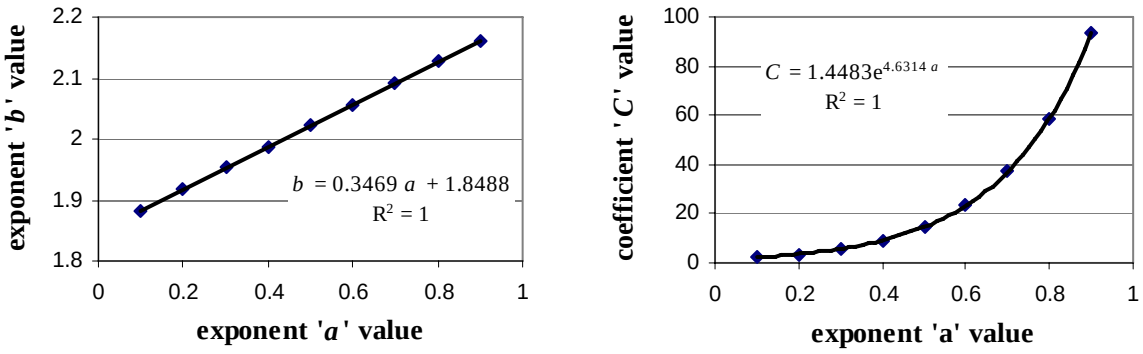


Figure 54, Cement Meal results for the solids friction power law relationship between the exponent '*b*' and coefficient '*C*' with the exponent '*a*'

From Figure 54, it can be clearly established that for a particular material, all the unknowns in the $\lambda_s$ power law correlation can be determined from a single value (i.e either '*a*', '*b*' or '*C*'). It is also interesting that the '*b*' exponent linearly decreases with '*a*' which means that the subsequent behaviour of the parameters defined in Equation 5.4 will be affected by the value of '*b*' as follows:

i. when '*b*' is increased to values higher than 2,
   a. the velocity becomes inverted and as $v_a$ increases then the pressure decreases,
   b. for a typical pipe diameter less than 1m, as *D* increases then pressure increases,
   c. gravitational exponent is greater than 1, and
   d. *m** weighting decreases (as '*a*' value increases).

ii. when '*b*' is decreased to values lower than 2,
   a. as $v_a$ increases then the pressure increases.
   b. for a typical pipe diameter less than 1m, as *D* increases then pressure decreases,
   c. the gravitational exponent is less than 1, and
   d. *m** weighting increases (as '*a*' value decreases)

which suggests that the most accurate physical behaviour of a pneumatic conveying system occurs for '*b*' values less than 2.

Also seen from Figure 54, the behaviour of the coefficient '*C*' shows an exponential increase with increasing '*a*' values. This '*C*' value analysis indicates a high sensitivity response to any minor error in predicting the appropriate exponent '*a*' value. Ultimately, this sensitivity has the potential to cause significant errors in the magnitude of the solids friction value and subsequent pressure drop prediction. From this analysis, the relationship between the solids friction correlation coefficient and exponents can be defined by the equations:

$$b = x_1 a + x_2 \text{ and } C = x_3 e^{x_4 a} \tag{5.5}$$

where the values of the constants $x_1$, $x_2$, $x_3$ and $x_4$ are specific for a bulk material, and are detailed in Table 19 for the Chapter 3 materials. A graphical representation of the relationship between the coefficients and exponents for the Chapter 3 bulk material are shown in shown in Figure 55 and Figure 56.

Table 19, Solids friction correlation constants defined in Equation 4.27

| Material Type | Material Code | $x_1$ | $x_2$ | $x_3$ | $x_4$ |
|---|---|---|---|---|---|
| Cement Meal | CM | 0.3469 | 1.8488 | 1.4483 | 4.6314 |
| Flyash | FA | 0.6344 | 1.5501 | 0.6446 | 5.3124 |
| Alumina | AL | 1.3269 | 1.0729 | 0.2602 | 6.8453 |
| Pulverised Fuel Ash | PA | 0.8140 | 1.0254 | 0.2840 | 5.8826 |
| Democrat Flour | DM | 0.6423 | 1.0626 | 0.4456 | 5.5031 |
| Iron Powder | IP | 0.9700 | 1.1475 | 0.3777 | 6.8618 |

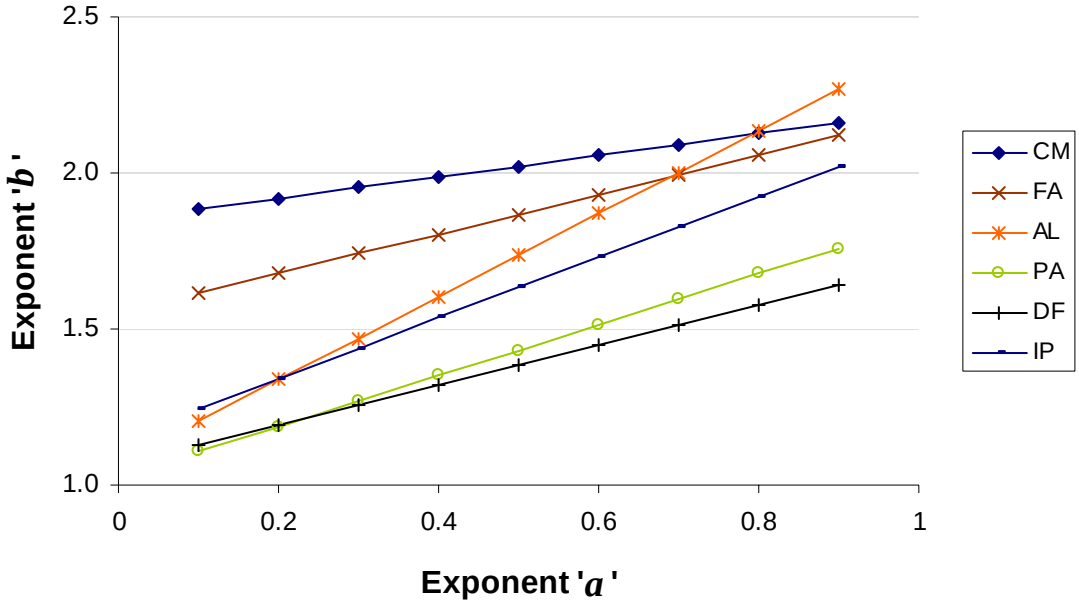


Figure 55, comparison of the Exponent '*a*' and '*b*' values

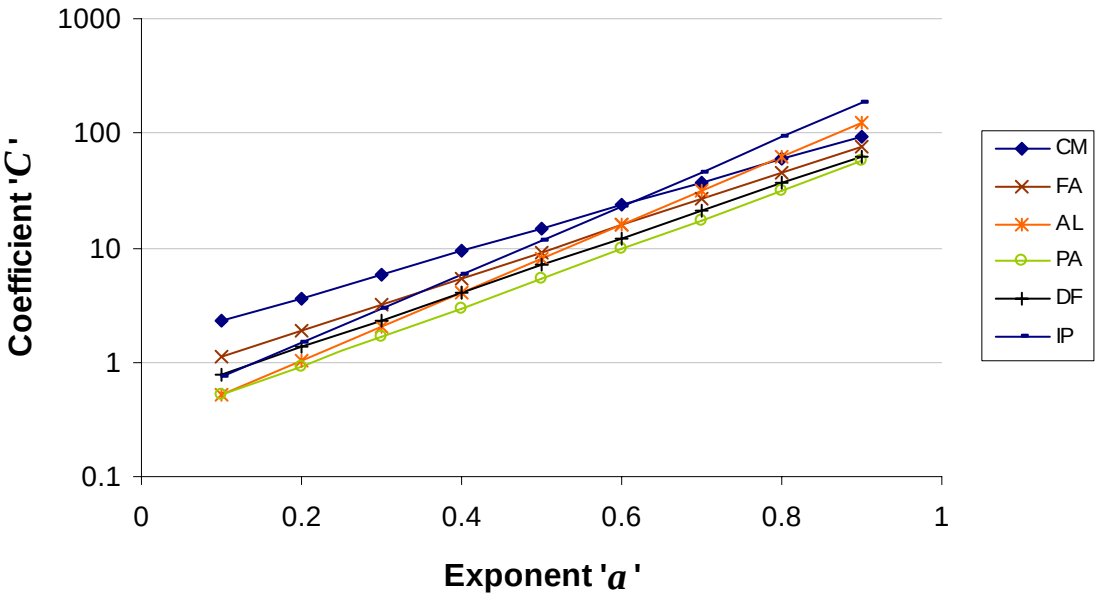


Figure 56, comparison of the Exponent '*a*' and coefficient '*C*' values

Table 19 shows that the constants (defined in Equation 5.5) vary for each given material, which indicate that a relationship between these constants and material properties or parameters (e.g. particle size, density, permeability, de-aeration, $P^*$, $N_c$, etc ) may be possible, which is discussed later in this chapter.

### 5.1.2 Scale-up behaviour

The purpose of this section is to look at the behaviour of the back-calculation technique to gain some insight into its effect on pipeline length and diameter scale up. Using the same process for the scale-up analysis conducted in Sub-chapter 4.2.3, the changes in coefficient and exponent values were analysed for pressure response stability with respect to pipe length and pipe diameter variations. Initially, an analysis was conducted using the Cement Meal flow conditions (S-1, S-2 and S-3) and procedures described in Sub-chapter 4.2.3. This analysis investigated the behaviour of variations in exponent '*a*' for horizontal straight sections of pipe using the solids friction power law. Incorporating the relationships between the exponents and coefficient defined in Equation 5.5 into solids friction power law, solids friction pressure drop (Equation 4.3), can be expressed as:

$$\Delta P_{fs} = \frac{K_1 e^{x_3 a} M_s^{(1-a)} M_a^{(1+a)} L}{\left(\frac{M_a}{\left(\Delta P_{fs} + 2P_0\right) D^{2.5}}\right)^{x_1 a + x_2} \left(\Delta P_{fs} + 2P_0\right) D^5} \tag{5.6}$$

where $K_1$ is constant for a particular bulk material and where $\Delta P_{fs}=\Delta P$ (straight pipe, neglecting air losses). Again, equation 5.6 shows a polynomal structure, however, no specific solution to the polynomial was found because there are no pressure solutions (either real or complex) for some length/diameter and exponent '*a*' combinations, as will be seen later in this chapter. Expanded as a polynomial, Equation 5.6 can be written as:

$$\Delta P_{fs} = K_2 \Delta P_{fs}^2 D^5 + K_3 \Delta P_{fs} D^5 - K_4 e^{k_3 a - k_2} \left( \frac{M_a}{\left(\Delta P_{fs} + 2P_0\right) D^{2.5}} \right)^{-x_1 a - x_2} M_s^{(1-a)} M_a^{(1+a)} L \quad (5.7)$$

where $K_2$, $K_3$, and $K_4$ are constant for a particular bulk material. The form of Equation 5.7 shows that the number of solutions to the polynomial is variable, depending on the bulk material specific $x_1$ and $x_2$ values and the exponent '*a*' value used.

#### *5.1.2.1 pipeline length variations*

The pipeline length was varied from 1 to 1000 metres to analyse the stability of each exponent '*a*' value from 0.1 to 0.9 in increments of 0.1. Although the pipe diameter used in this analysis is 0.053m, the 1000 m length was chosen so that the behaviour of the pressure prediction could be better observed. Currently, the maximum capabilities of current twin-screw compressor are around 1500 kPa, however, a pressure response to a value 10000 kPa was plotted to observe the pressure prediction behaviour. The pressure responses for the three flow conditions are shown in Figure 57 for flow conditions S-1, Figure 58 or flow condition S-2 and Figure 59 for flow conditions S-3.

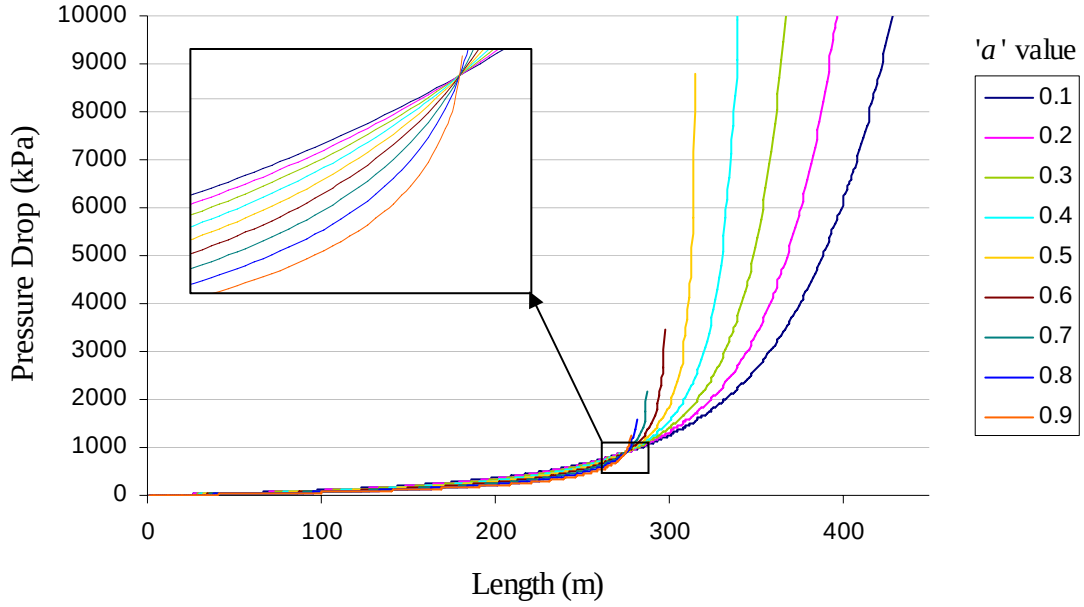


Figure 57, plot of Cement Meal pressure drop Vs length scale-up analyses for $M_s$ = 4.09, $M_a$ = 0.0806 kg/s and $D$ = 0.053m.

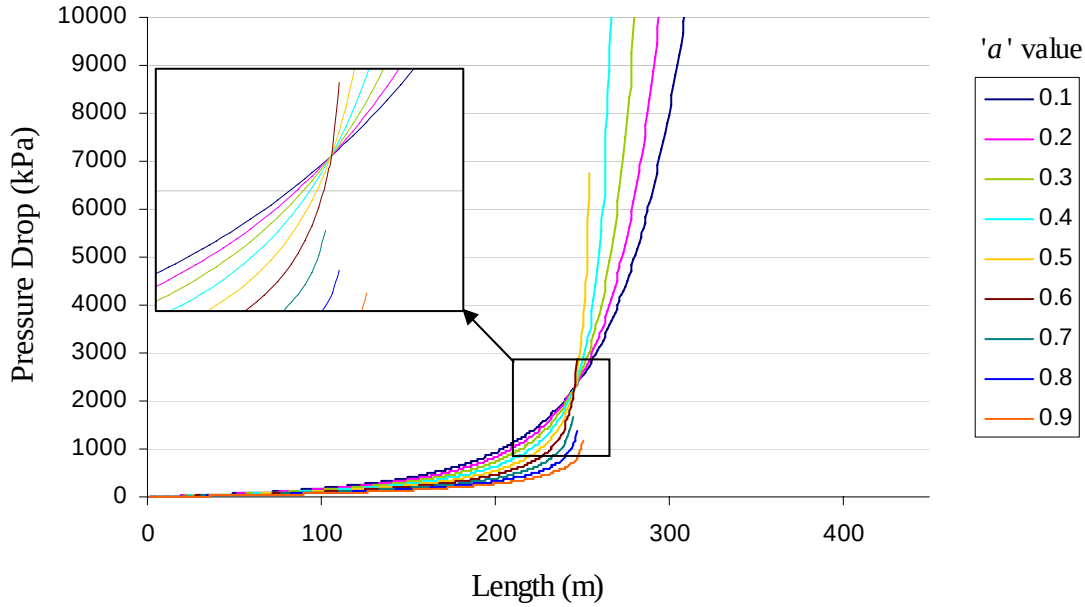


Figure 58, plot of Cement Meal pressure drop Vs length scale up analyses for $M_s$ = 3.68, $M_a$ = 0.0481 kg/s and $D$ = 0.053m.

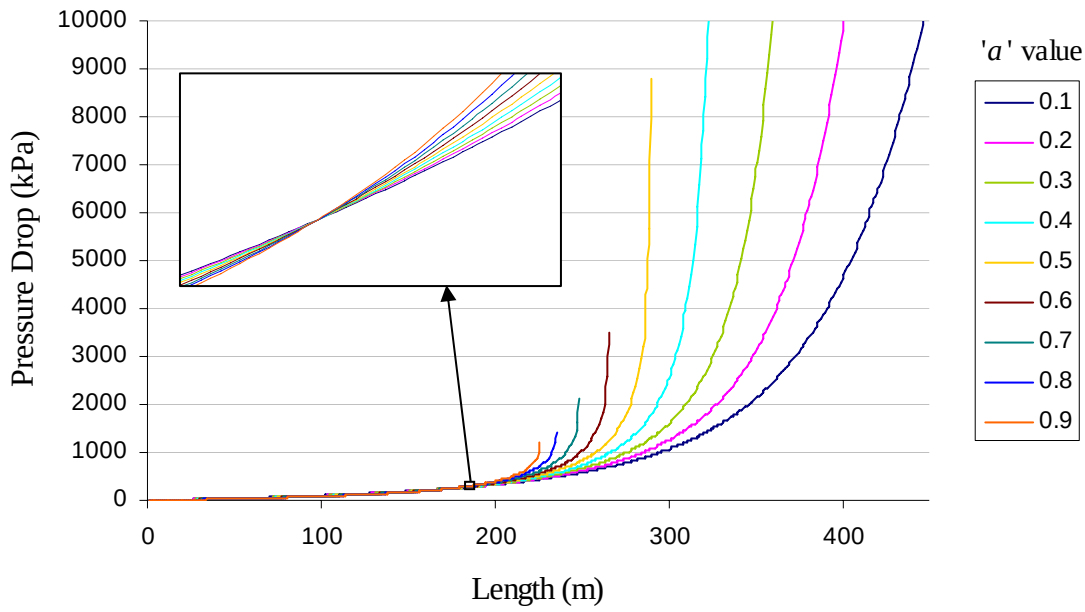


Figure 59, plot of Cement Meal pressure drop Vs length scale up analyses for $M_s$ = 1.18, $M_a$ = 0.0208 kg/s and $D$ = 0.053m.

Overall, the length scale up pressure solution analysis found first real recursive solutions for the polynomial for all lengths up to 1000 m for the exponent '*a*' values from 0.1 to 0.4. For '*a*' values 0.5 to 0.9, it was found that there were no solutions (i.e. no convergence) after a certain length and significantly, these non-converging '*a*' values occur for corresponding exponent '*b*' values greater than 2. Also, there is a distinct convergence point of the pressure responses which occurs for most of the variations in exponent 'a', except the 0.7, 0.8 and 0.9 solution for flow conditions S-2. These convergence points vary in length for the 0.053 m diameter pipe, depending on the flow condition, but no obvious relationship has been found yet. However the meaning of the convergence may represent the mathematical limitation of the accuracy of the scale-up method for the proposed flow conditions. It is unlikely that the convergence point represents a physical upper limit in conveying length as this convergence does not always occur. For example, as shown in Figure 60, an analysis for Flyash conveying of 5.56 kg/s (20 t/hr) of material with 0.3 kg/s of air through a 0.2 m pipe shows no convergence point, although similar Flyash material has been conveyed in similar pipe diameters and flow conditions up to 500 m [32]. The last behaviour to consider from the

length scale up analysis is the variation in pressure drop prediction for variations in '*a*', as the difference can be quite large (e.g. 800 kPa difference between $a = 0.1$ and $a = 0.9$ at $L = 200$m in Figure 58).

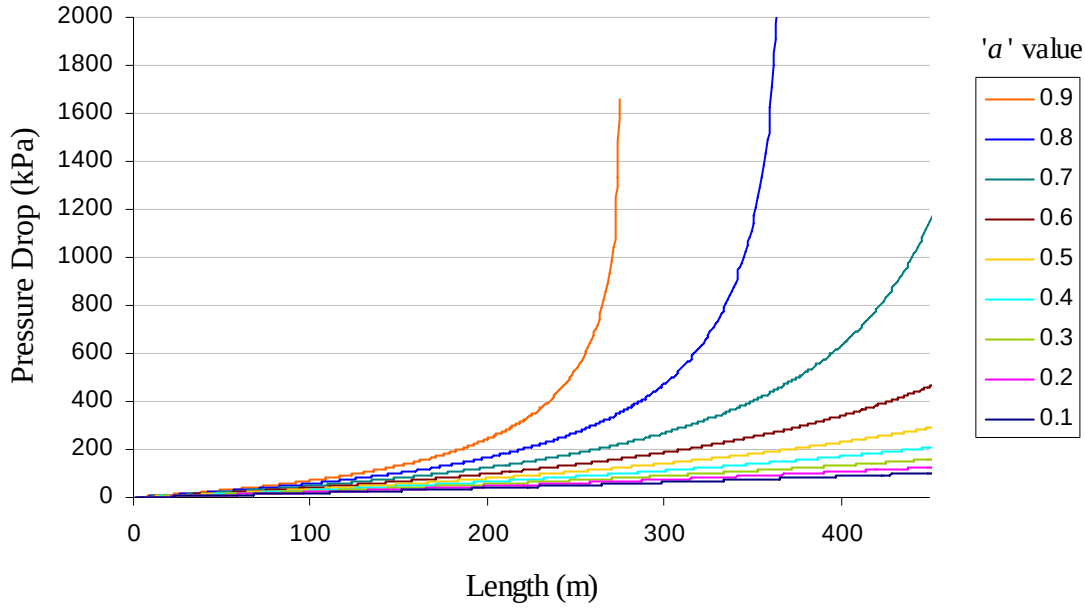


Figure 60, plot of Flyash pressure drop Vs length scale up analyses for $M_s = 5.56$ kg/s, $M_a = 0.3$ kg/s and $D = 0.2$ m.

A comparison of the all six test materials was also undertaken for length scale up analysis, with the results for the flow conditions S-1 from $0 < L < 500$ m and $0 < \Delta P < 2000$ kPa shown in Figure 61. Similarly to the previous Cement Meal analysis, for some exponent '*a*' values, it was found that after a certain length there were no pressure solutions and, again, this occurred for exponent '*a*' values which had corresponding exponent '*b*' values greater than 2. Also, a convergence point was sometimes observed with its location varying in length for different materials and different flow conditions. Generally, the convergence length for a specific flow condition is smaller for the material tested in the 50 m pipe length (Pulverised Fuel Ash, Democrat Flour and Iron Powder) than for the material tested in the 130, 173 and 176 m pipeline configurations, again, no definable relationship to this convergence length behaviour has been found. The convergence behaviour appears to be a mathematical anomaly associated with the structure of the solids friction correlation. However, it is apparent that stable pressure solutions occur for all the material at correlations where exponent '*b*' is less than 2.

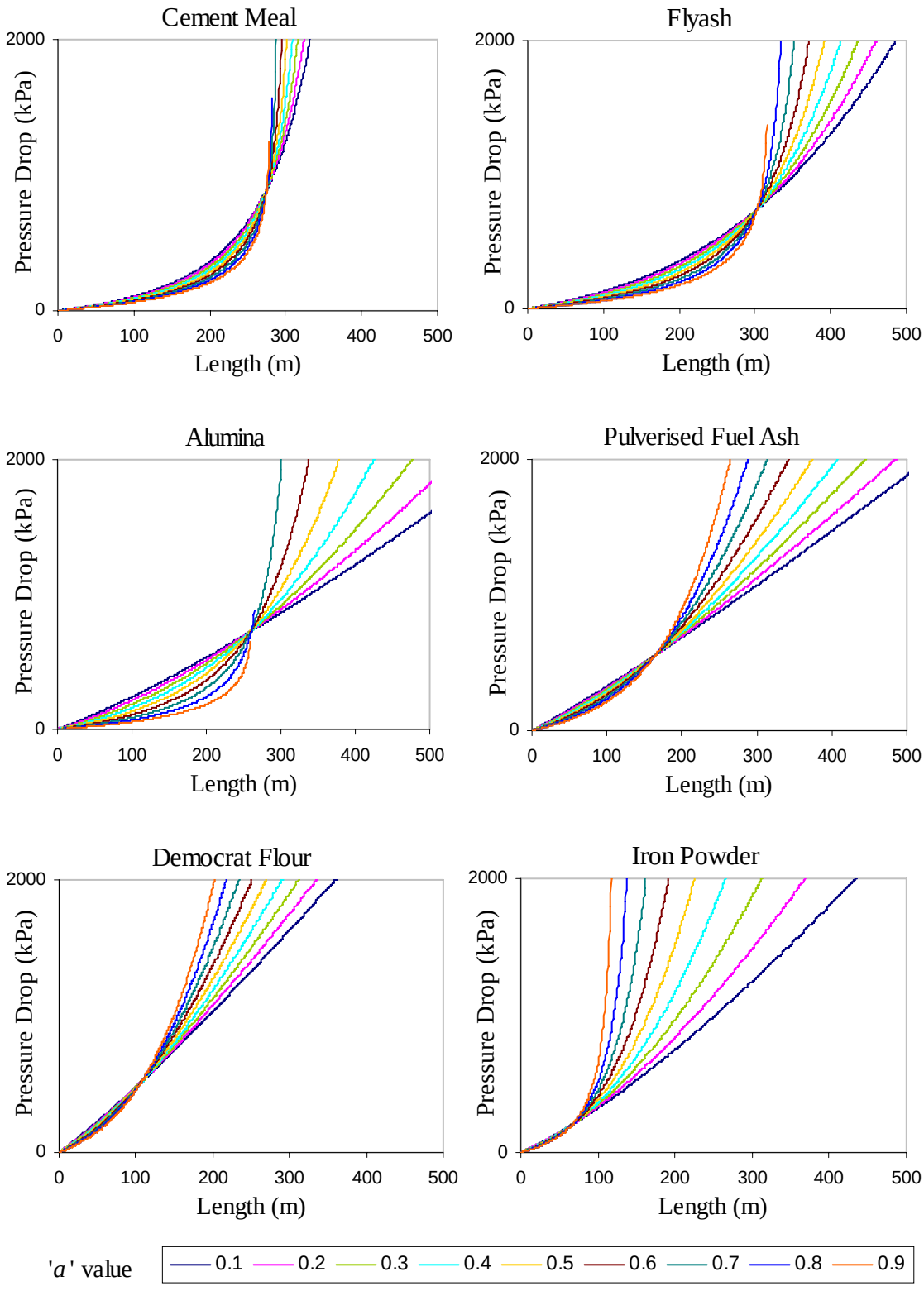


Figure 61, plot of Chapter 3 bulk material of pressure drop Vs length scale-up analyses for $M_s$ = 4.09, $M_a$ = 0.0806 kg/s and $D$ = 0.053m.

### *5.1.2.2 pipeline diameter variations*

For the diameter scale up analysis, the pipeline diameter was varied from 0.01 to 0.99 metres with the exponent '*a*' value varied from 0.1 to 0.9, in increments of 0.1. The Cement Meal air and solids mass flow rates were 'scaled-up' using the dimensionless relationship defined in Equation 4.1 and plotted for variations in different pipe diameters. The pipeline length analysed was at $L$ = 200m, however, the general behaviour of the pressure response for the diameter scale-up analysis was similar for different pipeline lengths. Also, the maximum value shown in the plots was chosen as 1600 kPa as this value was deemed sufficient to show the general behaviour for different flow conditions and different material. The results of the analysis for the three flow conditions are shown in Figure 62 for flow conditions S-1, Figure 63 or flow condition S-2 and Figure 64 for flow conditions S-3.

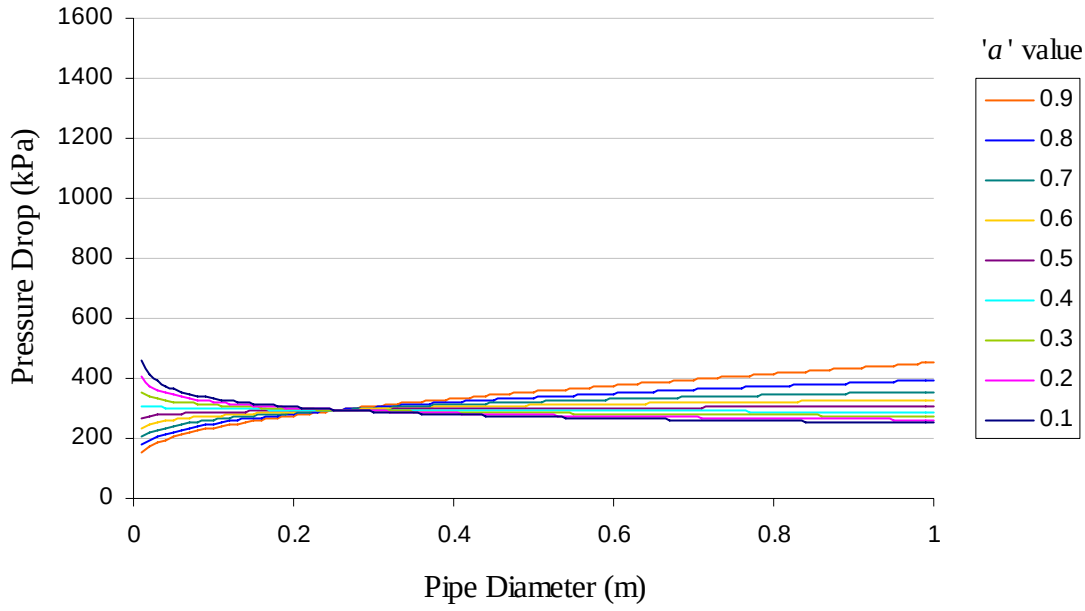


Figure 62, plot of Cement Meal pressure drop Vs diameter scale up for $m^*$ = 50.7 and $L$ = 200m based on S-1 flow conditions

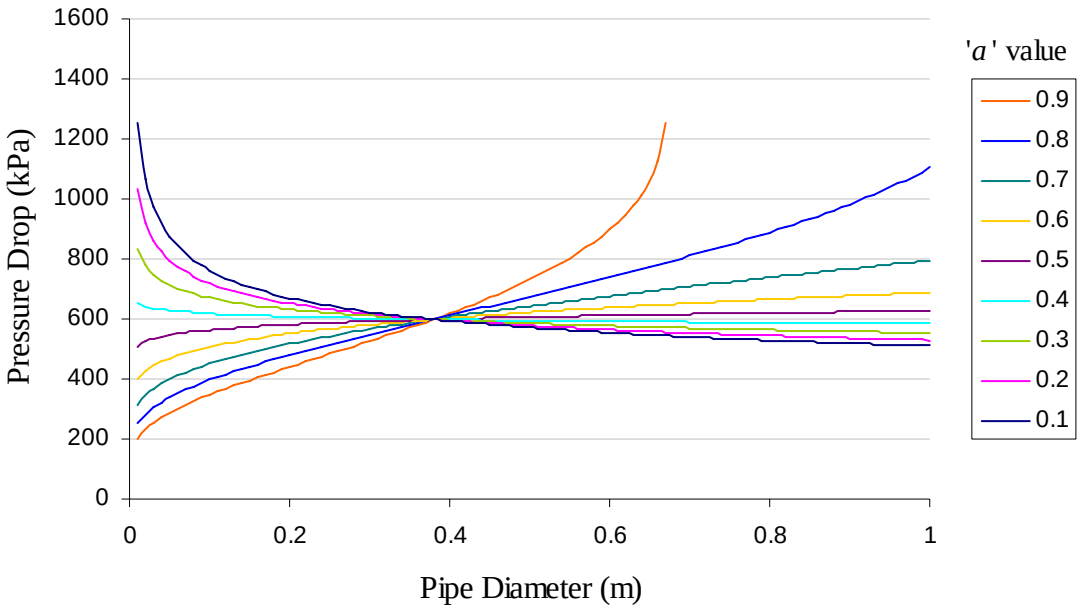


Figure 63, plot of Cement Meal pressure drop Vs diameter scale up for $m^*$ = 76.5 and $L$ = 200 m based on S-2 flow conditions

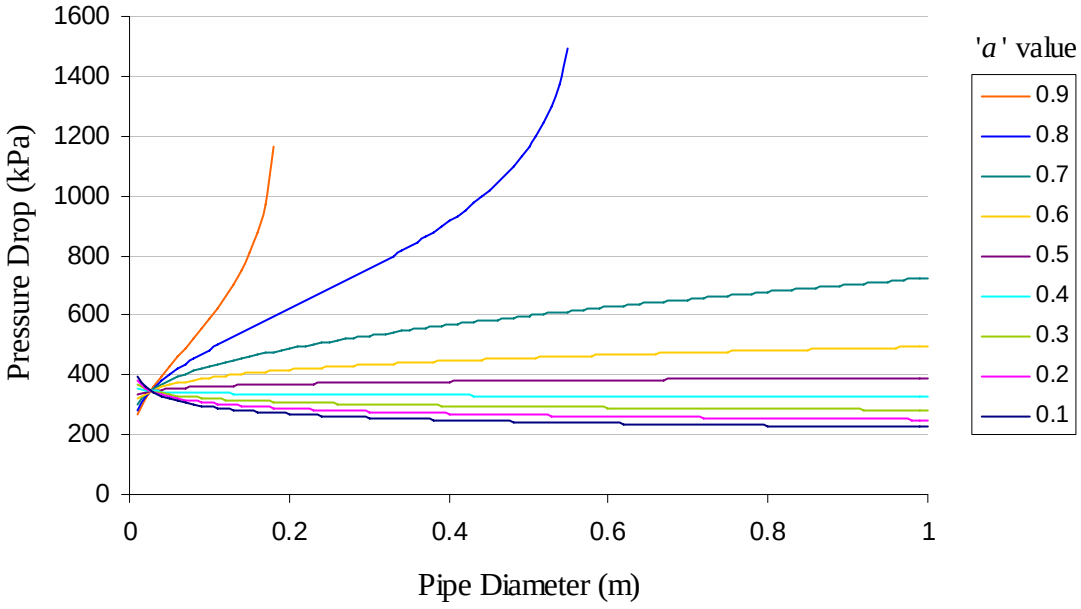


Figure 64, plot of Cement Meal pressure drop Vs diameter scale up for $m^*$ = 56.7 and $L$ = 200 m based on S-3 flow conditions

As suggested in the discussion on the structure of Equation 5.4, for all exponent '*a*' values that have corresponding '*b*' values less than 2, the pressure drop decreases for increasing pipe diameter. Also, for exponent '*b*' values less than 2, pressure solutions occurred for all the diameters analysed. Although the reverse is true in that the pressure increased with increasing diameter for exponent '*b*' values greater than 2, the pressure equation may not converge to a solution for increasing pipe diameter. Also, there is again a distinct convergence point of the pressure responses which occurs at a specific diameter for the entire exponent 'a' values analysed. These convergence points vary significantly in diameter location, depending on the flow condition, but no obvious relationship has been found yet. The similarities with the length scale up analysis are interesting with respect to the following behaviour:

i. A unique diameter pressure solution occurs at the convergence point which is independent of the solids friction exponents.

ii. The meaning of the convergence is again less clear as:

   a. it may represent the mathematical limitation of the accuracy of the scale-up method, or

   b. it may mean that this is the physical limit in conveying diameter for the specific conveying condition analysed.

iii. There can be significant variations in pressure drop prediction between '*a*' values (e.g. approximately 500 kPa difference between $a = 0.1$ and $a = 0.5$ at $D = 0.4$ m in Figure 58).

A comparison of all six test materials was also undertaken for diameter scale up analysis, with an example for the flow conditions S-1 from $0.01 < D < 0.99$ for a 200 m pipeline length with the results shown in Figure 65.

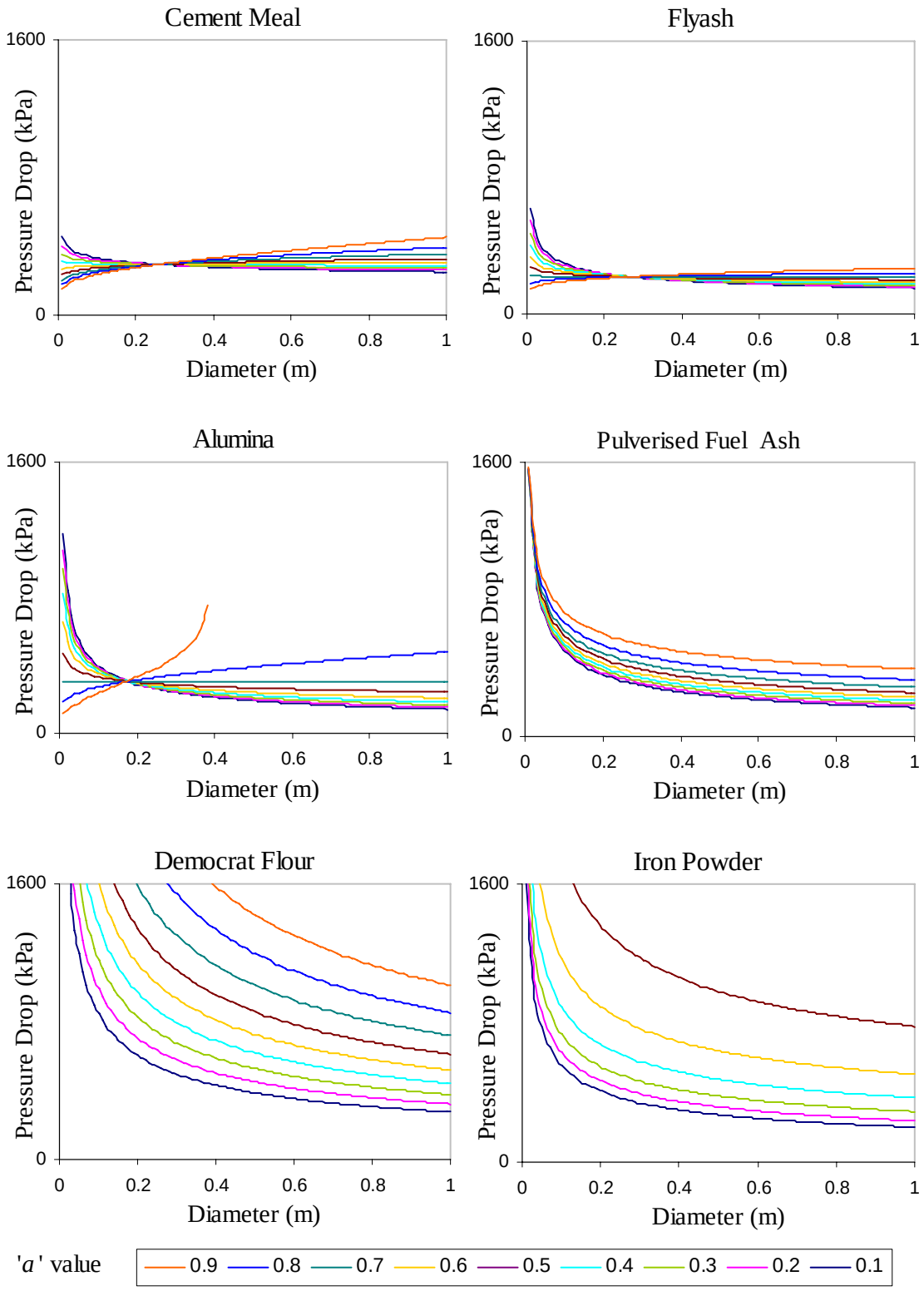


Figure 65, plot of Chapter 3 bulk material pressure drop Vs diameter scale up for $m^*$ = 50.7 and $L$ = 200m

There were again similarities of the diameter scale up analysis with the length scale up analysis, such as:

i. Pressure solutions were found for the entire exponent 'a' values that had corresponding '*b*' values less than 2.

ii. The '*b*' values that coincide with unsolvable pressure equations are always greater than 2.

However some '*b*' values greater than 2 have pressure solutions for all the diameters analysed (e.g. Flyash at $a$ = 0.8, $b$ = 2.058). Also, even though the diameter scale up analysis models the pneumatic conveying flow as incompressible steady state systems, due to the non-linearity of the polynomic equations, some unsteady/chaotic behaviour was observed generally for large diameter sizes (i.e. > 0.6 m) and exponent '*b*' values greater than 2. An example of this unsteady/chaotic behaviour is shown in Figure 66 for Alumina.

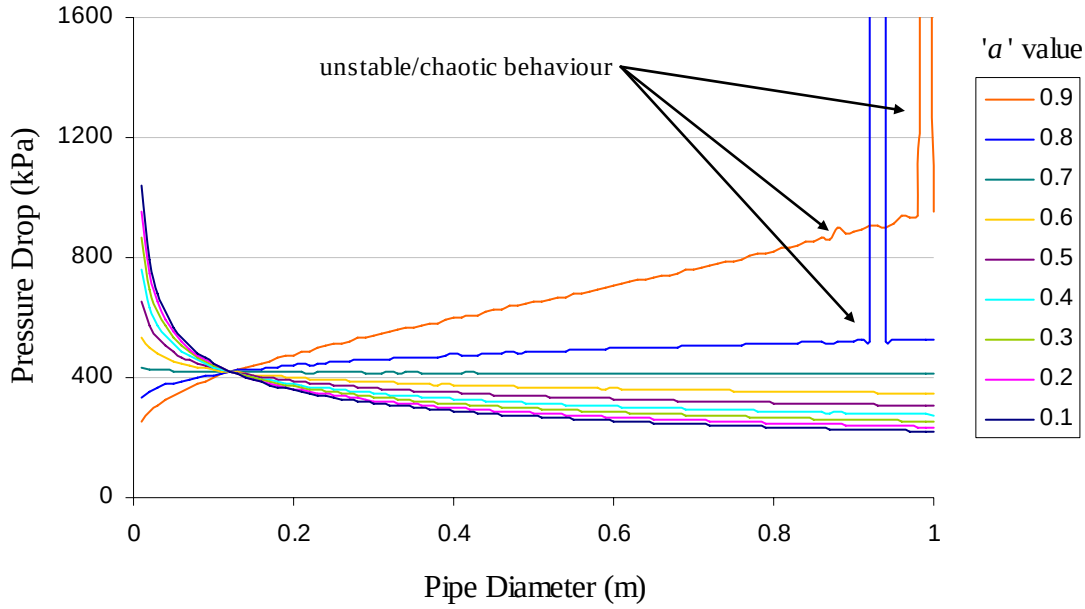


Figure 66, plot of Alumina pressure drop Vs diameter scale up showing unstable/chaotic pressure solutions for $L$ = 260m based on S-1 flow conditions

### 5.1.3 Summary of power law back calculation

The back-calculation technique used to calculate the solids friction power law correlation can initially appear to have a high degree of accuracy. However, the subsequent pressure solutions associated with the correlation can vary significantly and at times become unsolvable, unstable and even chaotic, depending on the values of the exponents and coefficient. To minimise the likely-hood of unstable equations occurring for scale up analysis, the research conducted in this chapter found that the solids friction correlation should have the following limits:

i. The exponent '*a*' value should be between 0.1 and 0.9,

ii. The exponent '*b*' value should be no greater than 2,

iii. Due to industrial compressor pressure capability rarely exceeding 1.5 MPa, realistically this pressure limit can also be associated with a maximum limit in pipeline length conveyability.

With respect to the variations in pressure solutions for the correlations with '*b*' values less than 2, the question of what are the optimal combination of coefficient and exponents needs to be addressed, which is discussed in the next Sub-Chapter.

Also, to avoid using different solids friction correlations that may exhibit this adverse behaviour or to analyse scale-up correlations which use pressure models (like Equation 4.3), then analysis similar to this is recommended. For example, Equation 5.9 is a solids friction correlation similar to Stegmaier's [47] correlation. This theoretical correlation has an unknown power law co-efficient '*C*' and exponents '*a*' and '*b*', but has a ($D/d_p$) ratio exponent equal to 0.1. For Equation 5.9, the '*b*' value at which the pressure value is independent of pipeline diameter will occur at $b$ = 1.96, as such the exponent 'b' value for this correlation should not be greater than 1.96.

$$\lambda_s = \frac{CFr_s^{0.5}}{m^{*a}\, Fr^b}\left(\frac{D}{d_p}\right)^{0.1} \tag{5.9}$$

## *5.2 Optimal Power Law Determination*

The previous sub-chapter highlighted there can be a significant difference in the calculated pressure for different values in the power law co-efficient and exponents. This sub-chapter investigates how the most optimal values of the co-efficient and exponents can be determined from which a reasonable accuracy in predicting the pressure can be achieved. Investigation of the information derived from the conveying tests led to the development of three proposed methods to determine these optimal values. Also, a comparison of these optimal value methods was conducted to assess if sufficient data (i.e. enough conveying trials) has been collected to produce a quality solids friction factor correlation.

### 5.2.1 Empirical optimisation methods

The approach of trying to determine optimal values for the solids friction power law centred on the exponent '*a*' value range of 0.1 to 0.9 using three different empirical methods. Firstly, an $R^2$ fit of the solids friction power law was used, based on the back calculation of the power law analysis conducted in Sub-Chapter 5.1.1 (e.g. Figure 53). The second method (standard deviation) and third method (trendline) were derived from a comparison between the pipeline predicted pressure solutions ($\Delta P_p$) and the measured pressure data ($\Delta P_m$) detailed in Chapter 3. The pressure components associated with the bend and vertical pipeline sections were again determined using Equations 4.20 and 4.21. An example of the comparison of the predicted and measured pipeline pressure for Cement Meal with '*a*' = 0.4 is shown in Figure 67.

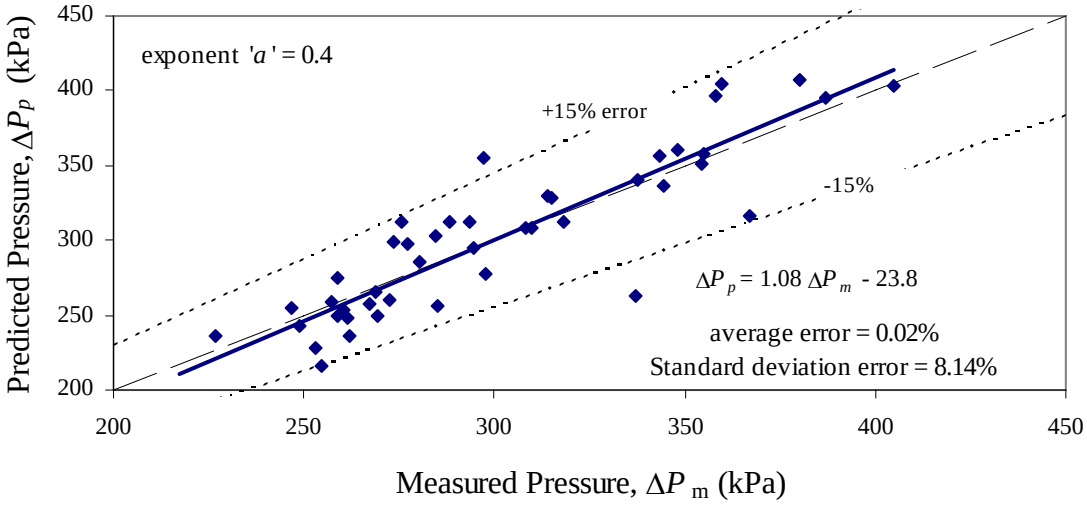


Figure 67, Cement Meal predicted and calculated pressure drop comparison for exponent '*a*' = 0.4

**$R^2$ method –** This method looks for the region in which the value of the square of the Pearson's correlation ($R^2$) of the power law trendline has the highest correlation (i.e. $R^2$ closest to 1). From the analysis shown in Figure 68 for the Cement Meal, the $R^2$ correlation values suggest that the best solids friction factor should be within the range $0.45 < a < 0.55$. Further analysis of the '*a*' range showed that the highest $R^2$ correlation of 0.992 occurred at the range $0.49 < a < 0.52$. A similar analysis was conducted for the other bulk materials, with all the optimal $R^2$ based results detailed in Table 20.

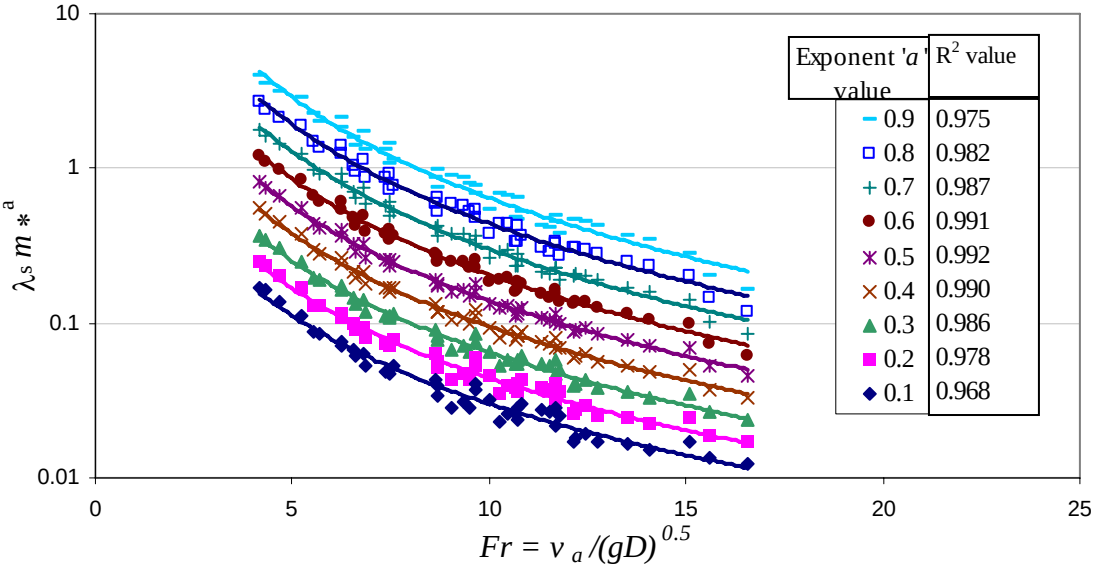


Figure 68, Cement Meal power law correlation showing the exponent 'a' value and corresponding $R^2$ correlation

**standard deviation method –** This method uses the values determined for the average predicted error value with the associated standard deviation error for each exponent '*a*' value. The error value was determined by calculating the difference between the predicted and measured total pressure drop (with respect to the measured pressure drop) and averaging the results for each different material for each '*a*' value. For example, the analysis shown in Figure 67 shows an average error calculated at 0.02 % with a standard deviation error of 8.12 %. A comparison of the average errors and the standard deviation error for $0.1 < a < 0.9$ is displayed in Figure 69 and shows that as the average error approaches zero, the associated standard deviation also decreases. For Cement Meal, the exponent '*a*' value is between 0.47 to 0.49 and is the range at which the standard deviation error is a minimum (7.88%) and the average error is closest to zero. The optimal region for the other bulk material is also detailed in Table 20.

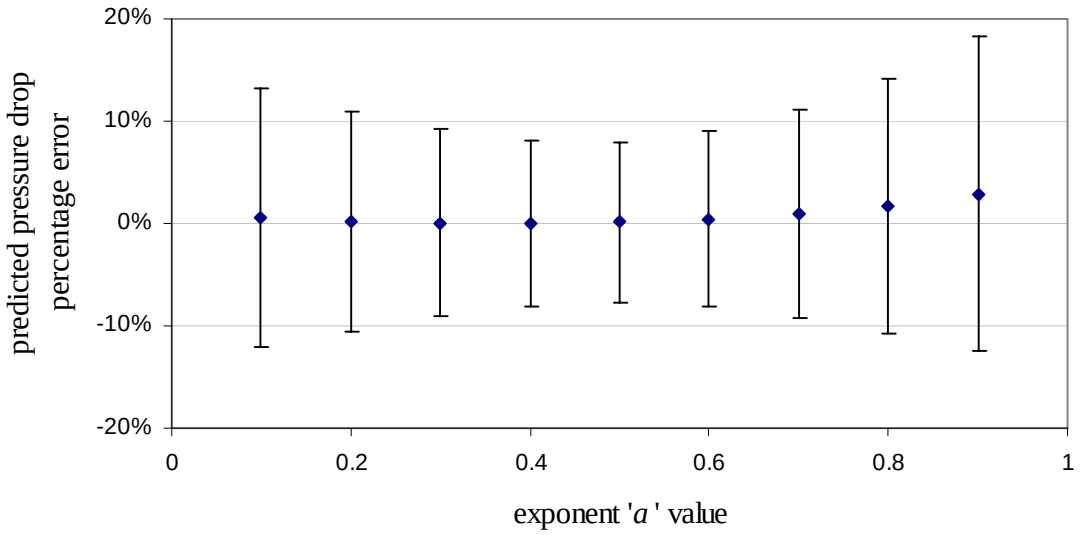


Figure 69, Comparison of the average percentage error of pressure drop prediction and associated standard deviation for Cement Meal

**trendline method –** Another interesting and important analysis of the pressure drop comparison of Figure 67 is the values of the slope and intercept of linear trendline. It is certainly mathematically true that the most accurate relationship between the predicted pressure drop and measured pressure drop occurs when the slope is equal to unity (i.e one) with the intercept equal to zero (i.e. through the origin). An analysis of $0.1 < a < 0.9$ is displayed in Figure 70 for Cement Meal and shows that the point at which the linear trendline slope is equal to one and the intercept is equal to zero occurs at approximately $a = 0.48$. Using this method, the optimal '*a*' value and associated coefficient '*C*' and exponent '*b*' for each material was determined and is shown in Table 20.

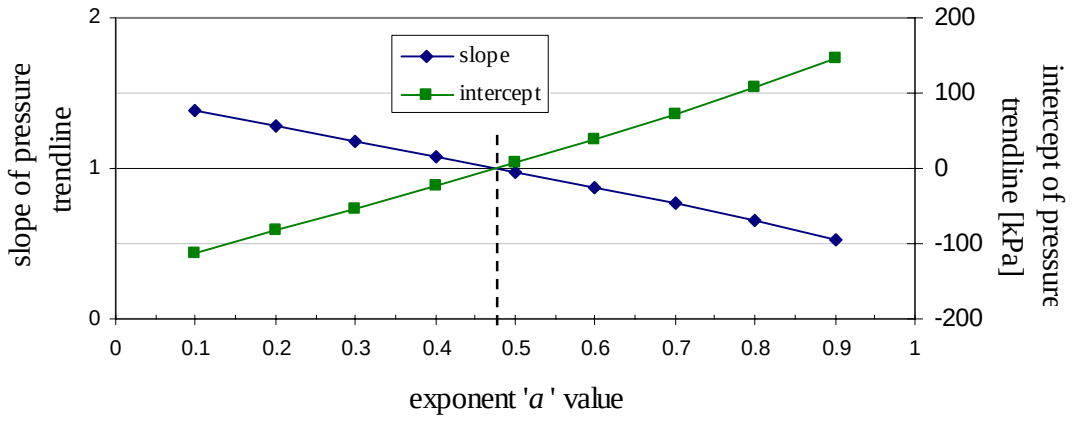


Figure 70, Cement Meal trendline pressure comparison analysis to determine the optimal exponent '*a*´ value

Table 20, results of the optimal exponent '*a*' analysis using different methods for the bulk materials detailed in Table 1

| **Material type** | | **Cement Meal** | **Flyash** | **Alumina** | **Iron Powder** | **Democrat Flour** | **Pulverised Fuel Ash** |
|---|---|---|---|---|---|---|---|
| **Material code** | | **CM** | **FA** | **AL** | **IP** | **DF** | **PA** |
| **Solids friction correlation method** | '*a*' range | 0.49-0.52 | 0.60-0.73 | 0.64-0.83 | 0.83-0.88 | 0.40-0.52 | 0.46-0.49 |
| | $R^2$ value | 0.992 | 0.999 | 0.998 | 0.988 | 0.951 | 0.924 |
| **Minimum standard deviation method** | '*a*' range | 0.47-0.49 | 0.57-0.59 | 0.68-0.69 | 0.77-0.79 | 0.30-0.37 | 0.37-0.39 |
| | St. dev | 7.88% | 4.01% | 3.29% | 6.08% | 10.5% | 6.86% |
| **Optimal Trendline method** | '*a*' value | 0.479 | 0.541 | 0.682 | 0.774 | 0.100 | 0.300 |
| | '*b*' value | 2.01 | 1.89 | 1.98 | 1.90 | 1.09 | 1.23 |
| | '*C*' value | 13.3 | 11.4 | 27.7 | 76.5 | 0.668 | 1.45 |

**Comparison of the optimal power law methods**

This comparison analysis essentially attempts to indicate whether sufficient numbers and range of operating parameters have been used in the pneumatic conveying experiments. Crucial in this technique is the assumption that if sufficient number and range of experiments where conducted, then there should be a good correlation between the different optimal methods. The closer agreement between the optimal methods also means that there will be a higher confidence level in the values of the solids friction coefficient and exponents and that this correlation sufficiently describes the solids friction in the pipeline.

To highlight any differences within the three optimal power law methods, the '*a*' values and regions detailed in Table 20 were plotted for each material in Figure 71. From Figure 71, it is easily seen that for the Cement Meal and Alumina, the different optimal methods agree very well, as all the '*a*' value results encompass each other. For the Flyash and the Iron powder there is a distinct area between different methods which indicates a lower confidence level, however, the two pressure based methods show good agreement. Disappointingly, there is a poor correlation between other two materials, Democrat Flour and Pulverised Fuel Ash, as these correlations are distinctively different in their predicted '*a*' values. Inspection of the $R^2$ values of these two products (see Table 20 – Democrat flour $R^2 = 0.951$ and Pulverised Fuel Ash $R^2 = 0.924$) reveal that the values are significantly lower than for the other four materials. The lower $R^2$ values indicate that these materials have much more scatter in the data, and therefore appear to reflect a correspondingly poor agreement in optimal exponent '*a*' value prediction.

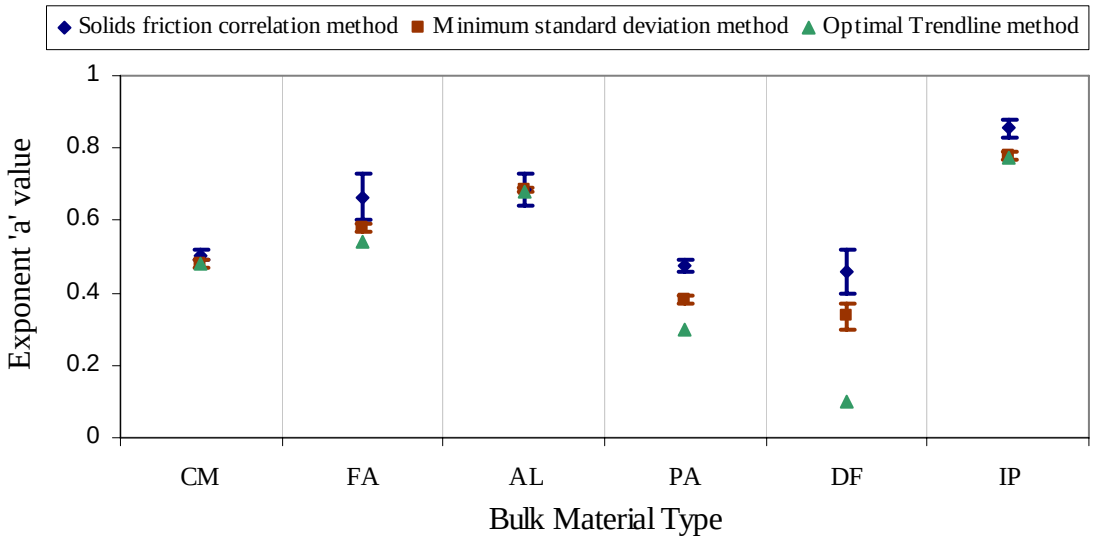


Figure 71, comparison of the optimal methods

### 5.2.2 Pressure drop prediction and bench scale based parameters

To illustrate the variation in solids friction correlation between different products, the optimal linear trendline values were plotted for each material, as shown in Figure 72. Obviously, from Figure 72, the difference in solids friction behaviour is mostly due to the properties of the bulk material, therefore, the next stage in the predictive process is to try to establish a generic solids friction model to reduce or eliminate the need for conveying the bulk material in a test pipeline. As stated previously in Chapter 2, dense phase pneumatic conveying capability can be predicted through bulk material parameter and air/particle interactions. It is two of these parameters, the Hausner Ratio (HR) and an air-particle parameter ($P^*$) developed by Sanchez *et al* [45], that have shown the most promise in developing a generic solids friction technique for fluidised dense phase flow.

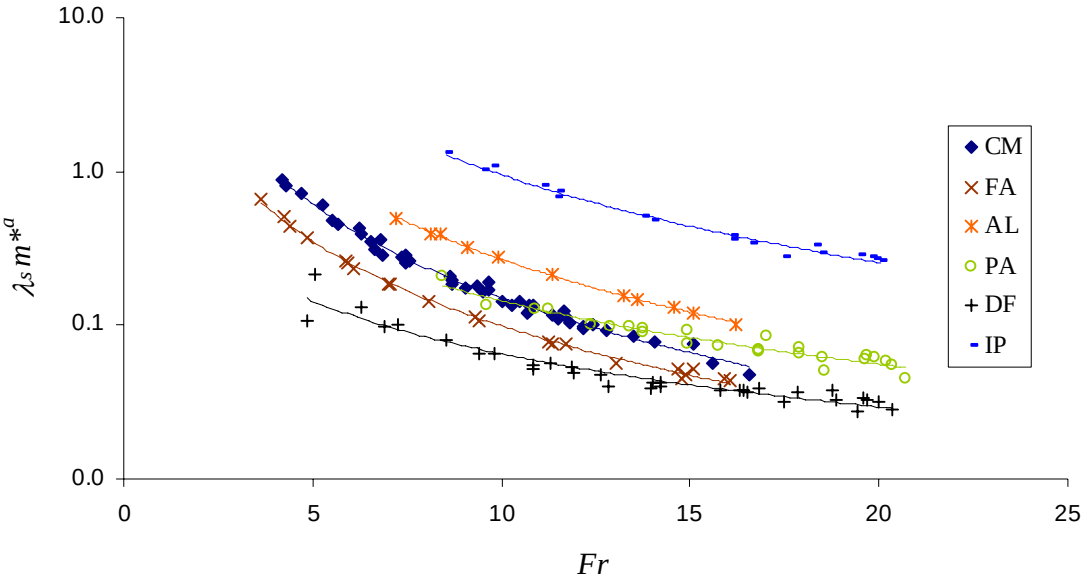


Figure 72, solids friction correlation using linear trendline values detailed in Table 20

Generally, the Hausner Ratio (*HR*) defines the packing efficiency between the 'loose poured' ($\rho_{bl}$) and tapped bulk density ($\rho_{bt}$) of a material and has been shown to be a good indicator of the flowability of a powder (Abdullah and Geldart [1]). *HR* is defined as:

$$HR = \frac{\rho_{bl}}{\rho_{bt}} \tag{5.10}$$

Sanchez's *P** parameter is based on particle parameters and the air permeability ($\psi$) of the material and is defined as:

$$P^* = \frac{\psi \rho_s \sqrt{g d_p}}{d_p} \tag{5.11}$$

From the analysis, the best exponent '*a*' was determined through an iterative method which calculated the most accurate slope for the relationship for an intercept equal to 1:

$$a = X_1 \frac{HR}{\rho_s} + 1 \tag{5.10}$$

Where $X_1$= -975.8 for the data presented here.

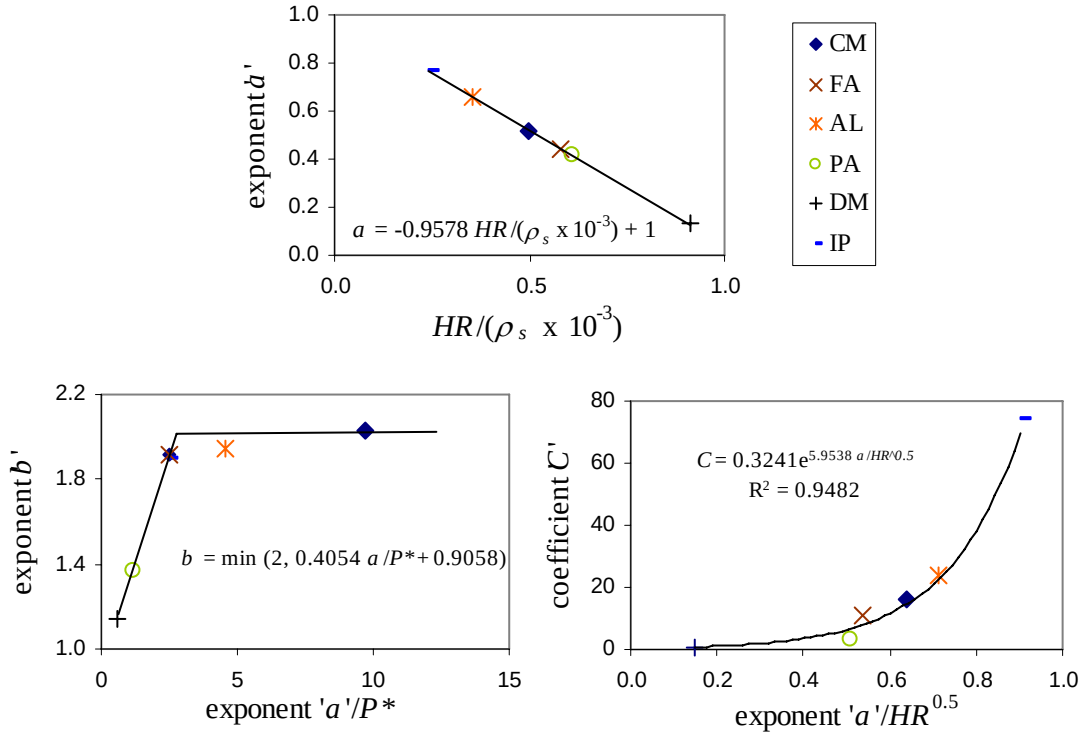


Figure 73, relationship between the solids friction correlation coefficients, *HR* and *P**

The exponent '*b*' and co-efficient '*C*' values of the solids friction correlations were also determined for the six different bulk materials, with the correlations with exponent '*a*', *HR* and *P**, as shown in Figure 73. This figure shows a linear trendline for exponent '*a*', a linear trendline with a maximum limit for exponent '*b*' and exponential increase for coefficient '*C*'. As can be also seen in Figure 73, '*b*' is as linear function with '*a*' up to a maximum of 2 and '*C*' has again an exponential relationship with '*a*'. The results of the frictional components where then incorporated into the pressure drop model defined in Equation 4.3, with the results shown in Figure 74.

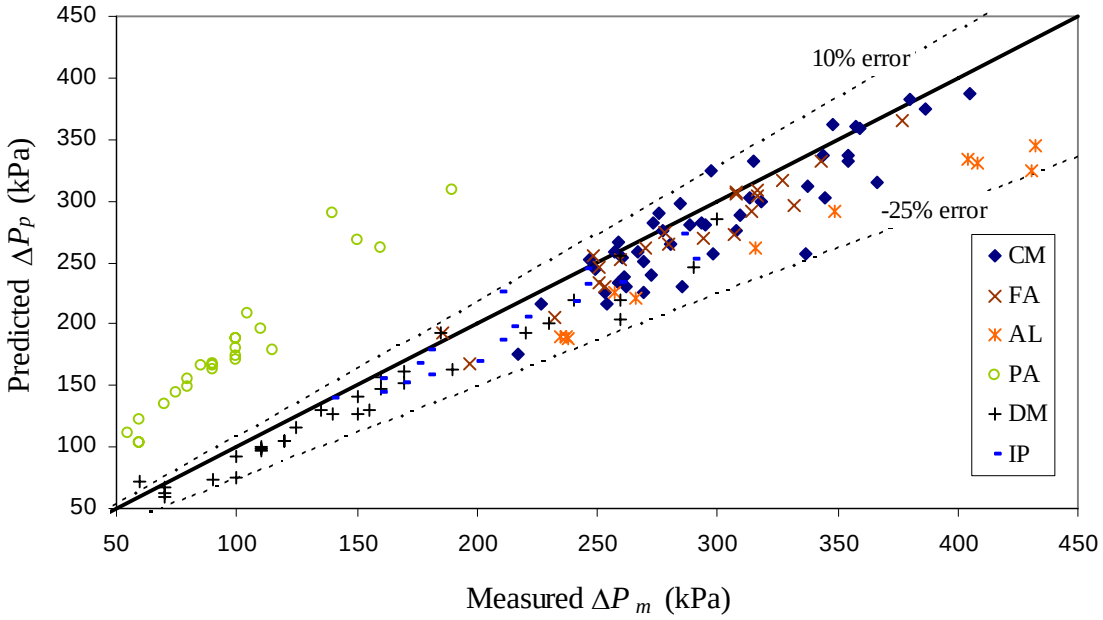


Figure 74, pressure drop comparison using the solids friction relationships shown Figure 73

Figure 74 shows that the vast majority of pressure test data for the Cement Meal, Flyash, Alumina, Democrat Flour and Iron Powder pressure drop can be predicted to within +10% and -25%. The results shown in Figure 74 also indicate that the method slightly under-predicts the pressure. The Pulverised Fuel Ash results show a significantly larger error (factor of 2), which can be traced back to the prediction of the '*C*' coefficient value. The Pulverised Fuel Ash predicted '*C*' value (6.69) was twice the actual required value (3.36) while there was less than 1% difference between the calculated and required corresponding '*b*' values. Some of the Pulverised Fuel Ash error may be due to problems with the reliability of the data used in this method, as suggested by the difference in optimal '*a*' values displayed in Figure 71 and the lowest $R^2$ value (0.924). However, the Democrat Flour pressure prediction is still accurate even though the variations in optimal '*a*' values are much larger than for Pulverised Fuel Ash and therefore the reasons for the errors are empirically less clear.

Overall, the analysis of the method for power law solid friction correlations showed good results for all the products except the Pulverised Fuel Ash, which is due, in part, to the inherent sensitivity of the exponential relationship between exponent '*a*' and coefficient '*C*'. As a final note, the accuracy in the measurement of the bulk material parameters used in this solids friction analysis require further investigation due to the sensitivity of the exponents and co-efficient derived from these parameters. This is because the errors, scatter or experimental distribution associated with measuring, analysing and calculating the bulk material parameters may produce to large a variation in subsequent co-efficient and exponents to achieve quality pressure predictions.

# CHAPTER 6: NUMERICAL MODEL FOR SOLIDS VELOCITY

To design an economic pneumatic conveying system the designer must try to convey the desired mass flow rate ($M_s$) of the material through the pipeline using the minimum amount of energy. This energy is proportional to the volumetric flow rate and pressure of the conveying fluid (or gas), which is produced by either a positive pressure (blower or compressor) or negative pressure (vacuum) system. The required pressure drop ($\Delta P$) across the pipeline is then determined from the output of the pressure system, which, in conjunction with the volumetric flow must achieve a transport velocity at or above the minimum transport velocity for the material. The minimum transport velocity will be different, depending on the mode of flow of the material being conveyed. For instance, dilute phase only capable material, the minimum transport velocity is usually defined as the pick-up or saltation velocity and represents the velocity to maintain a particle in suspension. However, for the dense phase flow, the minimum transport velocity is below the saltation velocity as the material flow is quite different.

For dilute phase only capable material, minimum transport or conveying velocity models have either been derived from experimental data or a single particle saltation parameter is used (eg [41] [21] [31] [41]) with two reviews of minimum conveying velocity conducted by Plasynski *et al* [36] in 1991 and Yi *et al* [59] in 1998. However, in fluidised dense phase conveying, the majority of particles are generally in contact with each other in an aerated state at the bottom of the pipe, with a dispersed dilute phase layer flowing in the top of the pipe. The height (or volume) of this aerated layer varies in height due to the gas expansion and associated gas velocity changes along the pipeline and also because of the geometry of the pipeline. As such, the minimum velocity of the aerated material must be defined using a bulk parameter approach which reflects its aerated state, rather than single particle models. However, no bulk-fluid models (either DEM-CFD, FEM-CFD) currently exist which have been successfully used to describe fluidised dense phase flow and subsequently the minimum transport velocity. This lack of adequate bulk-fluid capable modelling is why empirically based friction models are still the most prevalent approaches used for predicting the resistive

forces of the flow. As a result, the development of a numerical model was concurrently started with the research into the power law friction correlation to determine the velocity of the aerated layer throughout the pipeline. It was hoped that this velocity model would lead to an additional design tool for fluidised dense phase pneumatic conveying.

## *6.1 Current modelling*

In modelling the flow throughout the pipeline, researchers have developed models for either horizontal or vertical straight section of pipes. In the most recent models, Levy and Mason [23] developed a two-layer pneumatic conveying model based on a hydraulic two-layer concept of Wilson [54]. Levy and Mason's model utilised the fundamental principles of conservation of mass and momentum for fluidised dense phase flow in horizontal straight pipes. The most noticeable result of Levy's model was that the steady state bed height in the pipeline was predicted at a half fill level for either a thin level or thick level initial bed height condition. Rautiainen *et al* [38] developed an experimentally based one-dimensional equation system to describe vertical conveying from dilute to dense phase flows. Although these models give good agreement with experimental results, there currently are no models to describe a more complex pipeline geometry (i.e. incorporating bends in the pipeline). The bends generally used in fluidised dense phase conveying systems are small to long radius bends, and the model presented here only relates to these types of bends. For other types of bends (e.g. T bends, Botswana (or barrel) bends), other models will need to be investigated.

## *6.2 The Initial Continuum Model Approach*

In developing the model for fluidised dense phase conveying, the flow was modelled as a continuum with all the parameters based on the dense phase layer. Any frictional losses in the dilute phase were incorporated into the single friction factor for the continuum. A force equilibrium and conservation of mass model was developed to simulate a complex pipeline, which is based on the work of Roberts [42] for discharge chutes. The model then calculates the dense phase solids velocity ($v_s$) profile of the pipeline. When the velocity drops to its lowest point (or below zero) then the likely blockage point can be estimated.

The assumptions of this model were:

i. The flow is a fluidised material whose major parameter is the fluidised bulk density ($\rho_{fb}$).

ii. The flow is steady state and incompressible.

iii. The air and particle combination across the pipe is modelled as a continuum

iv. The pressure drop per unit length throughout straight sections of the pipe is constant (with the calculated bend factor pressure added to the pressure drop for each bend)

With regards to the preceding assumptions, clearly, the conveying gas is compressible and the bulk density of the material is probably not constant throughout the dense phase layer of the flow. However, an incompressible rationale is made as the current form of the solids flow model computes the solids flow conditions across a thin cross sectional slice of the dense phase layer (NB. The slice thickness (or step length) is determined by the algorithm the program, usually around 0.01m). Within this slice of material, the average bulk density condition provides a reasonable estimate of the aerated state of the material, with the gas compression effect relatively small due to the thin slice and also that the flow resistance is dominated by the solids friction.

### 6.2.1 Force equilibrium and conservation of mass

In a complex geometry pipeline, there are 2 basic sections require separate consideration; straight section and curved sections. For curved sections there are 5 sub-sections relating to the flow direction change of the material in the bend; horizontal to downward flow (*h-d*), downward to horizontal flow (*d-h*), horizontal to upward flow (*h-u*), upward to horizontal flow (*u-h*) and horizontal bends (*hor*). Any other configuration is a superposition of these to basic sections (e.g. inclined straight sections). An analysis of the *d-h* flow through a bend can be seen in Figure 75. A moving coordinate system ('t' and 'n' components), peculiar to each geometry studied, was used so that the tangential component of force is always parallel to the flow.

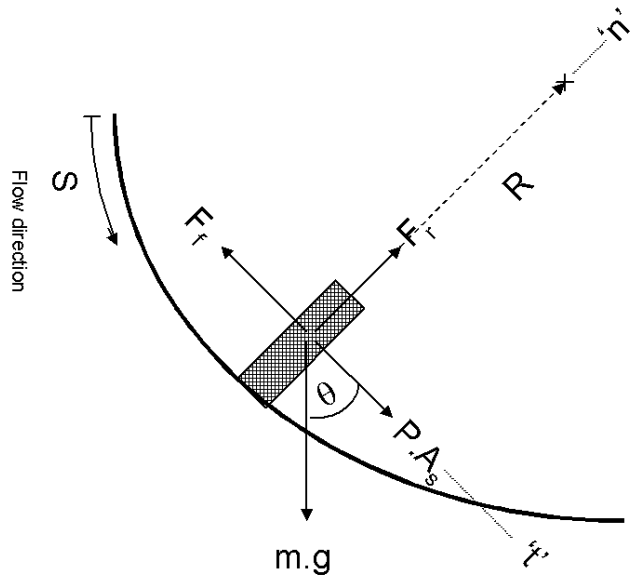


Figure 75, analysis of the forces for a curved pipe

### 6.2.2 Force equilibrium equations

From Figure 75, the force equilibrium equations can be derived for the tangential components (Equation 6.1) and the normal components (Equation 6.2).

$$\Sigma F_t = ma_t = P.A_s - F_f + mg\cos\theta = mv_s\frac{dv_s}{dS} \tag{6.1}$$

$$\Sigma F_n = ma_n = F_R - mg\sin\theta = m\frac{v_s^2}{R} \tag{6.2}$$

where the frictional force ($F_f$) and the radial force ($F_R$) are defined as:

$$F_f = \lambda_e F_R \tag{6.3}$$

$$F_R = m\left(\frac{v_s^2}{R} + g\sin\theta\right) \tag{6.4}$$

### 6.2.3 Conservation of mass

As the dense phase flow is modelled as incompressible flow, then from conservation of mass, each mass element ($m$ defined in Equation 6.5) can be calculated and $M_s$ (defined by Equation 6.6) is equal at all points throughout the pipeline. Also, as the fluidised bulk density is constant, then the solids cross sectional area solids velocity parameter ($v_s A_s$) at any point along the pipeline is also equivalent.

$$m = \rho_{fb} A_s S \tag{6.5}$$

$$\frac{M_s}{\rho_{fb}} = v_s A_s \tag{6.6}$$

## 6.3 Pressure Drop

For steady state flow, the pressure drop per unit length ($\Delta P/\Delta S$) is assumed constant (z) for straight pipes and at this early stage in the model, an added bend factor pressure drop will be used for the curved sections. Equations 6.7 and 6.8 detail the relationship for these sections.

$$\frac{\Delta P}{\Delta S} \approx \frac{P}{S} = z \qquad (\textit{straight sections}) \tag{6.7}$$

$$\frac{\Delta P}{\Delta S} \approx \frac{P}{S} = z(1+B) \qquad (\textit{for each bend}) \tag{6.8}$$

## 6.4 Differential Equations

Using Equations 6.1 to 6.8, the non-linear differential form of Equation 6.9 is derived, from which the velocity profile around a bend can be calculated.

$$v_s \frac{dv_s}{dS} = \frac{z(1+B)}{\rho_{fb}} - \lambda_e g\left(\frac{v_s^2}{Rg} + \sin\theta - \frac{\cos\theta}{\lambda_e}\right) \qquad (\textit{d-h bend}) \tag{6.9}$$

Using a similar analysis, the differential equation for the other 4 bends and straight sections are defined in Equations 6.10 to 6.14 with a more detailed derivation of the differential equations shown in Appendix D.

$$v_s \frac{dv_s}{dS} = \frac{z(1+B)}{\rho_{fb}} - \lambda_e g\left(\frac{v_s^2}{Rg} + \cos\theta + \frac{\sin\theta}{\lambda_e}\right) \qquad (h\text{-}u\ bend) \qquad (6.10)$$

$$v_s \frac{dv_s}{dS} = \frac{z(1+B)}{\rho_{fb}} - \lambda_e g\left(\frac{v_s^2}{Rg} + \sin\theta + \frac{\cos\theta}{\lambda_e}\right) \qquad (u\text{-}h\ bend) \qquad (6.11)$$

$$v_s \frac{dv_s}{dS} = \frac{z(1+B)}{\rho_{fb}} - \lambda_e g\left(\frac{v_s^2}{Rg} + \cos\theta - \frac{\sin\theta}{\lambda_e}\right) \qquad (h\text{-}d\ bend) \qquad (6.12)$$

$$v_s \frac{dv_s}{dS} = \frac{z(1+B)}{\rho_{fb}} - \lambda_e g\left(\frac{v_s^2}{Rg} + 1\right) \qquad (hor\ bend) \qquad (6.13)$$

$$v_s \frac{dv_s}{dS} = \frac{z}{\rho_{fb}} - \lambda_e g\left(\frac{\sin\theta}{\lambda_e} + \cos\theta\right) \qquad (straight\ section) \qquad (6.14)$$

A specific equation for each bend configuration was used (with a limit from 0° to 90° for each bend starting at s=0) as this method was more efficient for incorporation into the computational model. For Straight pipes, the angle of inclination ($\theta$) ranges from 90° for vertical downward flow, 0° for horizontal flow to -90° for vertical upward flow. At this stage of the continuum model development, analytical solutions can be derived for the straight section and horizontal bend equations. Numerical solutions had to be computed for all the other bend equations.

## *6.5 Initial Conditions*

The initial conditions for the model occur at the start of the pipeline where the superficial fluid velocity ($v_{f,,i}$) is calculated from the ideal gas law. Levi and Mason [23] used an initial gas to solids ratio of 0.9, for small particles, which appears to be of the scale of a dilute phase slip velocity ratio. As there appeared to be no specific fluidised

dense phase model, the slip velocity described by Chambers and Marcus [5] was used, and is defined as:

$$\frac{v_{s,i}}{v_{f,i}} = 1 - 0.008 d_p^{0.3} \rho_{bl}^{0.5} \tag{6.15}$$

Where $d_p$ is the average particle diameter **in mm** and $\rho_{bl}$ is the loose poured bulk density.

## *6.6 Behaviour of the Non-Linear Differential Equations*

The solutions to the differential equations for the bends were then computed using 'the fourth and fifth order Runge-Kutte algorithm in MATLAB to investigate the response of the axial velocity profile for different radii bends. The salient part of the MATLAB programming code developed is shown in Appendix E. Figure 76 shows some of the results of this program which shows a comparison of the velocity profiles for 0.05 m radius bends and 1 m radius bends, for the five different bend configurations.

In comparing the two plots in Figure 76, it can be seen that as *R* is changed from 0.05 m to 1 m, the radial force resisting the flow is reduced, as is expected. It can also be seen that the flow velocity changes as expected, depending on the orientation of the bend. For example, in the downward flow to horizontal bend (*d-h*), initially there is very little frictional resistance and the flow is dominated by acceleration due to gravity. As the flow moves around the bend, the radial force resistance is constant (for constant radius bends) with the frictional resistance increasing, reaching a maximum at the exit of the bend, where the flow becomes horizontal.

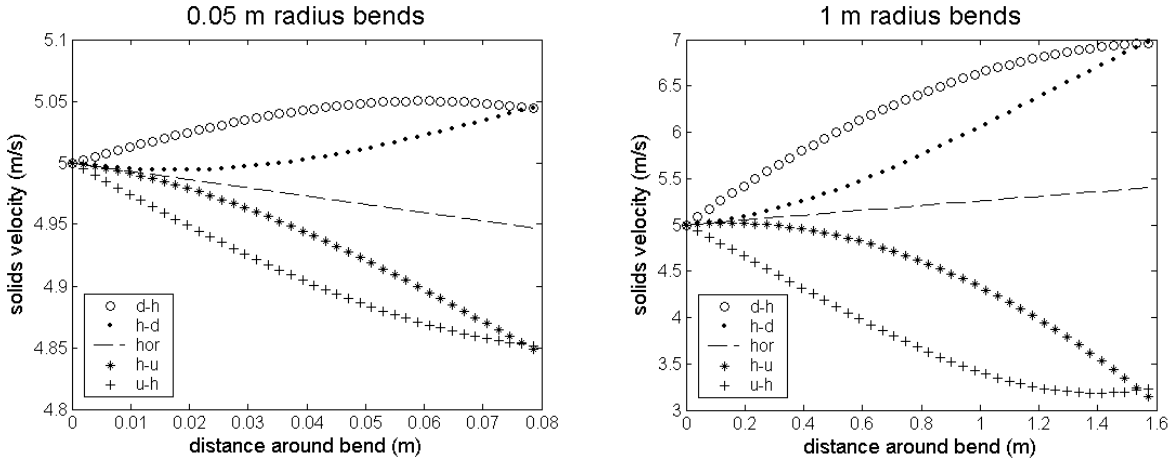


Figure 76, a comparison of the five different bend configuration equations in constant for a small radius bend ($R$ = 0.05 $m$) and a large radius bend ($R$ = 1 $m$). The parameters entered into the model were $k$ (1+B)= 1.7 $kPa$, $\rho_{fb}$ = 1000 $kg/m^3$, $v_{s,i}$ = 5 $m/s$, $m^*$ = 50 and $\lambda_e$ = 0.01

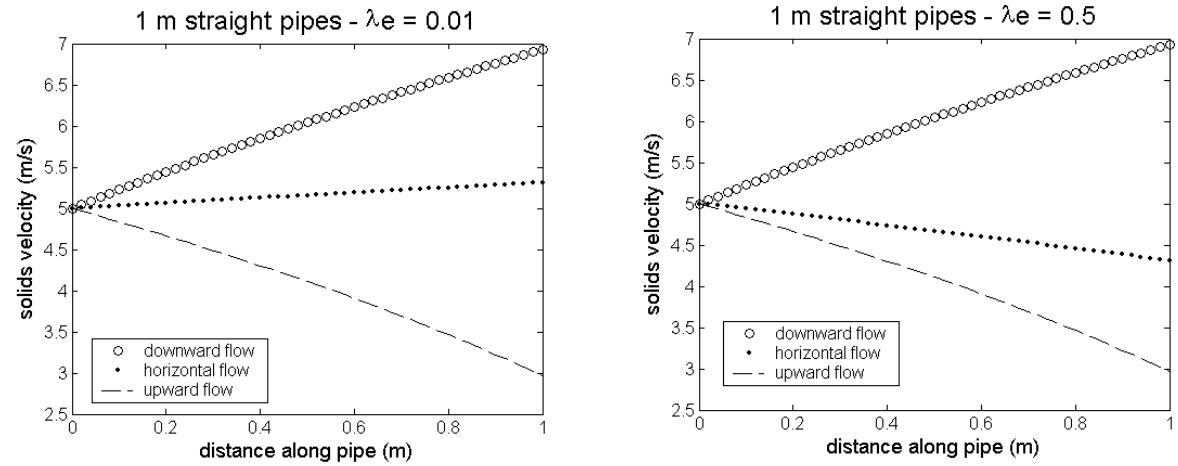


Figure 77, a comparison of three different flow orientations for 1-metre straight sections using two different equivalent friction factors ($\lambda_e$ = 0.01 and $\lambda_e$ = 0.5). The parameters entered into the model were $k$ = 1.7 $kPa$, $\rho_{fb}$ = 1000 $kg/m^3$, $v_{s,i}$ = 5 $m/s$ and $m^*$ = 50

Solutions were then computed for the straight sections for three orientations of flow; upward, horizontal and downward flow. Two different solids friction factor were compared for each of these flows, as is shown in Figure 77.

In comparing the two plots of Figure 77, the only variation is in the horizontal flow where the velocity profile is less for the larger $\lambda_e$. The two vertical flows remain the

same and as expected are independent of $\lambda_e$ as the gravitational forces dominate the flow.

## *6.7 Comparison of Continuum Model to Conveying Tests*

### 6.7.1 Constant solids friction along pipeline

Using the Cement Meal optimal trendline method (Table 20, Chapter 5), the solids friction parameter was calculated as a constant using the average gas velocity within the pipeline for each conveying test. The global conveying parameters ($\Delta P$, $M_a$ and $M_s$) in conjunction with the constant friction parameter were subsequently incorporated into the continuum model. Figure 78 shows four solutions of the model for Cement Meal conveying tests in the 176m short radius pipeline and represent a change in average gas velocity from 11.3 m/s down to 3.4 m/s.

The solution to the 11.3 m/s average gas velocity flow (Figure 78a) showed a solids velocity increase throughout the pipeline, with a reduction in solids velocity around each bend. As the average gas velocity was reduced (as shown in Figures 78b to 78d), the overall solids velocity reduced, and in the case of the average gas velocity test of 3.4 m/s, generally decreased. This reduction in solids velocity behaviour with decreasing gas velocity was mostly due to the bends because of the additional resistive force in the radial direction. With respect to different conveying tests, the larger loss in solids velocity around the bend occurred because the available gas energy was less for the lower average gas velocity tests, which reflects the likely deceleration of the material flow around bends in a real system.

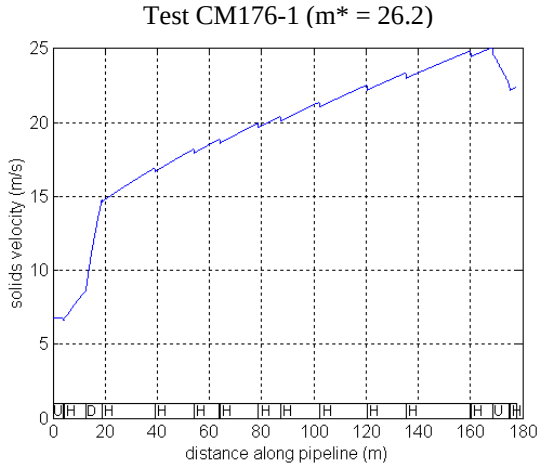


Figure 78a, average superficial gas velocity = 11.3m/s

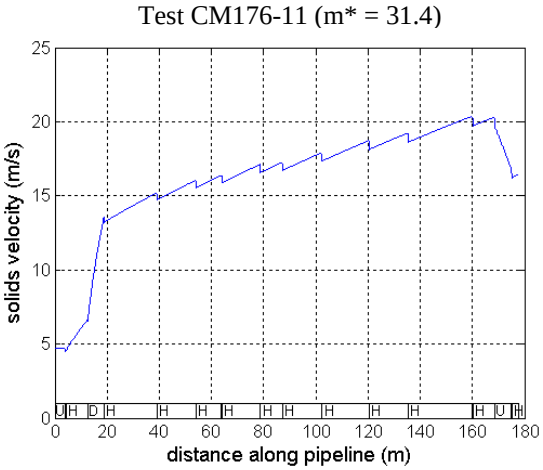


Figure 78b, average superficial gas velocity = 8.2 m/s

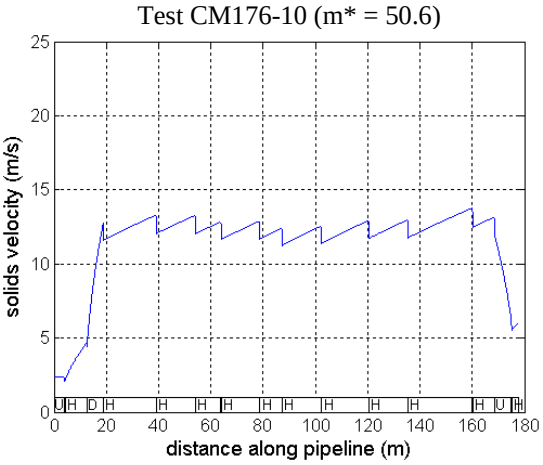


Figure 78c, average superficial gas velocity = 4.1 m/s

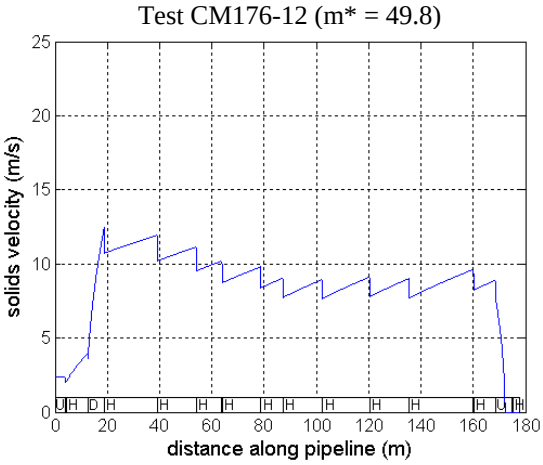


Figure 78d, average superficial gas velocity = 3.4 m/s

Figure 78, solutions of the continuum model for four conveying tests using a constant friction along the pipeline.

#### *6.7.1.1 limitations*

Even though there were some positive aspects of the numerical solids velocity model using constant friction (i.e. solids velocity drop around bends and slower solids velocity for higher *m** values), there were some aspects of the solids velocity result that need addressing. Firstly, it is simple to see that the solids velocities are generally quite higher than the average gas velocity, which cannot physically occur. The major reason for this velocity difference is due in part to the overestimation of the solids velocity in the vertically downward flow section at the start of the pipeline. This overestimation is due

to the assumption of constant bulk density of the solids flow down the pipe and treats the solids as a ‘massed-lump’. In reality, for fine powders the material will convey in a more dispersed form down the pipe at velocities close to the gas velocity. Also, currently the model is based on a force balance and does not account for momentum changes occurring in the flow due to variations in bulk density, fluctuations in bed height and other turbulent flow mechanisms. As a result, the solids velocity model in its present form cannot be used quantitatively.

However, the solids velocity behaviour can be analysed from a qualitative perspective and can be used to show the locations where the solids velocity is low or slows in the pipeline, from which the likely blockage locations can be determined. Also, to better represent the solids flow velocity and therefore provide information on likely pipeline blockage locations, a variable friction parameter was incorporated into the solids velocity model. The variable friction approach, in conjunction with a qualitative solids velocity analysis, is the focus of the next sub-chapter.

### 6.7.2 Variable solids friction along pipeline

The next step in the development of the model was to improve the friction parameter by changing from a constant value to a variable friction parameter. The variable friction component still had the optimal power law relationship detailed in Table 20, however for each incremental step (pipeline segment); a local friction value was calculated. Determining local friction values better represented the change in friction of the particle flow and its relationship with the gas expansion and subsequent superficial gas velocity increase. This variation in friction component is achieved due to the change in superficial gas velocity and subsequent Froude number along the length of the pipeline. Using the same conveying tests shown for the constant friction analysis in Figure 78, the solids velocity/variable friction analysis was conducted with the results shown in Figure 80.

The variable friction solution to 'test CM176-1' (Figure 79a) shows that as the solids flow velocity increases throughout the pipeline there is a negligible change in velocity around each bend. As the average velocity reduces (from 'test CM176-11 (Figure 79b)' to 'test CM176-10' (Figure 79c)), the decrease in velocity due to the effect of the bends is larger. For 'test CM176-12' (Figure 79d), the velocity drops to below zero in the initial horizontal straight section of the pipeline.

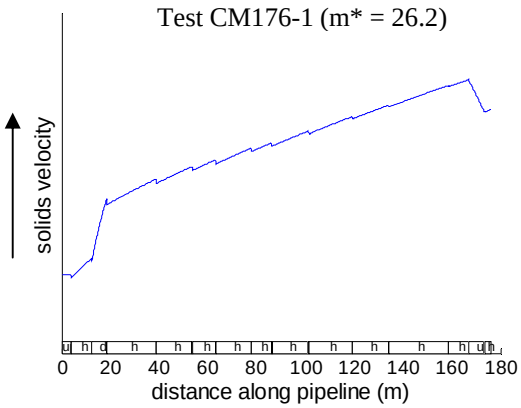


Figure 79a, average superficial gas velocity = 11.3m/s

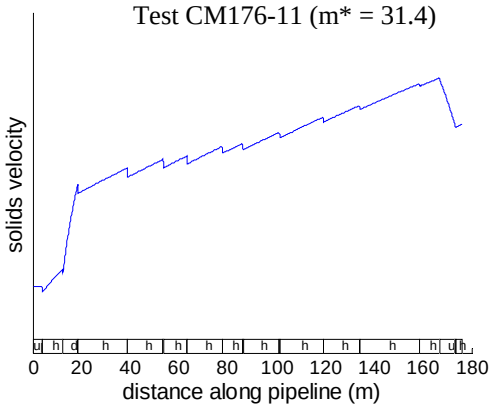


Figure 79b, average superficial gas velocity = 8.2 m/s

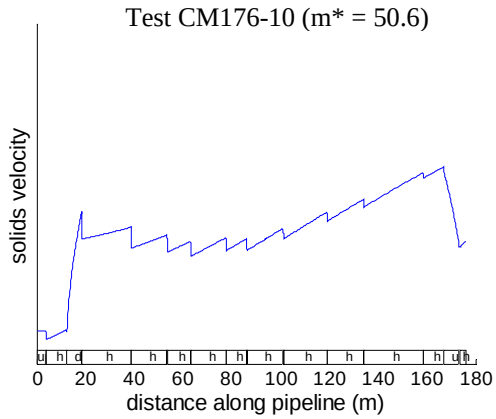


Figure 79c, average superficial gas velocity = 4.1 m/s

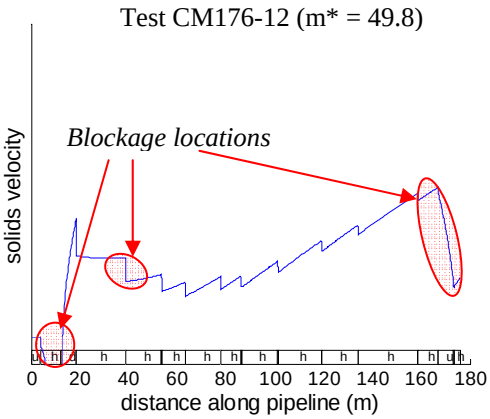


Figure 79d, average superficial gas velocity = 3.4

Figure 79, solutions of the continuum model for four conveying tests using variable friction parameter along the pipeline.

The results for all the variable friction analysis showed that the velocity reduction around each bend was less as the gas expanded through the pipeline, which is significantly different than for the constant friction tests. This smaller velocity reduction reflects the increasingly larger air pressure drop and smaller material contact time associated with each bend as the gas expands. The larger pressure drop means that more energy is available to move the product while the shorter contact time is reflected through a lower friction component due to the higher superficial gas velocity. Also, importantly, the rate of change in velocity (i.e. acceleration) also increased in the straight sections for the variable friction analysis. This increased velocity behaviour better reflects the effect of the gas expansion on the solids velocity. The other important feature of the analysis is that there can be a deceleration in the horizontal sections at the start of the main horizontal section of the pipeline.

#### *6.7.2.1 blockage analysis*

Overall, the solids velocity analysis highlighted three areas of the pipeline where blockage (or operating problems) might occur, as is highlighted in Figure 79d. One likely blockage point appears to occur at the start of the pipeline (zero solids velocity – figure 79d) in the first horizontal section, which is expected as the gas velocity is lowest at the start of the pipeline. Some operating problems occurred in this part of the pipeline as there was some non-steady feeding behaviour from the blow tank into the pipeline. This non-steady feeding was characterised by material stoppage which caused a pressure build up until the flow started again. Another problem point in this particular pipeline is the final ‘upward’ section were velocity drops significantly. Lastly, there appears to be another problem area in the horizontal straight section after the vertical drop in the pipeline, as indicated by the ‘blockage location’ in Figure 79d. In this horizontal section, the deceleration of the solids flow indicates that the friction force of the material flow cannot be overcome by the motive pressure force from the gas. Importantly, it was in the bend after this straight section that the blockage occurred for the cement meal. The blockage at this bend was confirmed by visual inspection of the pipe blockage access points and removal of the join between the bend and the straight pipe section.

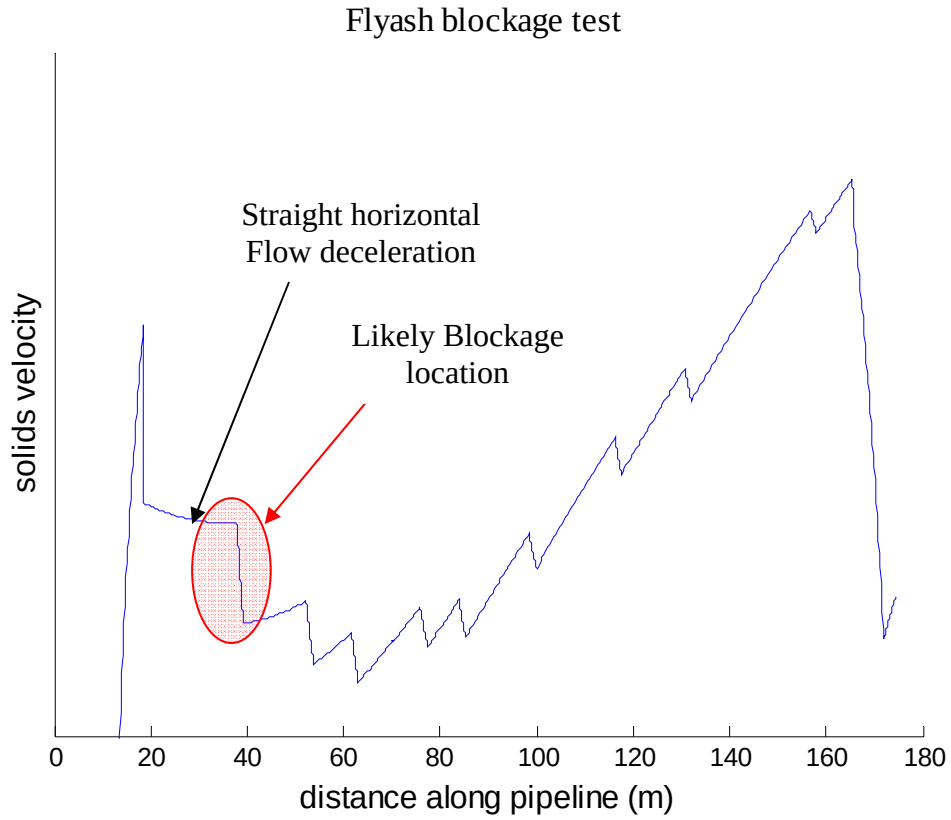


Figure 80, continuum model solids flow velocity analysis for Flyash near blockage conditions

To test if the blockage location can be predicted for a similar dense phase capable material, the Flyash pneumatic conveying tests conducted in the 173m variable radius pipeline included placing pressure transducers at the likely blockage point in the horizontal section of the pipeline. The likely blockage location was determined from the analysis of the blockage solids flow behaviour for test FA173-19 (317 kPa total pressure, primary airflow of 0.0100 kg/s, secondary airflow of 0.0079kg/s). The analysis indicated that the three main problem areas in the pipeline that occurred for the Cement Meal also occur for the Flyash. As such, the likely blockage location was assumed to be in the same location as for the cement meal, as indicated by the deceleration of the solids flow analysis shown in Figure 80. Subsequently, pressure transducers were placed along the pipeline (T1 to T15 – see Figure 39) and the air reduced until blockage occurred (primary airflow of 0.0100 kg/s, secondary airflow of

0.0062kg/s), with the results of the pressure profiles at the most accurate pressure transducer locations shown in Figure 81.

The structure of the pressure traces in Figure 81 shows an initial pressure surge past the T1 to T4 pressure transducers as the material flow commenced (i.e. when the blow tank pinch valve was opened). During this surge, a lower fluctuating pressure profile was seen further down the pipeline at transducer locations after T6. Subsequently, the pressure started to rise quickly in T1 prior to the bend and to a lesser extent T2 to T4 after the bend while further down the pipe at the T6 to T12 locations, the pressure fluctuations stopped and reduced to ambient pressure. At this time, the material had stopped flowing from the receival vessel and the pressure continued to rise, so the conveying airflow was turned off. The most obvious pressure behaviour after the airflow was turned off was that there was residual pressure at the T1 and T2 locations while the pressure transducer locations T3 and T4 showed a pressure decay down to ambient pressure. This difference in pressure behaviour shows that at T1 and T2, the material is not allowing air to permeate through and that a blockage has occurred here. At the T3 and T4 locations, there probably is material completely filling the pipe; however the material must have a much higher porosity at these locations allowing the air to permeate through or de-aerate, as indicated by the pressure decay taking approximately 30 seconds. At the other pressure locations (T6 – T12), there was some material on the bottom of the pipe, however the top of the pipe was clear. Subsequent visual inspection confirmed that the pipeline was blocked at this bend.

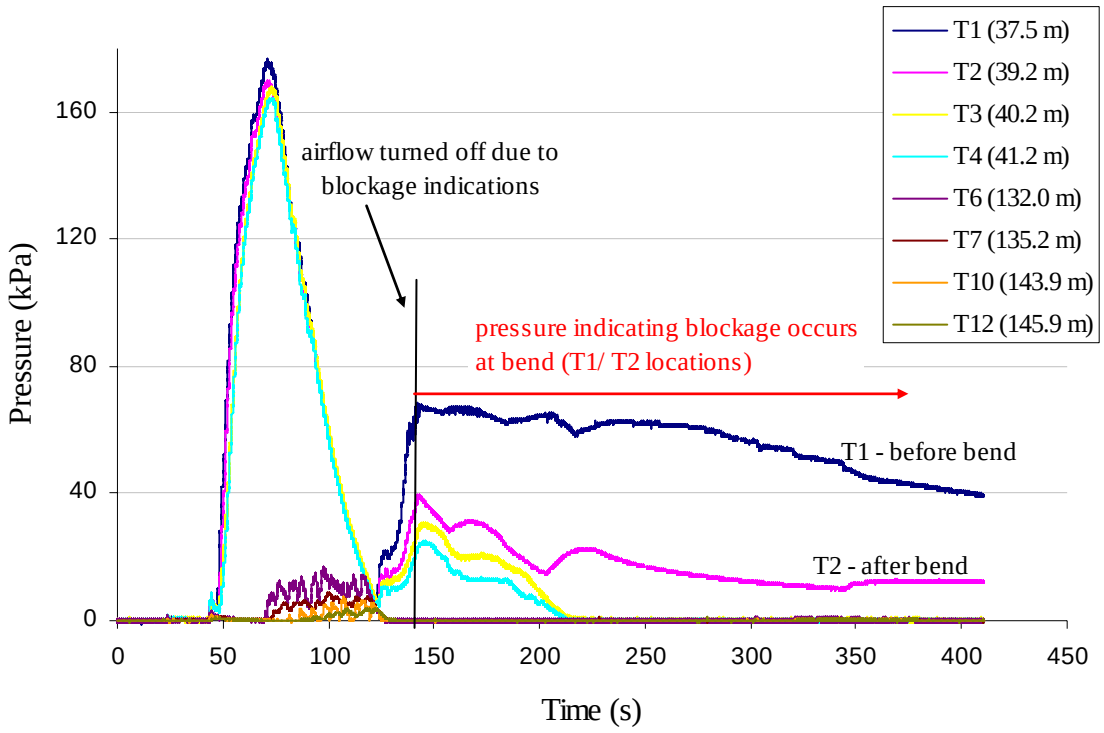


Figure 81, pressure trace of blockage location for Flyash at an airflow rate of 0.0162 kg/s (primary air = 0.0100 kg/s; secondary air = 0.0062 kg/s)

The blockage location was also determined for the Alumina in the 173m variable radius pipeline. Using the same process as for the Flyash, the airflow was decreased to near the blockage point and the conveying parameters were incorporated into the solids velocity model (an example for test AL173-11 is shown in Figure 82). As the Alumina dense phase flow has a higher minimum conveying gas velocity (3.9 m/s) in comparison to the Cement Meal (1.99 m/s) and Flyash (1.63 m/s), the structure of the predicted solids flow velocity is significantly different near the blockage location. For the Alumina, the is no deceleration of the solids flow along the horizontal sections of pipe, so the most likely blockage location was at or near the feed section at the start of the pipeline or in the vertical upward section at the end of the pipeline. So, the equipment used for the capturing of the upstream (or global data) conveying conditions were analysed for the actual pipe blockage test with the results shown in Figure 83.

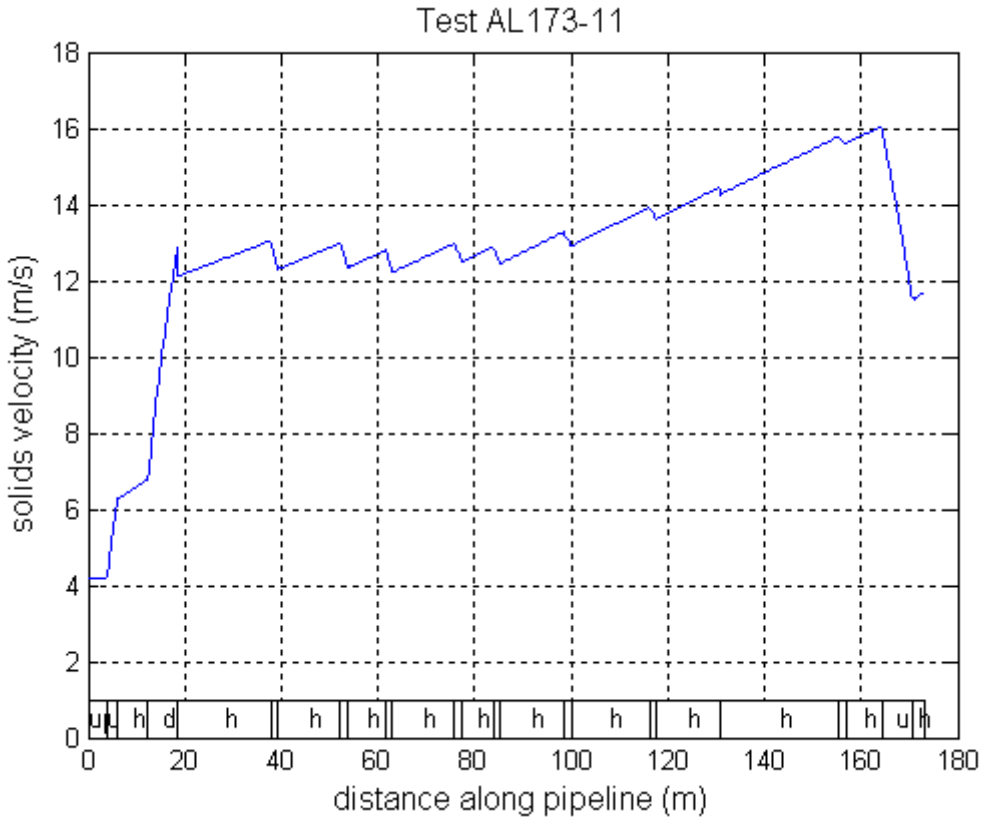


Figure 82, continuum model solids flow velocity analysis for Alumina near blockage conditions

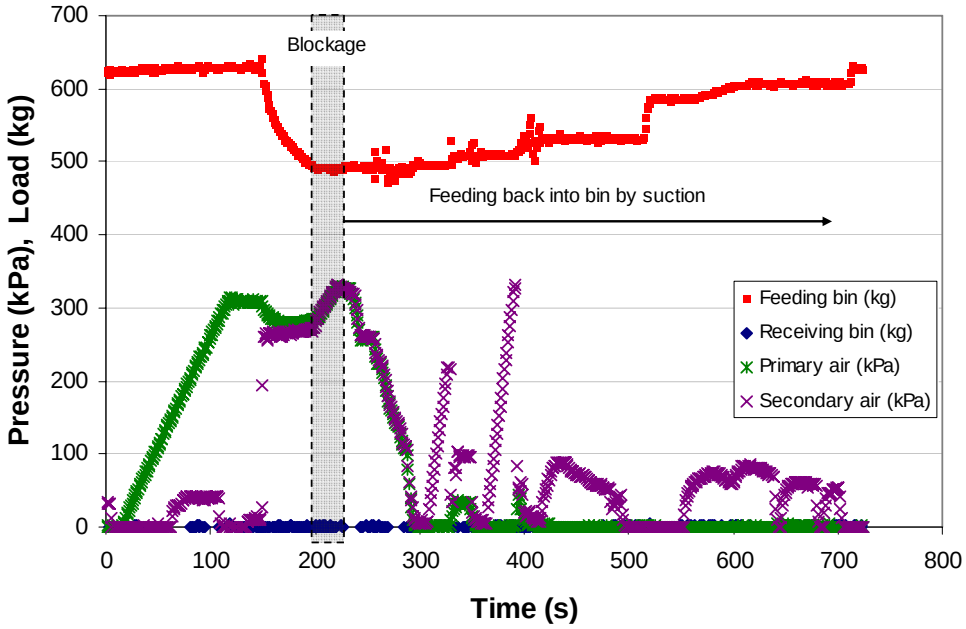


Figure 83, conveying test data for the blockage of Alumina with an airflow of 0.0424 kg/s (primary air = 0.0100 kg/s; secondary air = 0.0324 kg/s)

The results of the blockage tests showed that approximately 140kg of material was fed into the pipeline until feeding ceased and pressure started to rise in the blow tank, indicating that a blockage had occurred. Even though a large amount of material was fed into the pipeline, no material was collected in the receival bin. Subsequent investigation showed that the sight glasses at approximately 150m and 130m locations were filled with material, however the sight glass at the beginning of the pipeline (approximately 10m from the start of the pipeline) was only partially filled. Inspection of the vertical upward flow section of the pipeline confirmed the blockage at this location. For interest, the conveying data displayed in Figure 83 also shows the technique used to unblock the pipeline which was achieved by pressurising the pipeline between the back of the blockage and the pinch valve to the blow tank. Once pressurised, the pinch valve was opened, which created a vacuum and subsequently 'sucked' the material back into the blow tank. This process was repeated until the pipeline was unblocked.

Generally, the analysis of the solids velocity behaviour indicated that the problem areas in the pipeline and subsequent blockage location were the same for the Cement Meal and the Flyash. This similarity in solids velocity behaviour indicates that for material that can be conveyed in the lower range of fluidised dense phase flow, the resistive behaviour is similar at low flow velocities. However, the minimum dense phase flow capability of the Alumina is higher and as such, the blockage location was different.

### 6.7.3 Measuring fluidised dense phase flow velocity

The purpose of this sub-chapter is to show the methods used to try to measure the solids flow velocity in the pipeline and to present the information gained from the subsequent analysis. The initial intention of measuring the solids velocity was to quantitatively compare it with the solids velocity model. However, as will be shown and discussed in this sub-chapter, the solids velocity is non-steady and pulsatile to such an extent that determining a steady state value that reflects the speed of the flow is not possible.

Firstly, to try to measure the solids flow velocity at a point in the pipeline, a high speed video (1000 frames per second) was used to capture the flow structure utilising on of the sight glasses within the pipeline (Figure 40). For the fluidised dense phase flow, the particles were too small to be tracked individually, so the technique used in the video analysis calculated the dense phase flow velocity by tracking the small void spaces within the flow. The displacement ($S$) travelled, by a particular void space, after each subsequent time step ($t$) (or frame) was used to determine the solids flow velocity, as shown in Figure 84. Four tests were initially analysed from the 130 m pipeline for Cement Meal (Tests CM130-5, 9, 13 and 15) which varied in airflow rates between 0.036 to 0.056 kg/s, $m^*$ values between 61 and 71 and pressure drop between 294 and 355 kPa.

The results of the high speed video analysis showed that the flow conveyed in pulses with a subsequent decay in velocity (as shown in Figure 85) with the following flow features observed:

1. At the start of the pulse, the flow appeared to be full bore.
2. After the pulse, the material slowed with a faster dilute phase structure forming in the upper layer and a slower fluidised dense phase flow structure forming in the lower layer, which suggested that a shear layer between the two flows occurs.
3. As the velocity reduced, the bed height of the dense phase layer reduced, which suggested that the local bulk density of the dense flow increased.

4. For the pulses of the four tests analysed, the velocity decay was similar (see Figure 85), which suggested that the pulsatile decay for fully established fluidised dense phase flow of the Cement Meal may be independent of conveying conditions. However, the test sample size is very small and the actual flow relationship to changes in operating conditions will need significantly more data to become clearer.

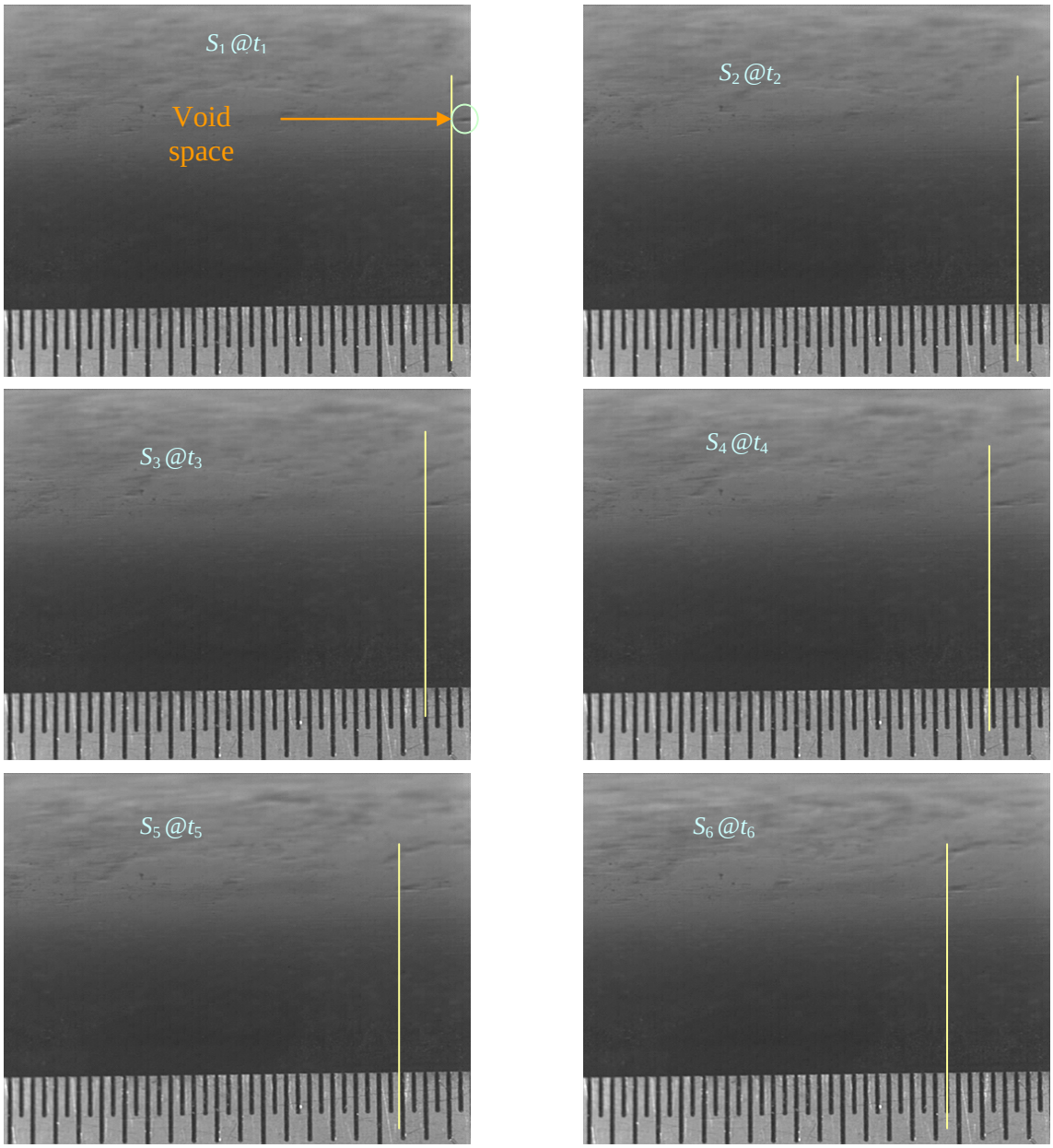


Figure 84, high speed video images of the fluidised dense phase flow and void spaces.

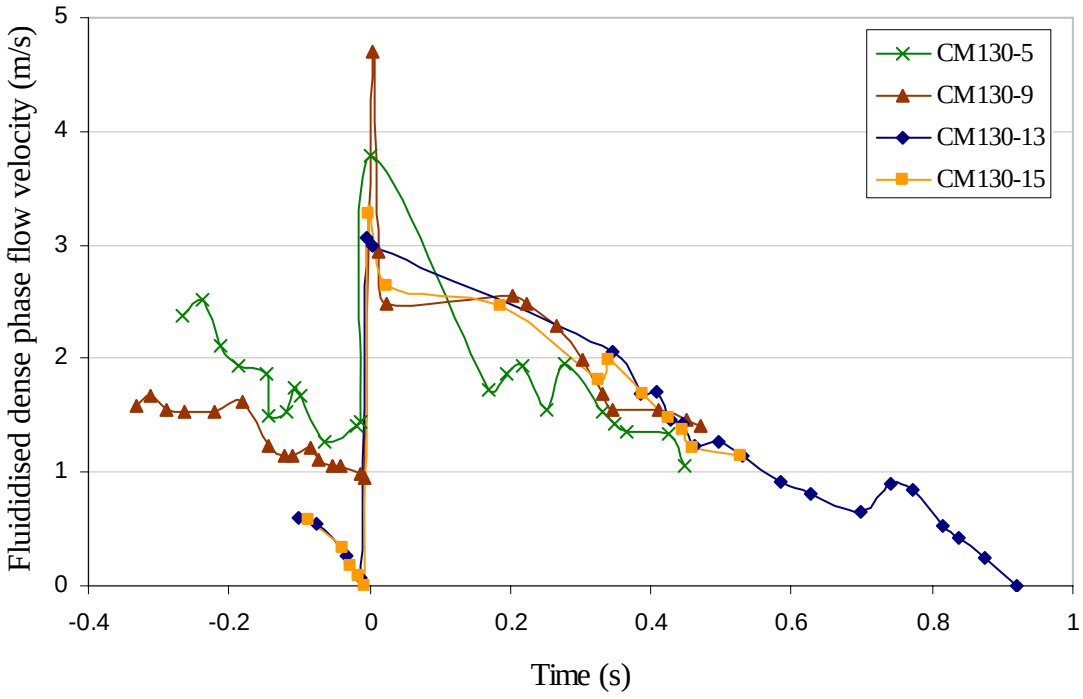


Figure 85, fluidised dense phase solids flow transient behaviour

In conjunction with the video analysis, a pressure transducer technique was conducted to try to determine the gas pulse velocity to firstly, find a non-visual means of estimating the dense phase flow velocity, and secondly, to compare the two velocity techniques. The pressure transducers used were Barksdale 0-100 psi pressure transducer located at the T8 – T15 pressure tapping points (130m pipeline) and the pressure data was recorded at a minimum frequency of 50Hz with the results of one test shown in Figure 86. Due to material build-up in some of the pressure tapping points, the most accurate pressure traces were obtained from T12 to T14 transducers (approximately 86 m from the start of the pipeline).

In investigating the structure of the pulsatile pressure fluctuations within the steady state period, a closer examination of the test data was undertaken for each of the conveying tests; an example for test CM130-12 with pressure transducer locations T12 and T14 is shown in Figure 87. The pressure structure investigation showed that for each test and each pressure transducer location, Ti, there was indication of a possible fluctuation period ($T_{P\,(Ti)}$). Also observed was a lower and upper bound of the pressure fluctuations, from which a major amplitude value ($A_{P\,(Ti)}$) is seen. It was also apparent that the there

was a time delay ($\Delta t_{P\ (Ti\text{-}Tj)}$) of the pressure pulse minima and maxima between each subsequent pressure transducer location, as is shown in Figure 87 for $\Delta t_{P\ (T12\text{-}T14)}$.

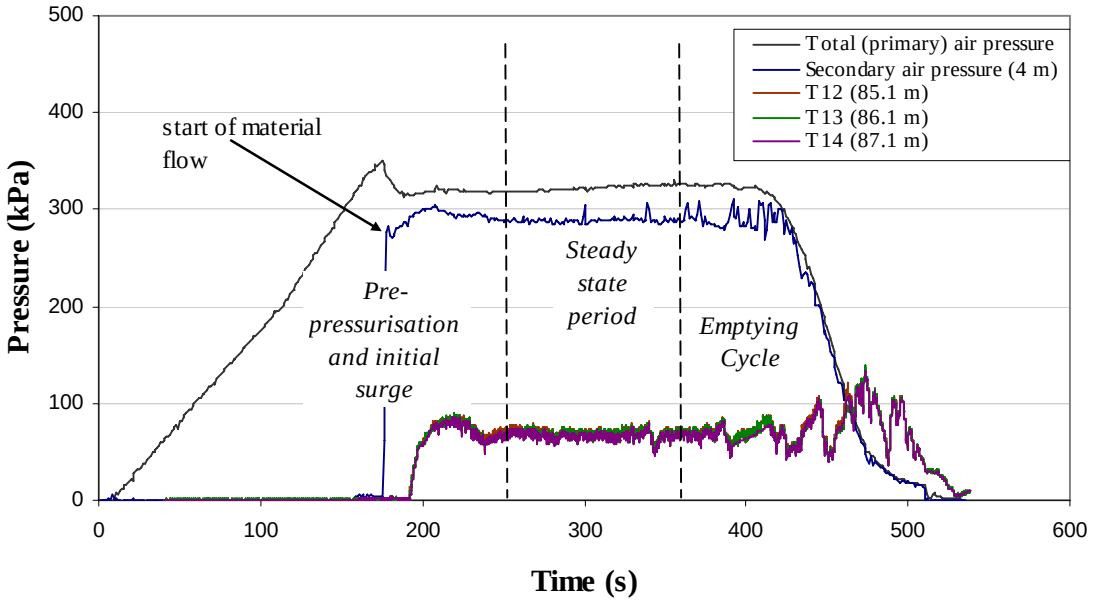


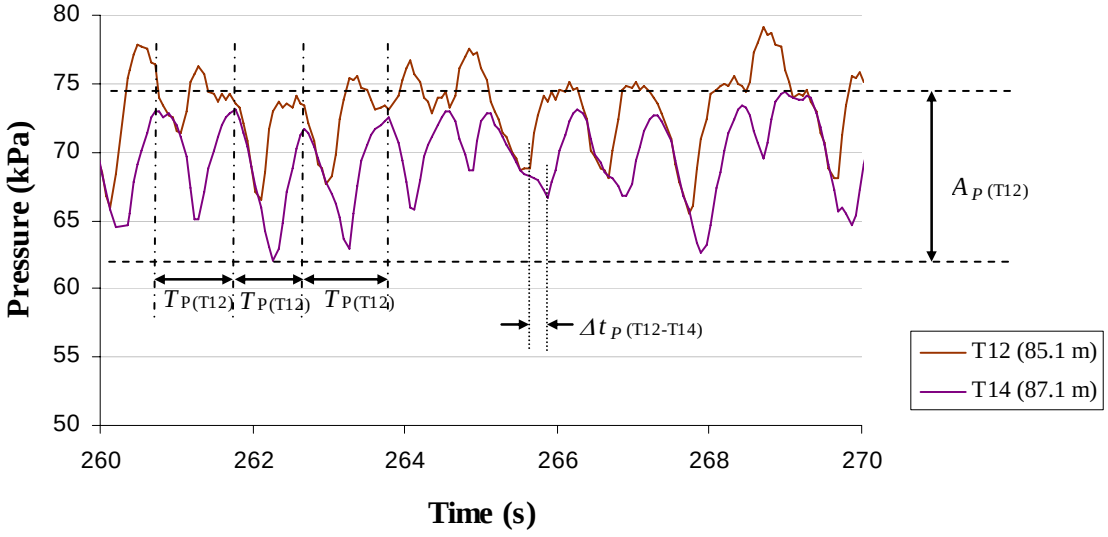


Figure 86, the pulsatile pressure test results for CM130-12

Figure 87, detailed view of the structure and analysis technique of the pulsatile pressure results for test CM130-12 in the steady state period

From the analysis of the time delay, the velocity of the pressure pulse (or wave) was determined and compared with the calculated superficial gas velocity, as shown in Figure 88. Even though the gas pressure pulse analysis shows a large amount of error, the average of the pulse velocity fluctuations is similar to the superficial gas velocity, which is understandable as the amount of energy in the system is generally conserved. However, as the gas pulse velocity fluctuates significantly, then determining the solids flow velocity relationship to the solids velocity model is also not possible.

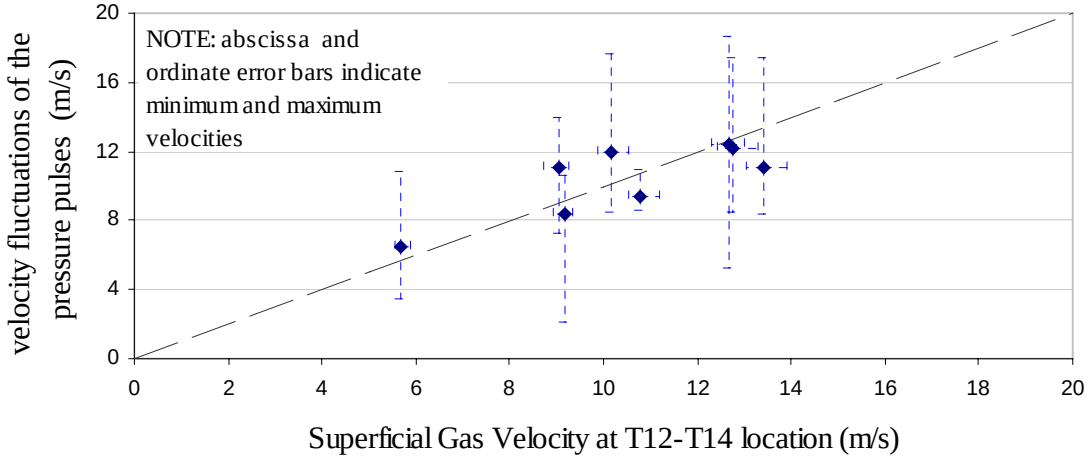


Figure 88, comparison of T12 to T14 velocity behaviour of the pressure pulses and the superficial gas velocity

In Summary, during each individual pulsatile event (or transient), a material impulse occurs which is characterised by a sudden increase in material velocity and bed height, which subsequently decays to a lower material velocity and bed height. Observation of the material impulse also indicates that the conveying gas re-aerates the material and is associated with fluctuations in gas pressure. What was clear from this analysis is that the dense phase flow velocity and dense phase bed height behaviour is transient and quite complex. This complex flow behaviour makes it difficult to correlate the solids flow velocity to the steady state continuum model and may also be the major reason why the accuracy of the current steady state pressure drop analysis methods cannot be improved significantly.

# CHAPTER 7: CONCLUSIONS

This thesis represents research on specific design aspects (mode of flow capability, pressure drop prediction and solids flow velocity behaviour) for determining dense phase pneumatic conveying capabilities and performance for fine powders. These design aspects represent and form part of a proposed fluidised dense phase design philosophy (or guide) and a flowchart representing this guide is displayed in Figure 89. The salient outcomes and associated phenomena of the design guide are symbolised by the darker flow chart blocks. The design aspects investigated are summarised below.

## *7.1 Mode of Flow*

Firstly, in Chapter 2, diagrams and parameters which have been used and/or developed for the prediction of mode of flow capability in pneumatic conveying systems were reviewed. The three major modes of flow were classified as dilute phase only flow, a full bore flow called plug flow; and a partially filled pipe flow classified as fluidised dense phase flow.

The diagrams which utilised basic particle parameters of particle density and mean size had strong predictive areas for plug flow and fluidised dense phase flow. However, there were distinct regions in these basic particle diagrams where the mode of flow capability could not be determined. To attempt to improve the predictive capability of these basic parameter diagrams, the particle density component was replaced with a ‘loose poured’ bulk density parameter. It appeared that there was a slight improvement in predictive performance using ‘loose poured’ bulk density as a distinct area showing dilute phase only capable material was observed. Unfortunately, there still were distinct areas in these diagrams where no mode of flow prediction was observed.

Air-particle parameters based diagrams were reviewed and it was found that they generally predicted more accurately the mode of flow capability of a bulk material. The major problem associated with these diagrams and associated parameters were that the de-aeration factors were not easily comparable between different researchers. This lack of commonality in de-aeration values led to the development of a new mode of flow chart,

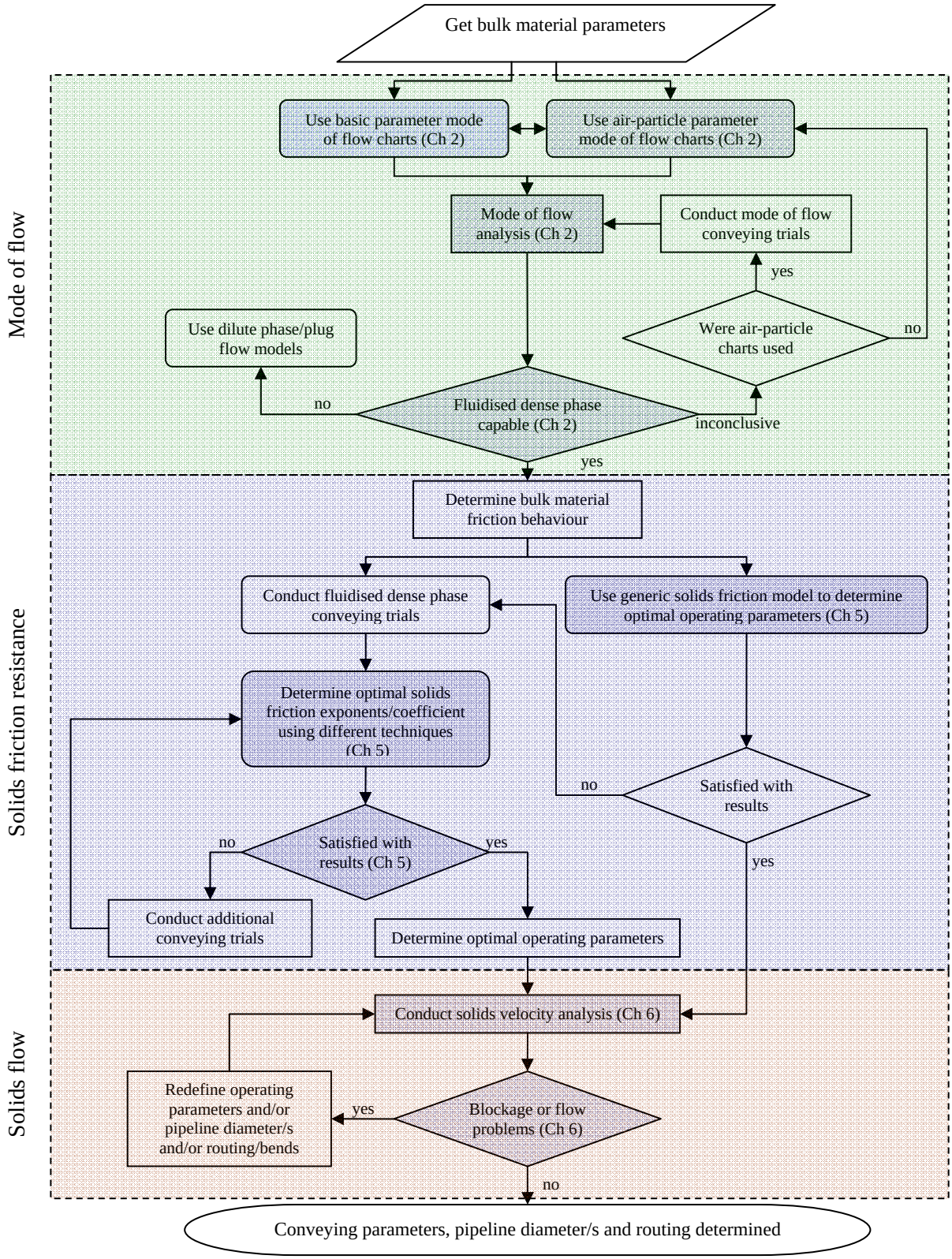


Figure 89, proposed flow chart of fluidised dense phase conveying. The coloured blocks represent design aspects detailed in this thesis

which utilised the more comparable parameters of permeability and 'loosed poured' bulk density. It was found that the mode of flow predictive capability of this new chart was comparable with the other air-particle based diagrams and parameters.

It is interesting to note that the performance of all the diagrams could satisfactorily predict at least one mode of flow. As such, rather than relying solely on one chart to be the definitive solution for a bulk materials potential conveying capability, a more discerning analysis of the particle and bulk parameters should be used which utilises a number (if not all) of the diagrams presented. The only other general comment on the mode of flow analysis is that as a material moves closer to a specific mode of flow boundary, then the confidence of the ability of the material to convey in a particular mode of flow becomes less. Therefore, it is bulk materials which sit close to this boundary which will require more pneumatic conveying analysis to either still try to predict the bulk materials mode of flow capability, or to actually convey the product to determine this capability.

## *7.2 Solids Friction Resistance*

The parameter which defined the fluidised dense phase solids friction was determined from an empirical approach using a steady state analysis. The major parameters of the solids friction were the solids loading ratio and Froude number parameter. As previous researchers have found, the friction correlation is relatively good for a given material and pipeline configuration and generally has some power law structure. The accuracy of this power law structure with subsequent scaling up results for pressure prediction can vary significantly and at times the pressure solution can become unstable or no solution found. The reasons for this instability can be traced back to the exponents/constant used in the power law.

A power law was based solely on the solids loading ratio and the Froude number was developed and an analysis of the scale up behaviour and variation of the exponents and coefficient found specific relationship to each other and limits to their values that can be realistically used. The analysis showed that the change in Froude number exponent is proportional to the change in solids loading ratio exponent, while the constant for solids friction has an exponential relationship to the exponents. The pressure solution was

always found to be stable when the Froude number exponent was less than two, which is a mathematical limitation of the model. The solids loading ratio exponent has limits between 0 and 1 to realistically have a true physical meaning.

As shown in Chapter 4 and Chapter 5, the pressure results are significantly dependant on the constants and exponents derived for the solids friction correlations, with these constant and exponent values subsequently derived from the pneumatic conveying tests. Therefore the conveying tests must encompass a sufficient range of gas velocities and solids loading so that the exponents and constants used in any solids friction power law correlation better represent the actual solids frictional behaviour in the pipeline. Subsequently, a comparison of three methods of determining the optimal values of the solids friction exponents/constants were conducted with the comparison showing their variation. This comparison clearly showed which material had the greatest variance in exponent/constant values using these different techniques, with a larger variation indicating a lower confidence in the resultant solids friction correlation.

Lastly, a generic friction model was empirically derived for fluidised dense phase conveying which incorporated air-particle and basic parameters of the conveyed material. The model was fairly accurate (within +10% and -25 %) for all the materials analysed except the Pulverised Fuel Ash (PFA). The PFA pressure drop results were in error by a factor of 2 for all the conveying tests, with this error traced back to the sensitivity of the constant used in the correlation. However, it is important to note that the variation in optimal exponent for the PFA was significantly large (Table 20), which may have attributed to the error.

It is important to note that the analysis used in determining the pressure drop in this thesis is based on average pressure (or density) and as such, the total length, number and location of bends and horizontal and vertical sections of the pipeline may influence the weighting of these solids friction factor exponents and constant/s. Finally, as a general note, the empiricism which has dominated the solids friction correlations may not be able to provide an accurate generic friction model and therefore eliminate the need for conveying trials This empiricism limitation in fluidised dense phase pneumatic conveying may also be due to the current steady state analysis methods used which may

not accurately reflect the frictional resistance of the transient-pulsatile (non-steady) flow behaviour of fluidised dense phase pneumatic conveying

## *7.3 Solids Velocity*

A continuum model which utilised force equilibrium, conservation of mass and continuity equations was developed to calculate the solids flow velocity profile along a pneumatic conveying pipeline. The continuum model was specifically developed for fluidised dense phase conveying and although validation of the actual velocity was not possible, the deceleration behaviour along the horizontal sections indicated a likely blockage location. Incorporation from a constant friction to a variable friction component along the pipeline equated to a more realistic frictional response of the system, where changes in air density throughout the pipeline gave a greater representation of the expansion of the gas flow.

From the variable friction analysis, the solution to the force balance was represented by plotting the solids velocity behaviour along the pipeline, which was qualitatively analysed. From this analysis, a deceleration region was observed which correlated to the blockage location in slow moving (minimum superficial gas velocity = 1.98 m/s for Cement Meal and 1.68 m/s for Flyash) fluidised dense phase conveying. For the faster flowing Alumina powder (minimum superficial gas velocity = 3.98 m/s), the low solids velocity areas correlated to the blockage location and areas in the pipelines where solids flow problems occur.

Although the solids velocity model in its present form cannot be effectively used quantitatively, further improvements to the model using any form of correction factor have been resisted, as this lessens the fundamental physics associated with the approach. To maintain the integrity of the fundamental physics, certain assumptions need to be addressed from a transient point of view, which is detailed in Chapter 8 (future work). This transient approach will build on the work presented in this thesis.

# CHAPTER 8: FUTURE WORK

Currently, the fluidised dense phase flow has been analysed utilising steady state models. However, from flow visualisation and pressure pulse analysis, it is clear that the flow of dunes in low velocity fluidised dense phase conveying is pulsatile in pressure behaviour and has a transient characteristic in the solids flow. So the question remains as to whether to continue to approach the prediction of conveying behaviour from a steady state point of view or attempt to characterise the flow utilising methods which can describe a transient behaviour. This researcher feels that certainly, in the near future, more accurate design methods may be achieved by improving the current steady state approaches. However, in the longer term, more fundamental research on the micro-scale mechanisms are required to understand the non-steady behaviour, which will hopefully, in time, provide even more accurate design methods.

## *8.1 Steady state approach*

Generally, the steady state approach concentrates on determining the operating parameters of conveying gas and solids mass flow rates and the total pipeline pressure drop required. To improve the pressure drop technique described in this thesis, then the modelling of two important areas require more development:

1. Back - calculating the solids friction and subsequent pressure profile via an algorithm which uses small step lengths (slices the pipeline into smaller sections) which will better represent the compressibility and gas expansion along the pipeline. A flowchart defining this segment method is shown in Figure 90 for a single pneumatic conveying experiment.

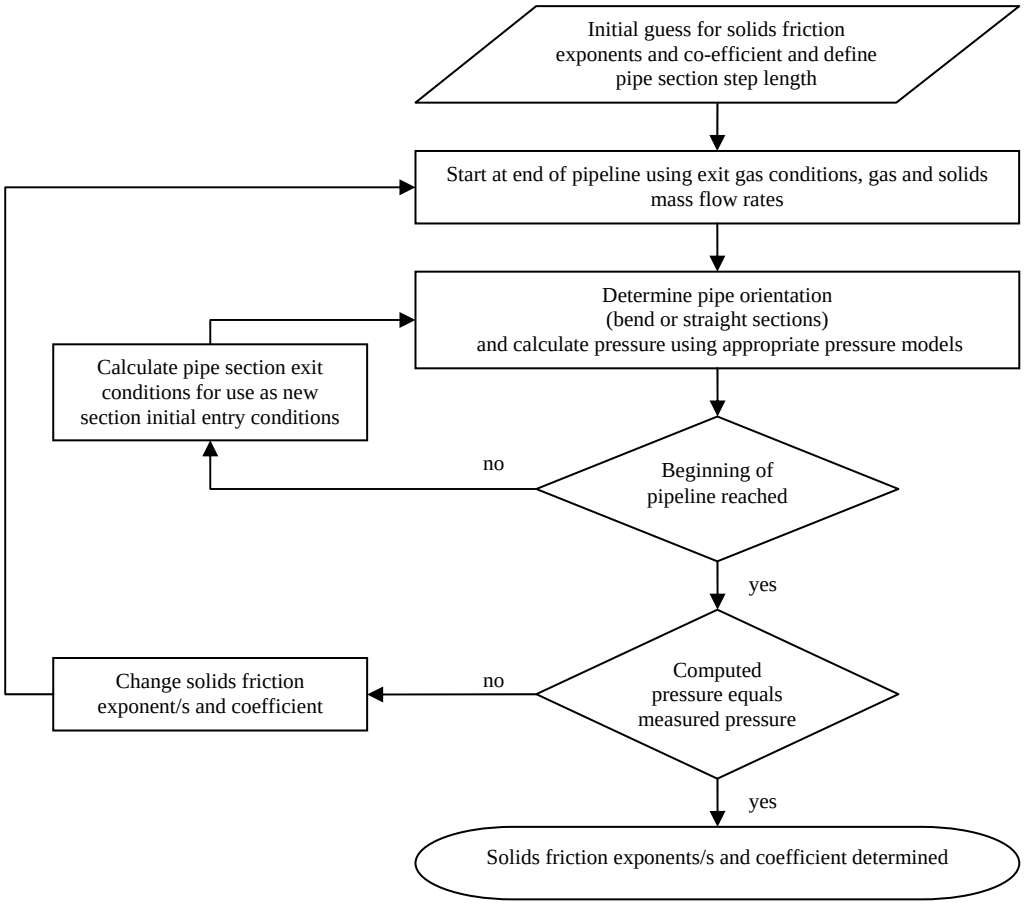


Figure 90, a flowchart showing the proposed back-calculation of a solids friction parameter using a segmented local approach.

2. Incorporating pressure drop models which more accurately reflect the local pressure bend losses at each point (eg, Bradley [4], Datta *et al* [7]) and also define the variation in pressure lengths associated with deceleration into and acceleration out of the bends including the variation of these lengths due to bend position within the pipeline and changes in operating parameters.

In using a local approach for determining the constants/exponents for the solids friction correlation will firstly, investigate if one set of constant/exponent values can sufficiently describe the variation in solids friction for a single conveying test. Furthermore, comparison of the constant/exponent friction results for each conveying test will help establish the accuracy of the correlation for different conveying conditions.

## *8.2 Transient approach*

Complex interactions occur during the formation of the material pulses due to the flow of air through the material; the flow of air above the material and the frictional interactions between the material bed and the pipe wall. For fluidised dense phase conveying, the powdered materials which exhibit high levels of air retention capability have a tendency to de-aerate once a full bore plug of material is formed leading to low air permeability and subsequent blockage. Clearly, the key to this lies in the aeration and fluidisation capabilities of the solids to be conveyed. The state of aeration of the solids will dictate the bulk density of the material which will clearly vary with time. It is the investigation and analysis of the time variation in flow structure that will lead to a better understanding of the unsteady flow. This will potentially lead to better modelling of fluidised dense phase conveying and ultimately a significant increase in the accuracy of prediction of the conveying parameters.

For example, in order to study the flow under dense phase flow conditions, it is useful to first examine the stress conditions and drag effects due to the resistance of bulk solid when conveyed in a horizontal pipe under varying fill ratios. The problem here is analogous to chute flow as studied by Roberts and Scott [43]. The model for this conveying condition is depicted in Figure 91. It is assumed that the loading is symmetrical and that the major consolidation stress $\sigma_1$ is equal to the 'hydrostatic' vertical stress. This latter assumption is consistent with the shallow bed conditions existing in the pipe.

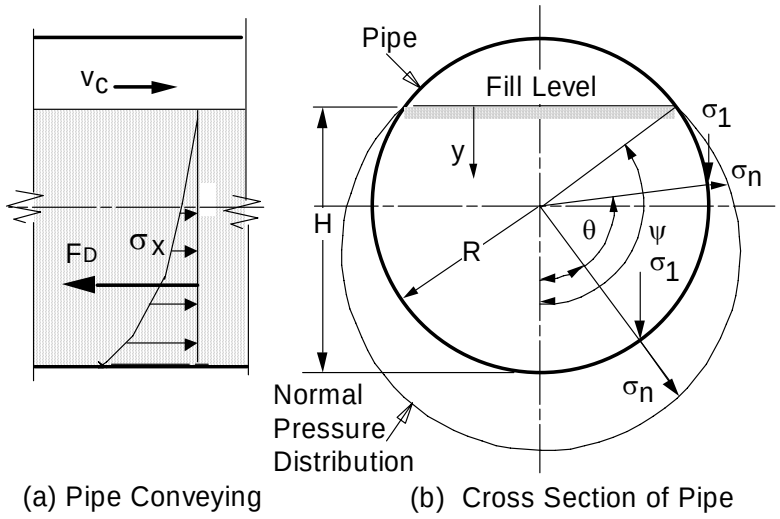


Figure 91, horizontal pipe flow model – partly filled condition

Based on this assumption, further analysis allows the normal stress distribution to be determined for a partially filled pipeline; however initial modelling using a coulomb friction approach required an input wall friction angle between 89-90 degrees for an accurate pressure drop to be computed. This high wall friction angle realistically means that viscous like resistance is dominant in the flow. Also, the bulk density and the frictional coefficient or viscous behaviour will not be constant but will vary with the flow conditions in the pipeline. Furthermore, the degree of filling of the pipe will vary both at any given point in the pipeline with time and at any point along the pipeline length at a given point in time. Hence any meaningful analysis or modelling must be informed by an understanding of the transient behaviour of the flow. In understanding the response of a particulate material in a system, the following points and behaviour need to be considered:

1. The fluidised dunes can be considered as a continuum where, in horizontal flow, the dune is supported by the bottom of the pipe and where the frictional interactions between the dune and the pipe wall induce a retarding force on the flow of material, which is probably a viscous like resistance.

2. The top surface of the dune appears to oscillate between a shear flow due to the relatively high velocity flow of gas in the top section of the pipeline and

a sudden pulse of full bore highly aerated material flow. The interface between the high velocity gas and the dune is particularly complex with the exchange of air flow to and between the dunes interstitial gas flow aerating and de-aerating the mixture

3. The process by which the material aerates and de-aerates is a function of the bulk parameters of permeability, fluidisation velocity and de-aeration rates. The amount of aeration will also affect the value of the bulk density for a given material and flow condition and the viscous resistance.

If the aeration/de-aeration behaviour of these pulses can be established and related to the pressure fluctuations, the modelling of the fluidised dense phase systems may be improved. For instance, even though the solids velocity model defined in Chapter 6 is steady state, the force balance equations are a partial differentiation of the fundamental momentum and impulse balance equations and as such the time dependant response of the flow can be modelled. For instance, integration of the change in force balance for the tangential force component of the solids velocity model (Equation 7.1) from time $T_1$ to $T_2$ is defined as:

$$\int_{T_1}^{T_2} \Sigma F_t dt = m v_{s_2} - m v_{s_1} \tag{7.1}$$

where the left hand side of the equation represents the linear impulse and the right hand side represent the linear momentum change of the elemental slice of fluidised dense phase flow. Subsequently, this momentum-impulse model has the potential to form the basis of a constitutive transient solids velocity model where the parametric models which describe the changes in bed height, bulk density and/or friction can be incorporated and modified, as required.

Finally, the approach to improve the predictive tools for dense phase pneumatic conveying of fine powders must include both the laws that govern the motive force behaviour of the gas and reflect the reactive behaviour of the solids flow. Also, the length scale used must be appropriate given the current computational ability available, which realistically means that a continuum based approach provides the only reasonable design tool for modelling the behaviour of the dense phase solids flow of powders.

# CHAPTER 9: REFERENCES

[1] Abdullah, E.C. and Geldart, D. (1999) The Use of Bulk Density Measurements as Flowability Indicators. *Powder Technology*, 102, 151-165

[2] Australian Bureau of Agriculture and Resource Economics (2007), *Australian Mineral Statistics*, December Quarter 2006, Canberra, 14 March. www.abareconomics.com

[3] Australian Department of Foreign Affairs and Trade (2006), *Australia - Fact Sheet*, September 2005-2006. www.dfat.gov.au

[4] Bradley, M.S.A. (1990) Prediction of Pressure Losses in Pneumatic Conveying Systems, *PhD Thesis*, Thames Polytechnic, London, UK

[5] Chambers, A.J. and Marcus, R.D. (1986) Pneumatic Conveying Calculations. *2nd International Conference on Bulk Materials Storage, Handling and Transportation*, Wollongong, Australia, 49-52

[6] Chambers, A.J., Keys, S. and Pan, R. (1998) The Influence of Material Properties on Conveying Characteristics. *6th International Conference on Bulk Materials Storage, Handling and Transportation*, Wollongong, Australia, 309-319

[7] Datta, K.B. and Ratnayaka, C. (2003). A simple Technique for Scaling Up Pneumatic Conveying Systems. *Particulate Science and Technology*, 21, 227-236

[8] Dixon, G (1979) The Impact of Powder Properties on Dense Phase Flow. *Proceeding for the International Conference On Pneumatic Conveying*, London, UK

[9] Donohue, T. (2005) Particle Density and Particle Diameter: Two Important Characteristics that Influence the Permeability of Fibrous Material. *4th Australasian Congress on Applied Mechanics*, Melbourne, Australia, 531-532

[10] Ergun, S. (1952) Fluid Flow Through Packed Columns. *Chemical Engineering Progress*,48 (2), 89-94

[11] Fargette, C., Jones, M.G. and Nussbaum, G. (1997) Bench Scale Tests for the Assessment of Pneumatic Conveying Behaviour of Powders. *Powder Handling and Processing*, 9 (2), 103-110

[12] Geldart, D (1973) Types of Gas Fluidisation. *Powder Technology*, 7, 285-292

[13] Geldart, D., Harnby, N. and Wong, A.C. (1984) Fluidization of Cohesive Powders. *Powder Technology*, 37, 25-37

[14] Geldart, D. (1990) Estimation of Basic Particle Properties for use in Fluid-Particle Process Calculations. *Powder Technology*, 60, 1-13

[15] Grace, J.R. (1986) Contacting Modes of Behaviour Classification of Gas-Solid and Other Two-Phase Suspensions. *The Canadian Journal of Chemical Engineering*, 64, 353-363

[16] Heiskanen, K. (1993) *Particle Classification*. Chapman & Hall, London

[17] Hong, J., Shen, Y. and Tomita, Y. (1995) Phase Diagrams in Dense Phase Pneumatic Transport. *Powder Technology*, 84, 213-219

[18] Jones, M.G. (1988) The Influence of Bulk Particulate Properties on Pneumatic Conveying Performance, *PhD Thesis*, Thames Polytechnic, UK

[19] Jones, M.G. and Mills, D. (1990) Product Classification for Pneumatic Conveying. *Powder Handling and Processing*, 2 (2), 117-122

[20] Jones, M.G. and Williams, K.C. (2003) Solids Friction Factors for Fluidized Dense Phase Pneumatic Conveying. *Particulate Science and Technology*. 21 (1), 45-56

[21] Jones, P.J. and Leung, L.S. (1978) Estimation of saltation velocity in horizontal pneumatic conveying – a comparison of published correlations. *Pneumotransport 4*, California, USA, C1 1-12.

[22] Konrad, K (1986) Dense-Phase Pneumatic Conveying: A review. *Powder Technology*, 49, 1-35

[23] Levy, A. and Mason, D.J. (2000) Two-Layer Model for Non-Suspension Gas-Solids Flow in Pipes. *Powder Technology*, 112, 256-262

[24] Mainwaring, N.J. and Reed, A.R. (1987) Permeability and Air Retention Characteristics of Bulk Solid Materials in Relation to Modes of Dense Phase Pneumatic Conveying. *Bulk Solids Handling*, 7 (3), 415-425

[25] Mason, D.J. and Levy, A. (2001) A Model for Non-Suspension Gas-Solids Flow of Fine Powders in Pipes. *International Journal of Multiphase Flow*, 27, 415-435

[26] Mason, J.S., Mills, D., Reed, R.A. and Woodcock, C.R. (1980) Introduction to Pneumatic Conveying. *Powder Europa 80*, London, England, 1-57

[27] Mills, D., Mason, J.S. and Stacey R.B. (1982) A Design Study for the Pneumatic Conveying of a Fine Particulate Material. *The Solids Handling Conference – Solidex 82*, Harogate, England, C1-C75

[28] Molerus, O. (1982) Interpretation of Geldart's Type A, B, C and D Powders taking into account Interparticle Cohesion Force. *Powder Technology*, 33, 81-87

[29] Molerus, O. (1996) Overview: Pneumatic Transport of Solids. *Powder Technology*, 88, 309-321

[30] Muswchelknautz, E (1959) Theoretische und Experimentelle Untersuchungen über die Druckverluste Pneumatischer Förderleitungen unter Besonderer Berücksichtigung des Einflusses von Gutreibung und Gutgewicht. *VDI Forschungsheft*, No. 476

[31] Ochi, M (1991) Saltation velocity of the gas-solid two-phase flow in a horizontal pipe. *1st ASME-JSME Fluids Engineering Conference*, FED 121, 163-166

[32] Pan, R. and Wypych, P.W. (1992) Scale-up procedures for Pneumatic Conveying Design. *Powder Handling and Processing*, 4 (2), 167-172

[33] Pan, R., Mi, B. and Wypych, P.W. (1994) Pneumatic Conveying Characteristics of Fine and Granular Bulk Solids. *Kona Powder and Particle*, 12, 77-84

[34] Pan, R. and Chambers, R. (1999) Part B: Details of Test Runs and Scale Up Procedure. *Bulk Solids Handling*. 19 (3), 321-327

[35] Pan, R. (1999) Material Properties and Flow Modes in Pneumatic Conveying. *Powder Technology*, 104, 157-163

[36] Plasynski, S., Dhodapkar, S. and Klinzing, G.E. (1991) Comparison of saltation velocity and pickup velocity correlations for pneumatic conveying. *AIChE Symposium Series*, 87 (281), 78-90.

[37] Rautiainen, A. and Sarkomaa, P. (1998) Solids friction factors in upward lean gas-solids flows. *Powder Technology*, 95, 25-35.

[38] Rautiainen, A., Stewart, G., Poikolainene, V. and Sarkomaa, P. (1999) An Experimental Study of Vertical Pneumatic Conveying. *Powder Technology*, 104, 139-150

[39] Rietema, K. (1984) Powders, What are They? *Powder Technology*, 37, 5-23

[40] Rhodes, M. J. (1998) *Introduction to Particle Technology*. Wiley, Chichester, England

[41] Rizk, F. (1976) Pneumatic Conveying at Optimal Operating Conditions and a Solution of Barth's Equation $\lambda_z = \phi(\lambda_z^*, \beta)$. *Pneumotransport 3*, Bath, England, 7-9 April, D4 43-58.

[42] Roberts, A.W. (1969) An Investigation of the Gravity Flow of Noncohesive Granular Materials Through Discharge Chutes, *Journal of Engineering for Industry*, 373-381

[43] Roberts, A.W. and Scott, O.J. (1981) Flow of Bulk Solids through Transfer Chutes of Variable Geometry and Profile. *Bulk Solids Handling*, 1 (4)

[44] Roberts, A. W. (2005) Private Communication. November

[45] Sanchez, L., Vasquez, N., Klinzing, G.E. and Dhodapkar, S. (2003) Characterization of Bulk Solids to Assess Dense Phase Pneumatic Conveying. *Powder Technology*, 138, 93-117

[46] Seigel, W. (1970) Untersuchungen zur Pneumatischen Förderung Körniger Festoffe in Waagerechten Rhorleitungen und Überprüfung der Ähnlichkeitsgesetze. *VDI-Forschungebericht*, No 538

[47] Stegmaier, W (1978) Zur Berechnung der Horizontalen Pneumatischen Förderung Feinkörniger Stoffe. *Fördern und Heben*, 28 (5/6), 363-366

[48] Sutton, H.M. and Richmond, R.A. (1973) How to Improve Powder Storage and Discharge in Hoppers by Aereation. *Process Engineering*, September

[49] Szikszay, G. (1987) Feststoffreibungsbeiwert bei der Pneumatischen Dünnstromföderung. *Dissertation*, Karlsruhe, Germany

[50] Villareal, J.A. and Klinzing, G.E. (1994) Pickup Velocities Under Higher Pressure Conditions. *Powder Technology*, 80, 179-182

[51] Weber, M. (1981) Principles of Hydraulic and Pneumatic Conveying in Pipes. *Bulk Solids Handling*, 1, 57-63.

[52] Weber, M. (1982) Correlation Analysis in the Design of Pneumatic Conveying Transport Plant. *Bulk Solids Handling*, 2 , 231-233

[53] Weber, M. (1991) Friction of the Air and the Air/Solid Mixture in Pneumatic Conveying. *Bulk Solids Handling*, 11, 99-102.

[54] Wilson, K.C. (1976) A Unified Physically Based Analysis of Solid-liquid Pipeline Flow; *Proceedings of Hydrotransport 4 BHRA*, 1-16

[55] Wypych, P.W. and Arnold, P.C. (1987) On Improving Scale-up Procedures for Pneumatic Conveying Design. *Powder Technology*, 50, 281-294

[56] Wypych, P.W. (1989) Pneumatic Conveying of Bulk Solids. *PhD Thesis*, University of Wollongong, Australia

[57] Wypych, P.W. and Pan, R (1991) Determination of Air Only Pressure Drop in Pneumatic Conveying Systems. *Powder Handling and Processing*, 3 (4), 303-309

[58] Yang, W.C. (1976) *Proceedings of BHRA Pnuemotransport 3*, Bath, England, E5-E49

[59] Yi, J., Wypych, P.W. and Pan, R. (1998) Minimum conveying velocity in dilute-phase pneumatic conveying. *Powder Handling and Processing*, 10(3), 255-261.

# APPENDIX A

# Mode of flow data

| PARTICLE TYPE | PARTICLE DENSITY [kg m$^{-3}$] | LOOSE POURED BULK DENSITY [kg m$^{-3}$] | MEAN PARTICLE SIZE [m] x 10$^{-6}$ | PERMEABILITY [m$^3$ s kg$^{-1}$] x 10$^{-6}$ | VIBRATED DE-AERATION CONSTANT (JONES) [m s$^{-1}$] x 10$^{-6}$ | DE-AERATION FACTOR (MAINWARING AND REED) [kPa s m$^{-1}$] | STEADY STATE FLUIDISATION PRESSURE [kPa m$^{-1}$] | DE-AERATION TIME ($t_r$) (Equation 2.22) [s] | $N_{c(mod)}$ - CHAMBERS (Equation 2.23) [-] x 10$^{-3}$ | Ω - FARGETTE (Equation 2.24) [-] x 10$^{3}$ | *Grt* - SANCHEZ (Equation 2.26) [m$^{-1}$] x 10$^{-3}$ | *P** - SANCHEZ (Equation 2.25) [] | REFERENCE |
|---|---|---|---|---|---|---|---|---|---|---|---|---|---|
| Fly ash 1 | 2197 | 634 | 16 | - | - | - | - | - | - | - | - | - | |
| Fly ash 2 | 2217 | 957 | 12 | - | - | - | - | - | - | - | - | - | |
| pulverised coal 1 | 1600 | 538 | 42 | - | - | - | - | - | - | - | - | - | |
| pulverised coal 2 | 1590 | 541 | 15 | - | - | - | - | - | - | - | - | - | |
| pulverised coal 3 | 1590 | 563 | 20 | - | - | - | - | - | - | - | - | - | [35] |
| pulverised coal 4 | 1580 | 568 | 33 | - | - | - | - | - | - | - | - | - | |
| pulverised coal 5 | 1415 | 588 | 46 | - | - | - | - | - | - | - | - | - | |
| pulverised coal 6 | 1500 | 400 | 40 | - | - | - | - | - | - | - | - | - | |
| pulverised coal 7 | 1539 | 368 | 26 | - | - | - | - | - | - | - | - | - | |
| Pulverised Fuel Ash | 2446 | 979 | 25 | 0.60 | 2.0 | 612 | 6.5 | 94.1 | 0.0156 | 16 | 27.4 | 0.92 | |
| Copper ore | 3950 | 1660 | 55 | 0.33 | 9.8 | 41.1 | 7.5 | 5.48 | 0.238 | 10.0 | 0.45 | 0.55 | |
| Coal (pulverised) | 1550 | 393 | 84 | 0.53 | 4.3 | 83.8 | 3.5 | 23.9 | 0.0343 | 115 | 3.28 | 0.28 | |
| Flour (RHM Dem.) | 1470 | 510 | 90 | 1.30 | 6.2 | 38.2 | 2 | 19.1 | 0.0999 | 28.8 | 2.57 | 0.63 | [18] |
| PVC Powder | 990 | 615 | 90 | 1.20 | 8.0 | 15.5 | 4.5 | 3.44 | 0.346 | 4.66 | 0.69 | 0.39 | |
| Pearlite | 800 | 100 | 158 | 5.70 | 8.8 | 10.3 | 0.4 | 25.8 | 0.177 | 45.3 | 3.64 | 1.14 | |
| Iron Powder | 5710 | 2380 | 64 | 0.34 | 7.0 | 117 | 6 | 19.4 | 0.100 | 24.0 | 0.95 | 0.76 | |

| PARTICLE TYPE | PARTICLE DENSITY [kg m$^{-3}$] | LOOSE POURED BULK DENSITY [kg m$^{-3}$] | MEAN PARTICLE SIZE [m] x 10$^{-6}$ | PERMEABILITY [m$^3$ s kg$^{-1}$] x 10$^{-6}$ | VIBRATED DE-AERATION CONSTANT (JONES) [m s$^{-1}$] x 10$^{-6}$ | DE-AERATION FACTOR (MAINWARING AND REED) [kPa s m$^{-1}$] | STEADY STATE FLUIDISATION PRESSURE [kPa m$^{-1}$] | DE-AERATION TIME ($t_r$) (Equation 2.22) [s] | $N_{c(mod)}$ - CHAMBERS (Equation 2.23) [-] x 10$^{-3}$ | Ω - FARGETTE (Equation 2.24) [-] x 10$^{3}$ | *Grt* - SANCHEZ (Equation 2.26) [m$^{-1}$] x 10$^{-3}$ | *P** - SANCHEZ (Equation 2.25) [-] | REFERENCE |
|---|---|---|---|---|---|---|---|---|---|---|---|---|---|
| Granulated Sugar (degraded) | 1580 | 656 | 157 | 1.40 | 8.3 | 22.9 | 2.5 | 9.17 | 0.241 | 4.66 | 0.69 | 0.39 | [18] |
| Ag. Cat (degraded) | 4660 | 760 | 270 | 1.70 | 6.7 | 104 | 3 | 34.6 | 0.229 | 26.8 | 0.49 | 1.51 | |
| Barytes | 4250 | 1590 | 11 | 0.48 | 3.9 | 279 | 12 | 23.3 | 0.0876 | 30.5 | 8.87 | 1.93 | |
| Cement | 3060 | 1070 | 14 | 0.71 | 3.0 | 340 | 7.5 | 45.3 | 0.0479 | 59.7 | 18.8 | 1.82 | |
| cement | 3160 | 1030 | 22 | 0.50 | - | 175 | 8.7 | 20.1 | 0.0785 | 39.1 | 5.15 | 1.06 | [25] |
| pulverised coal | 1500 | 610 | 44 | 0.60 | - | 110 | 2.5 | 44.0 | 0.0205 | 120 | 11.9 | 0.425 | |
| flour | 1470 | 514 | 78 | 0.50 | - | 5 | 2.4 | 2.08 | 0.353 | 8.11 | 0.324 | 0.261 | |
| pulverised fuel ash | 2450 | 980 | 20 | 0.30 | - | 290 | 7.5 | 38.7 | 0.019 | 132 | 14.0 | 0.515 | |
| Flyash | 2510 | 810 | 11 | 0.23 | - | 20 | 5.1 | 3.92 | 0.147 | 21 | 2.53 | 0.545 | See Ch3 |
| Cement meal | 3000 | 930 | 19 | 0.08 | - | 13 | 8.5 | 1.53 | 0.157 | 20.6 | 0.478 | 0.172 | |
| Alumina | 3300 | 1050 | 78 | 0.39 | - | 1.8 | 8.2 | 0.22 | 5.69 | 0.535 | 0.0157 | 0.443 | |

| PARTICLE TYPE | PARTICLE DENSITY [kg m$^{-3}$] | LOOSE POURED BULK DENSITY [kg m$^{-3}$] | MEAN PARTICLE SIZE [m] x 10$^{-6}$ | PERMEABILITY [m$^3$ s kg$^{-1}$] x 10$^{-6}$ | VIBRATED DE-AERATION CONSTANT (JONES) [m s$^{-1}$] x 10$^{-6}$ | DE-AERATION FACTOR (MAINWARING AND REED) [kPa s m$^{-1}$] | STEADY STATE FLUIDISATION PRESSURE [kPa m$^{-1}$] | DE-AERATION TIME ($t_c$) (Equation 2.22) [s] | $N_{c(mod)}$ - CHAMBERS (Equation 2.23) [-] x 10$^{-3}$ | Ω - FARGETTE (Equation 2.24) [-] x 10$^{3}$ | *Grt* - SANCHEZ (Equation 2.26) [m$^{-1}$] x 10$^{-3}$ | *P** - SANCHEZ (Equation 2.25) [-] | REFERENCE |
|---|---|---|---|---|---|---|---|---|---|---|---|---|---|
| high silica flux | 2664 | 1519 | 300 | - | - | - | - | - | - | - | - | - | [35] |
| primary concentrate | 4742 | 2778 | 142 | - | - | - | - | - | - | - | - | - | |
| Alumina | 3600 | 1040 | 79 | 0.42 | 19 | 10.0 | 6.5 | 1.53 | 0.986 | 3.51 | 0.096 | 0.53 | |
| Coal (degraded) | 1550 | 701 | 146 | 1.0 | 2.9 | - | - | - | - | - | - | - | |
| Zircon Sand | 4600 | 2600 | 120 | 1.3 | 10 | 46.0 | 20 | 2.30 | 2.60 | 0.68 | 0.742 | 1.71 | |
| Potassium Sulphate | 2625 | 1260 | 131 | 0.99 | 18 | - | - | - | - | - | - | - | |
| Silica Sand | 2630 | 1450 | 174 | 3.9 | 34 | 2.28 | 10 | 0.23 | 45.1 | 0.0402 | 0.0089 | 2.44 | [18] |
| Magnesium sulph. | 2353 | 1010 | 224 | 6.3 | 17 | 8.14 | 6 | 1.36 | 10.9 | 0.213 | 0.0458 | 3.1 | |
| Potassium Chloride | 1987 | 1010 | 384 | 11 | 26 | 2.94 | 8 | 0.37 | 59.5 | 0.0331 | 0.0086 | 3.49 | |
| Granulated Sugar | 1580 | 890 | 458 | 20 | 13 | 9.35 | 5 | 1.87 | 16.9 | 0.105 | 0.0460 | 4.62 | |
| Coal (as Supplied) | 1550 | 870 | 778 | 42 | 24 | - | - | - | - | - | - | - | |
| Ag. Catalyst (ICI) | 4655 | 767 | 782 | 23 | 23 | 8.8 | 4.5 | 1.96 | 54.8 | 0.111 | 0.0096 | 12.0 | |
| slate dust | 2860 | 1280 | 500 | 0.6 | - | 4.5 | 11 | 0.400 | 4.27 | 0.523 | 0.0050 | 0.240 | |
| zircon sand | 4610 | 2600 | 115 | 1.3 | - | 62.4 | 20 | 3.12 | 1.92 | 0.923 | 0.105 | 1.75 | [25] |
| pulverised fuel ash (grits) | 2380 | 400 | 700 | 11 | - | 0.18 | 2 | 0.090 | 276 | 0.0215 | 0.00101 | 3.10 | |

| PARTICLE TYPE | PARTICLE DENSITY [kg m$^{-3}$] | LOOSE POURED BULK DENSITY [kg m$^{-3}$] | MEAN PARTICLE SIZE [m] x 10$^{-6}$ | PERMEABILITY [m$^3$ s kg$^{-1}$] x 10$^{-6}$ | VIBRATED DE-AERATION CONSTANT (JONES) [m s$^{-1}$] x 10$^{-6}$ | DE-AERATION FACTOR (MAINWARING AND REED) [kPa s m$^{-1}$] | STEADY STATE FLUIDISATION PRESSURE [kPa m$^{-1}$] | DE-AERATION TIME ($t_c$) (Equation 2.22) [s] | $N_{c(mod)}$ - CHAMBERS (Equation 2.23) [-] x 10$^{-3}$ | Ω - FARGETTE (Equation 2.24) [-] x 10$^{3}$ | *Grt* - SANCHEZ (Equation 2.26) [m$^{-1}$] x 10$^{-3}$ | *P** - SANCHEZ (Equation 2.25) [-] | REFERENCE |
|---|---|---|---|---|---|---|---|---|---|---|---|---|---|
| narasin | 1745 | 880 | 325 | - | - | - | - | - | - | - | - | - | |
| BPP | 834 | 458 | 3760 | - | - | - | - | - | - | - | - | - | |
| WPP 1 | 1039 | 637 | 2980 | - | - | - | - | - | - | - | - | - | |
| WPP 2 | 865 | 494 | 3120 | - | - | - | - | - | - | - | - | - | |
| WPP 3 | 887 | 538 | 3684 | - | - | - | - | - | - | - | - | - | |
| WPP 4 | 895 | 526 | 3747 | - | - | - | - | - | - | - | - | - | [35] |
| wheat 1 | 1356 | 775 | 3788 | - | - | - | - | - | - | - | - | - | |
| wheat 2 | 1416 | 778 | 3502 | - | - | - | - | - | - | - | - | - | |
| duaralina | 1494 | 688 | 349 | - | - | - | - | - | - | - | - | - | |
| semolina | 1459 | 736 | 390 | - | - | - | - | - | - | - | - | - | |
| wheat 3 | 1449 | 811 | 3470 | - | - | - | - | - | - | - | - | - | |
| barley | 1350 | 722 | 3910 | - | - | - | - | - | - | - | - | - | |
| mustard seed | 1180 | 680 | 1650 | 129 | - | 0.46 | 4.8 | 0.10 | 1590 | 0.00109 | 0.000877 | 11.7 | |
| polyethylene pwd | 990 | 480 | 825 | 20 | - | 0.43 | 3.1 | 0.14 | 143 | 0.0144 | 0.00302 | 2.16 | |
| sand | 2620 | 1540 | 1020 | 62 | - | 0.45 | 11.8 | 0.04 | 4260 | 0.000399 | 0.000254 | 15.9 | [25] |
| polyethylene pellets | 914 | 558 | 3850 | 80 | - | 0.40 | 3.8 | 0.11 | 695 | 0.00236 | 0.000533 | 3.69 | |
| granulated sugar | 1590 | 820 | 720 | 21 | - | 2.4 | 6.0 | 0.40 | 83.5 | 0.0232 | 0.00622 | 3.90 | |
| Polyethelene Pellets | 912 | 540 | 4000 | 420 | 60 | - | - | - | - | - | - | - | [18] |
| Mustard Seed | 990 | 480 | 825 | 129 | 37 | 0.46 | 4.8 | 0.10 | 1590 | 0.00109 | 0.000877 | 11.7 | |

# APPENDIX B

# Bulk material data

# CEMENT MEAL

## Fluidisation Tests

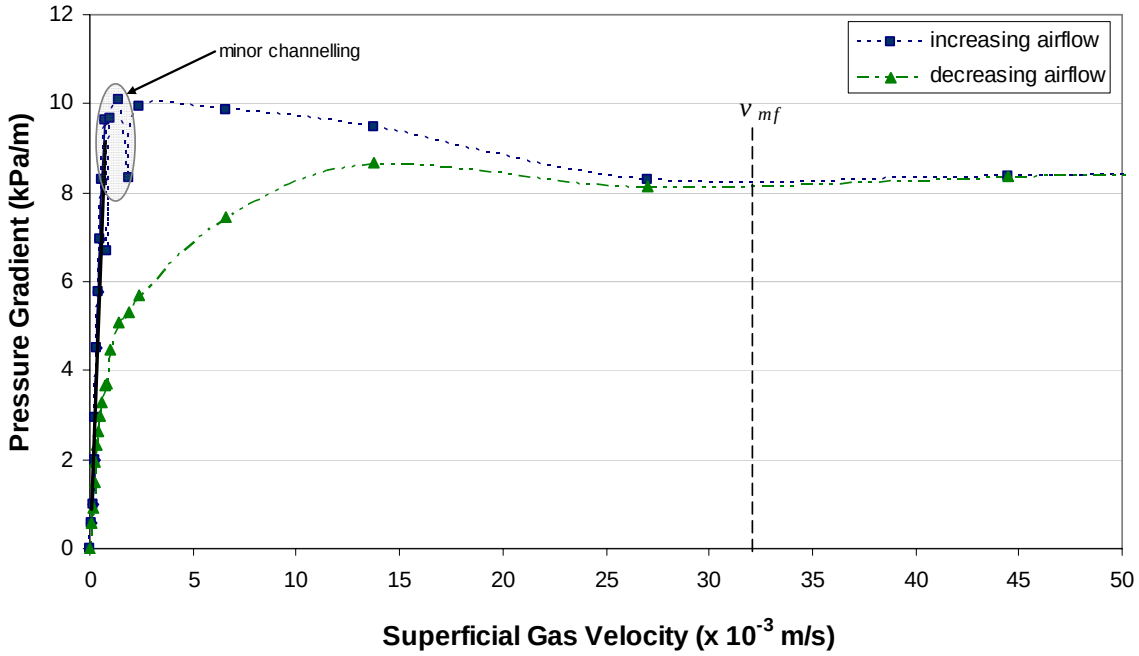


## De-aeration Test

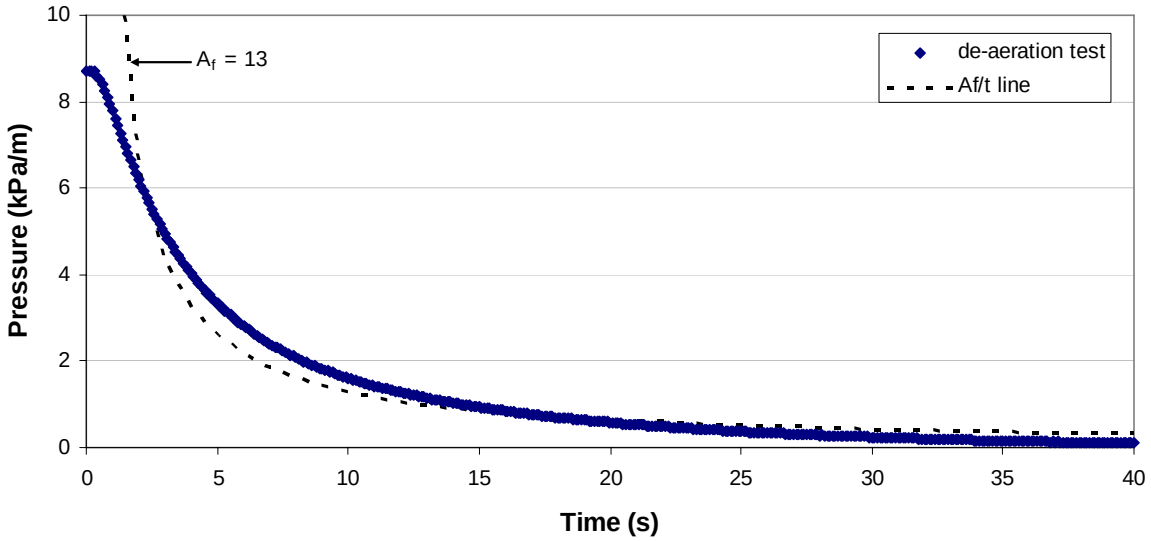

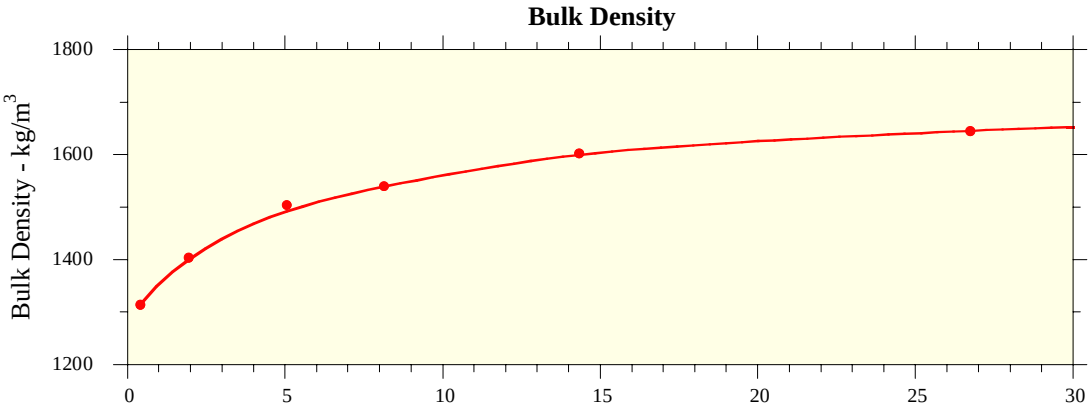


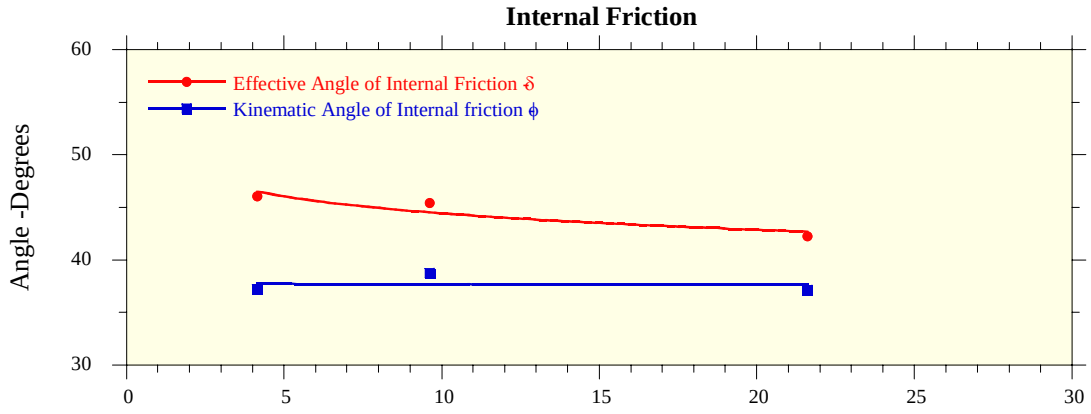


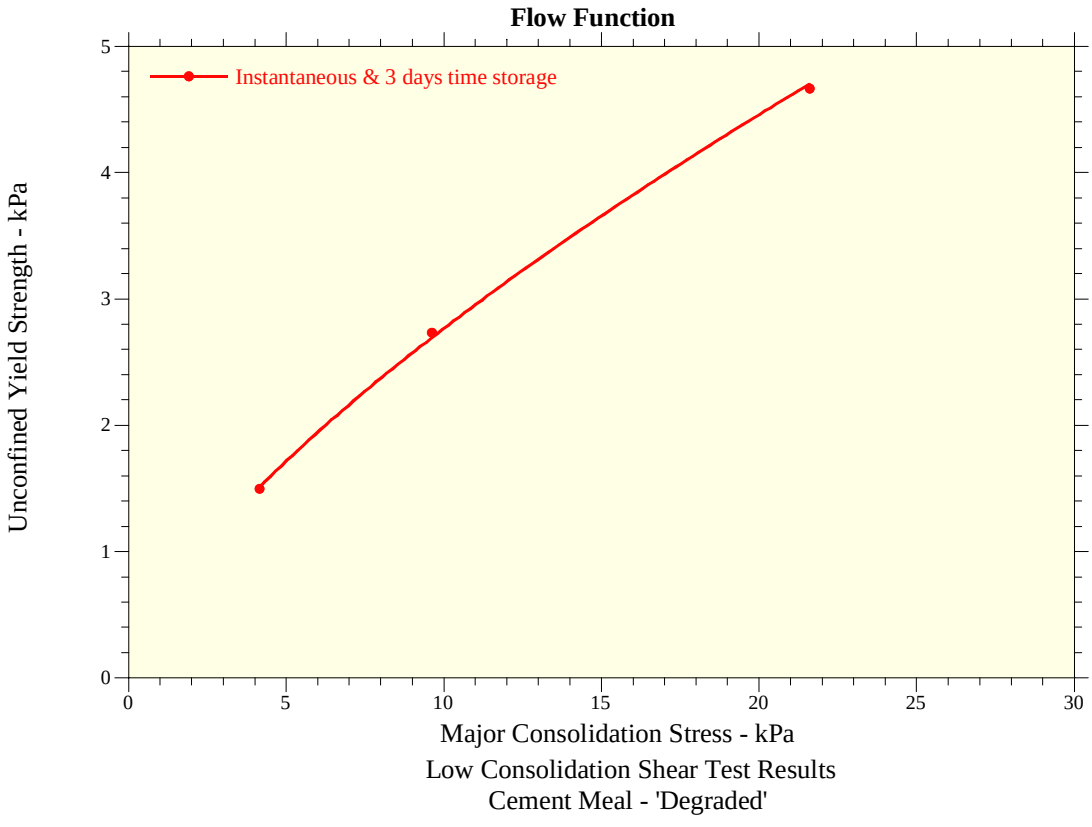


Low Consolidation Shear Test Results
Cement Meal - 'Degraded'

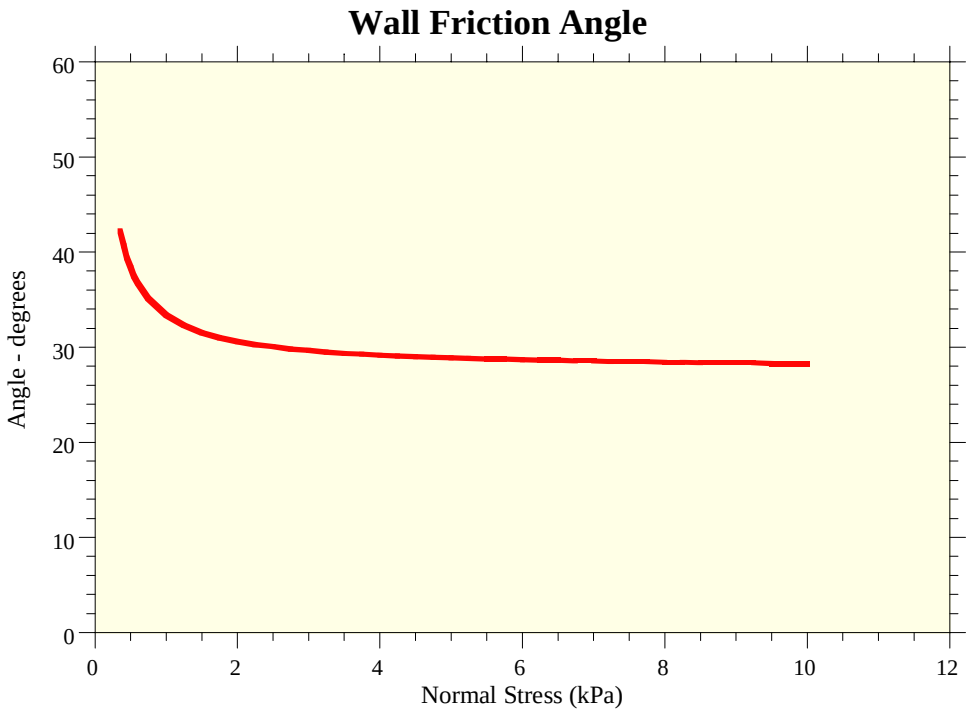


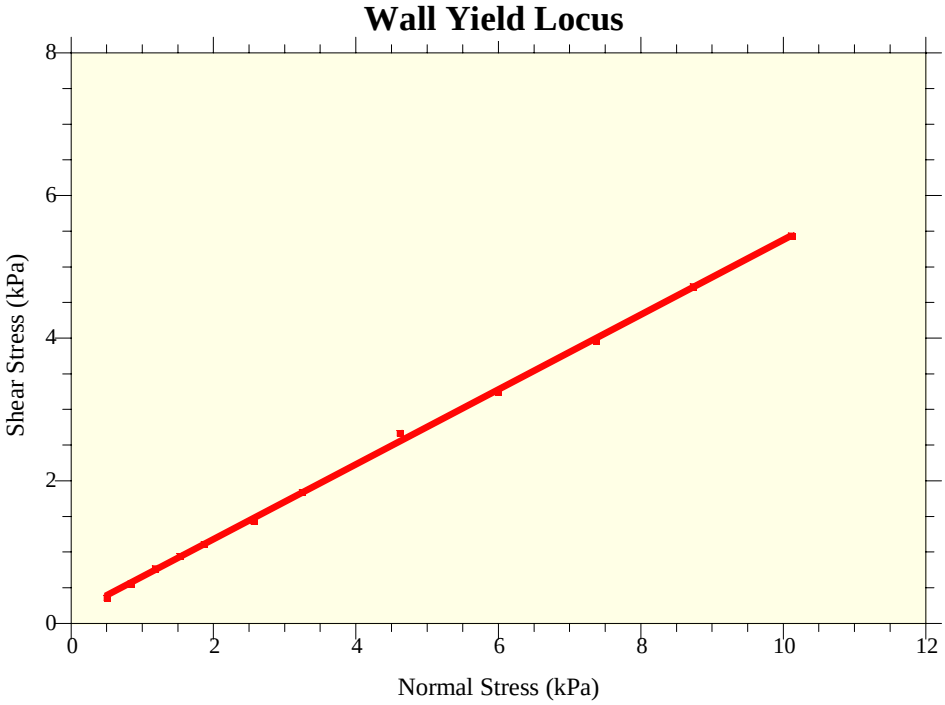


MSMS - Wall Friction Test Results
Cement Meal - 'Degraded'

# FLYASH

## Fluidisation Test

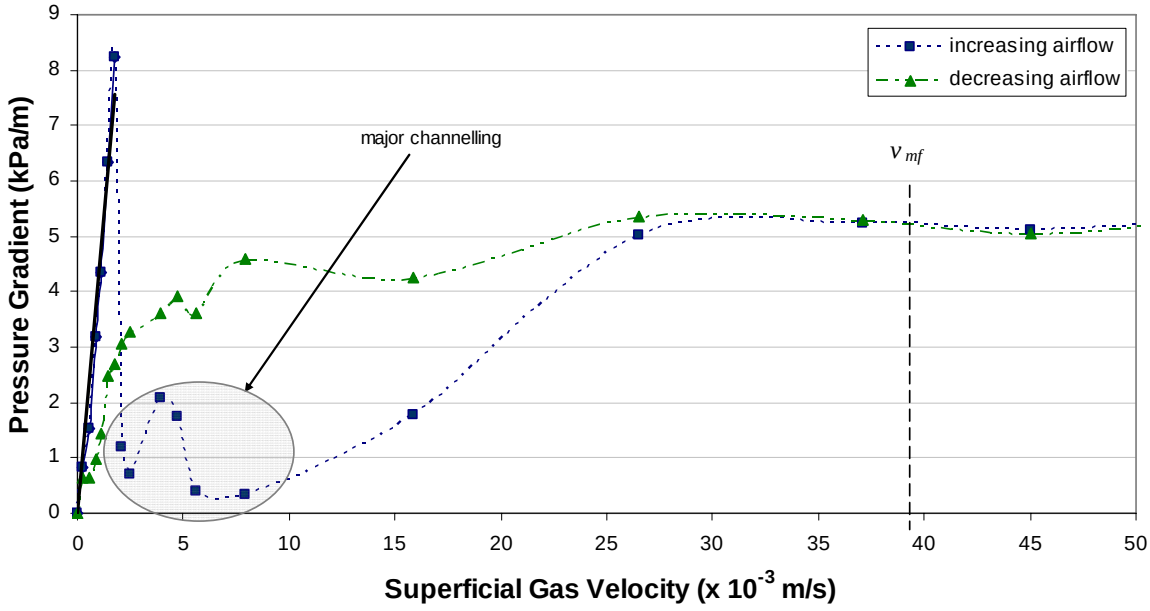


## De-aeration Test

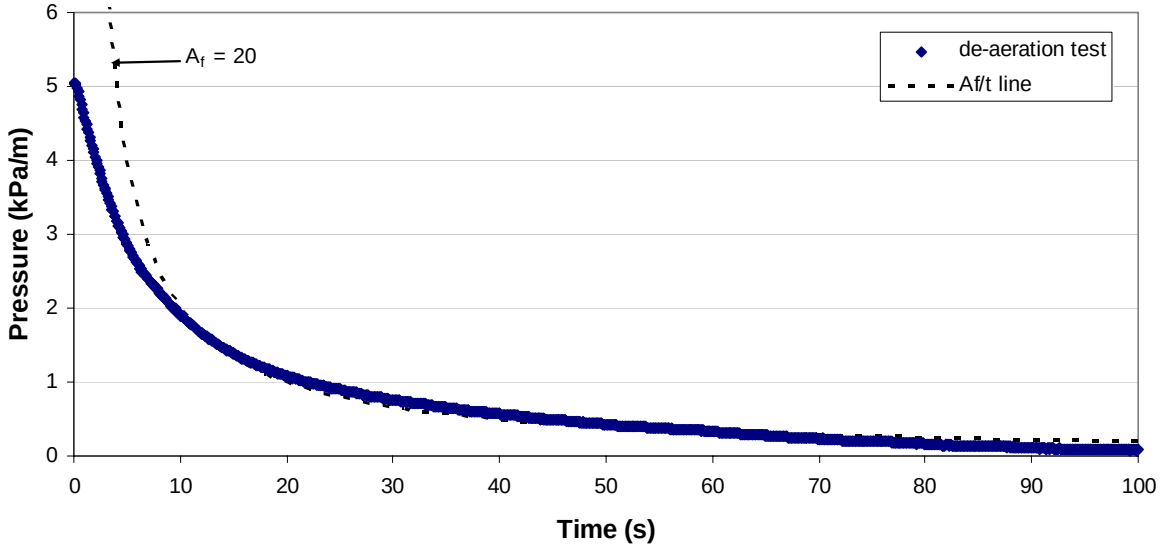

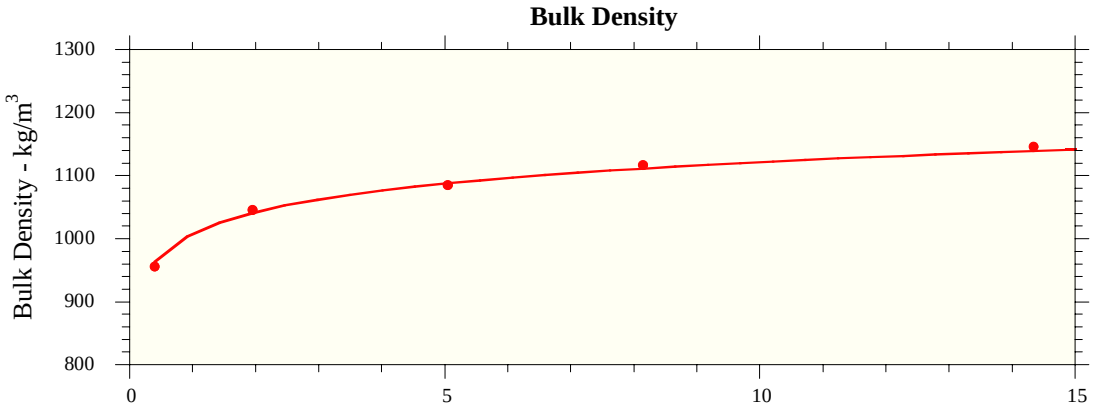


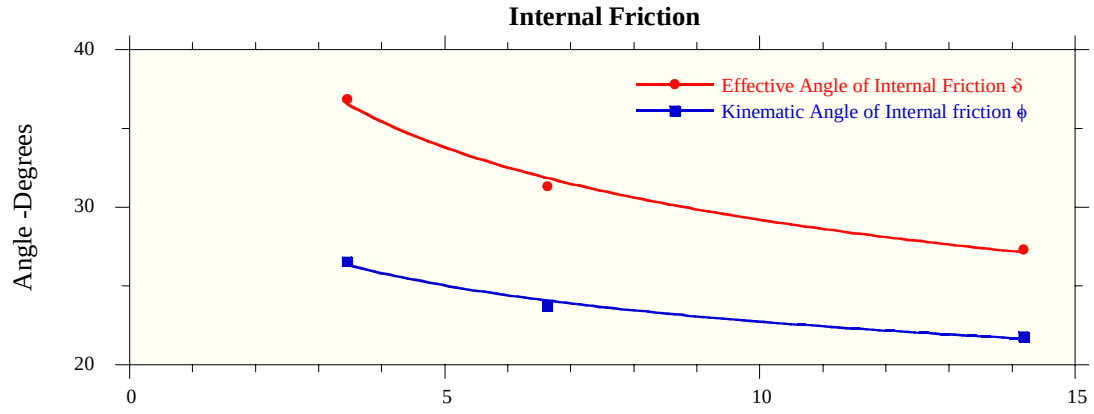


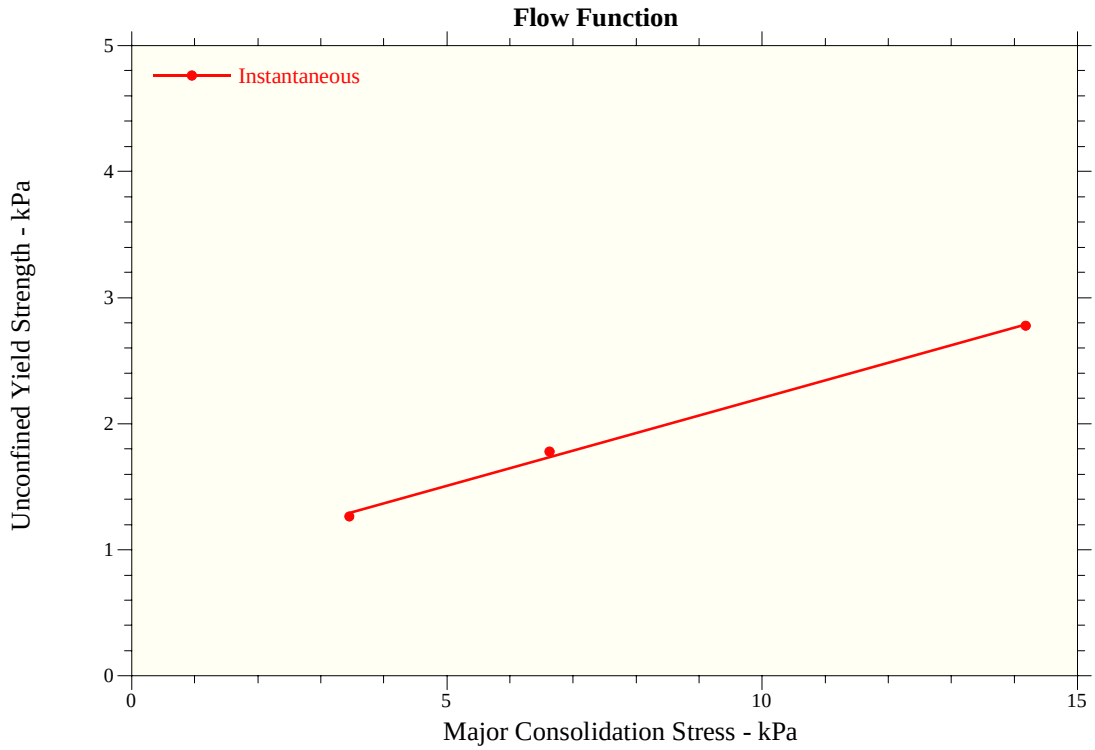


Low Consolidation Shear Test Results
Fly Ash - 'As Supplied '

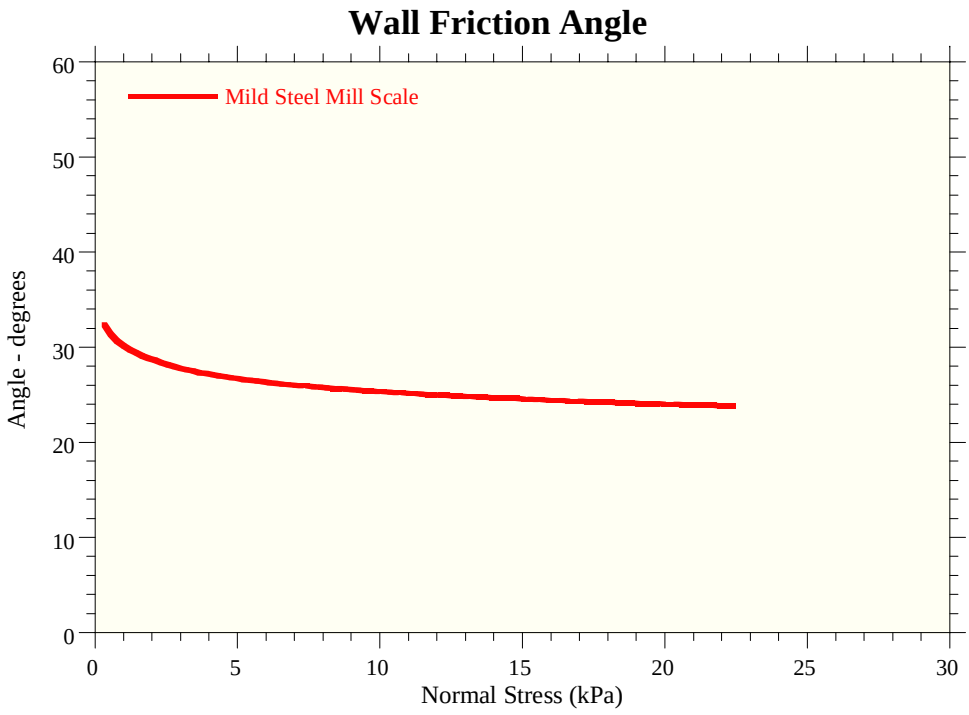


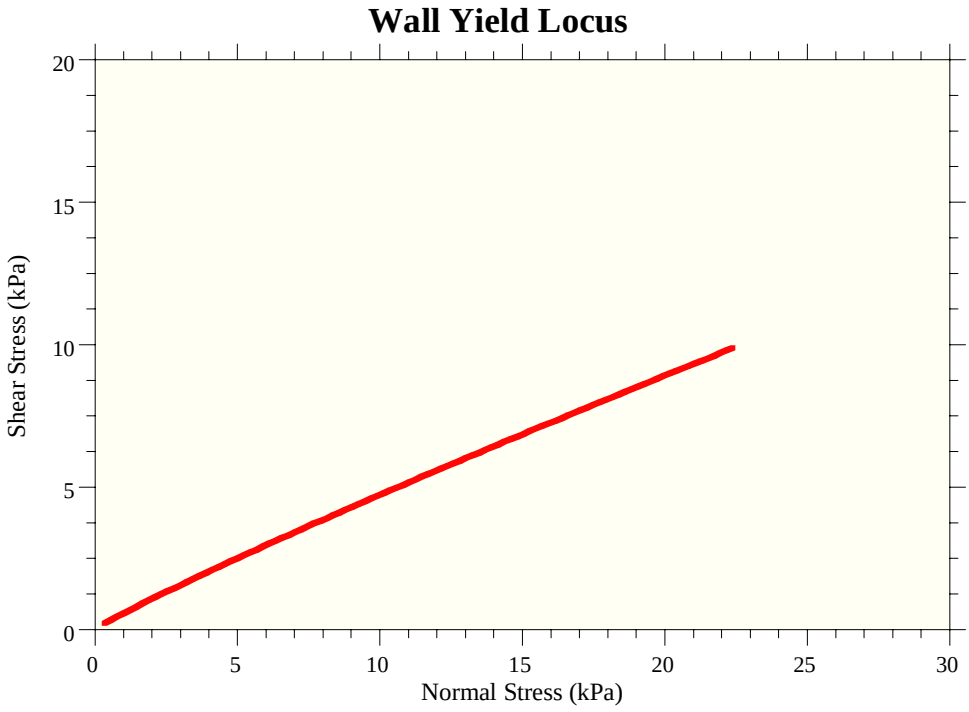


Wall Friction Test Results
Fly Ash - 'As Supplied'

# ALUMINA

## Fluidisation Test

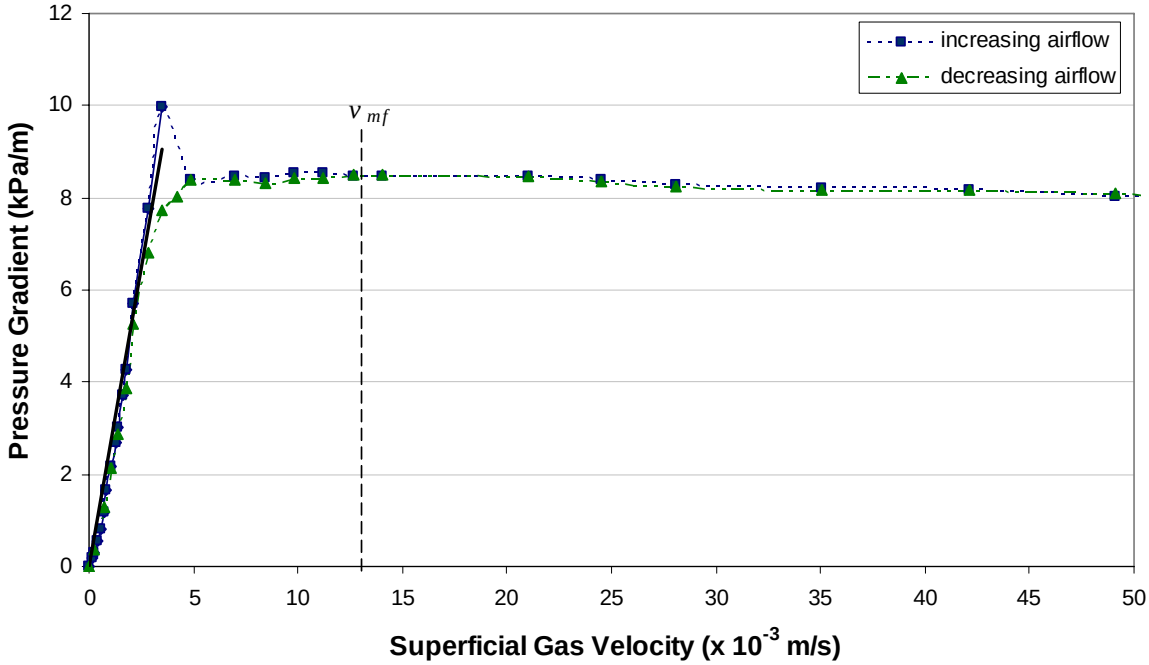


## De-aeration Test

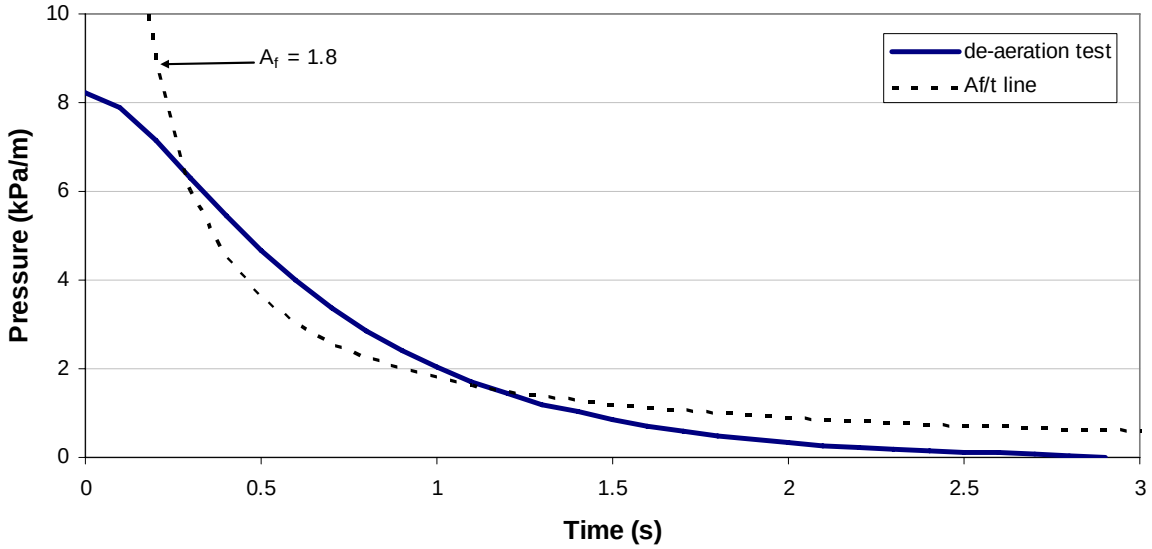

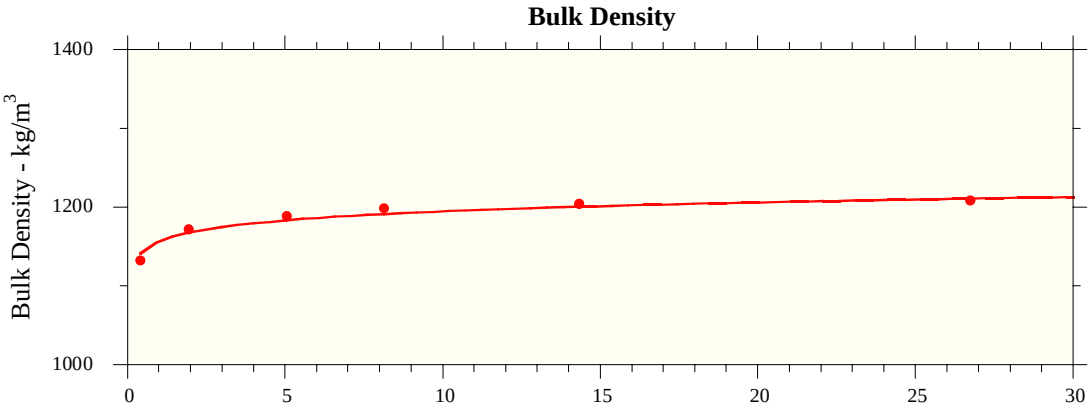


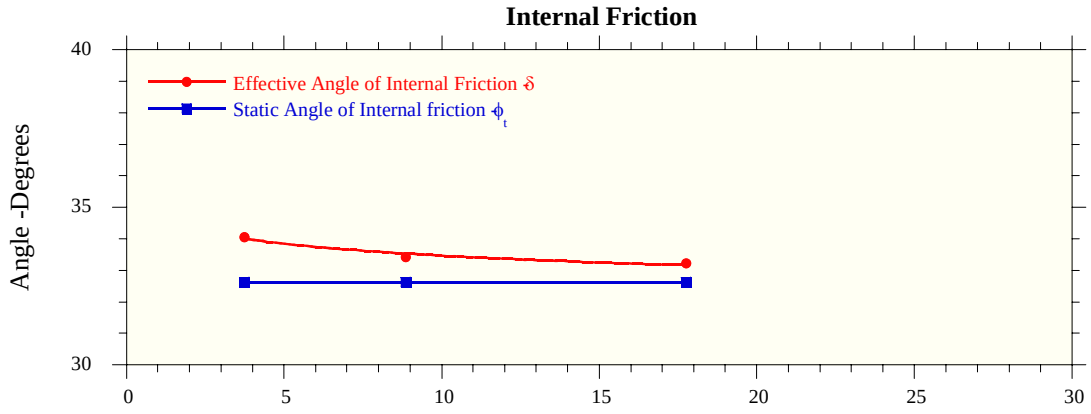


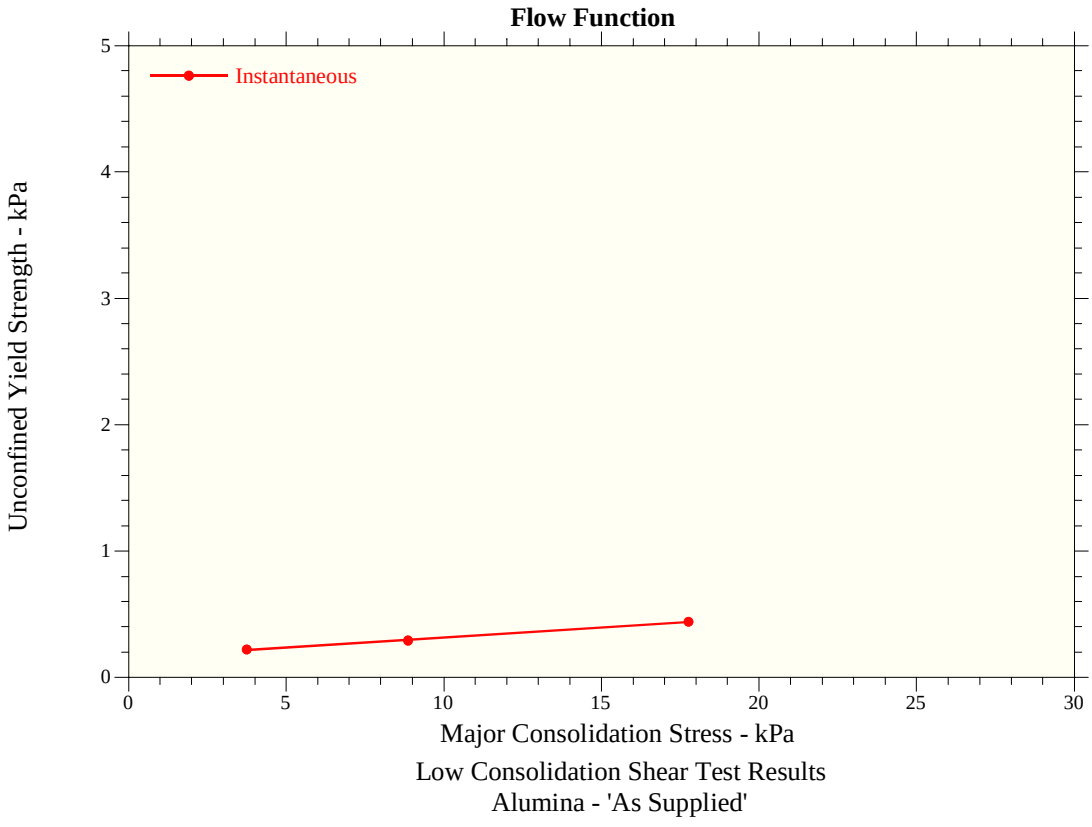


Low Consolidation Shear Test Results
Alumina - 'As Supplied'

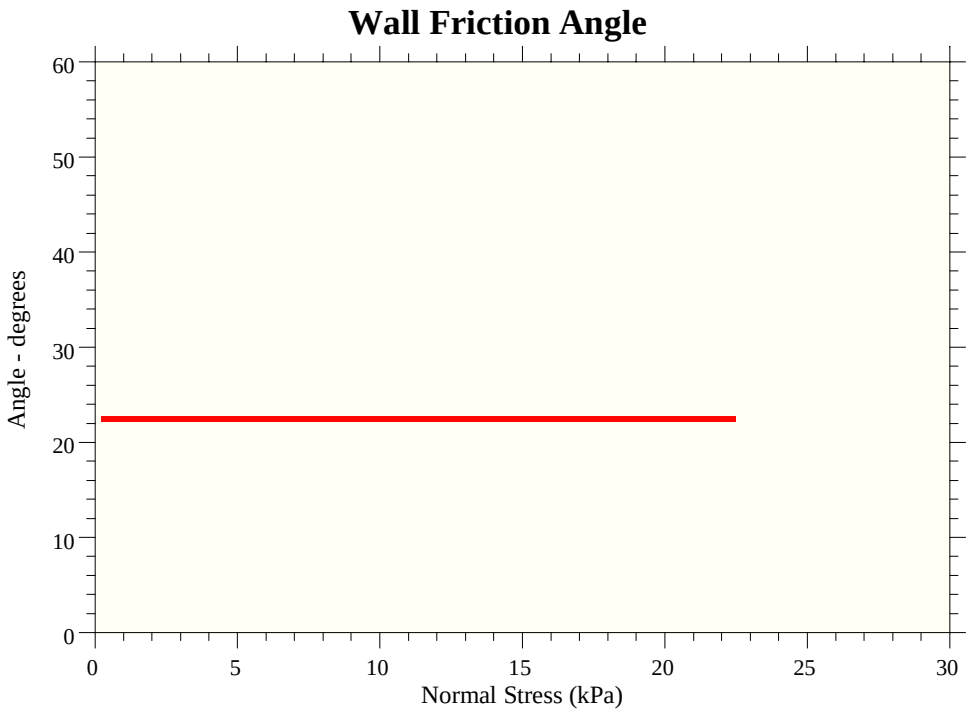


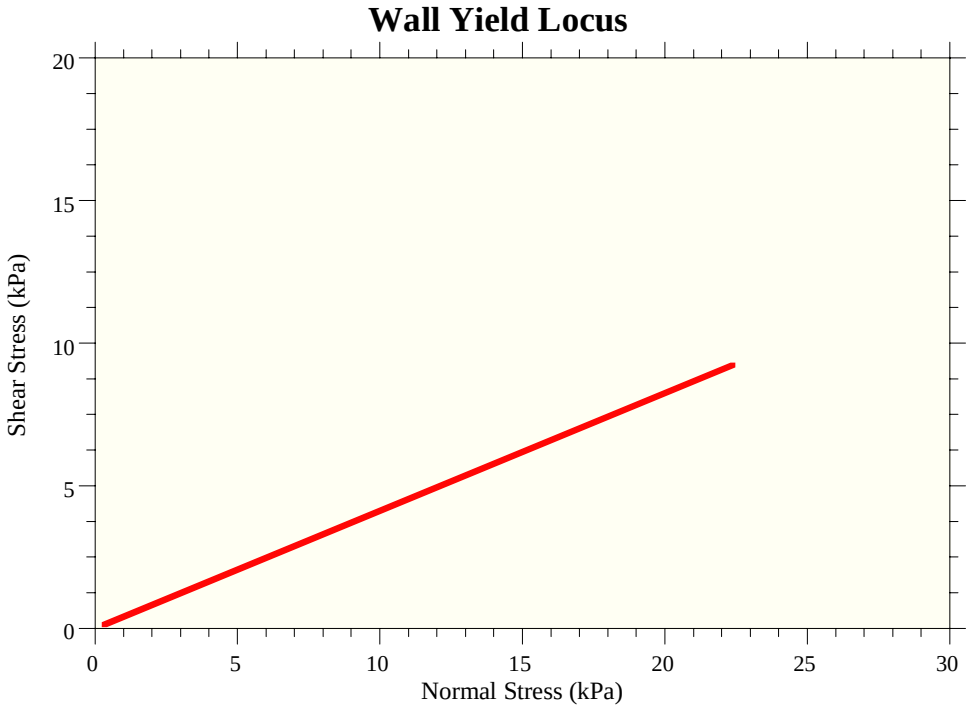


MSMS - Wall Friction Test Results
Alumina - 'As Supplied'

# APPENDIX C

# Solids friction correlations

# Cement Meal

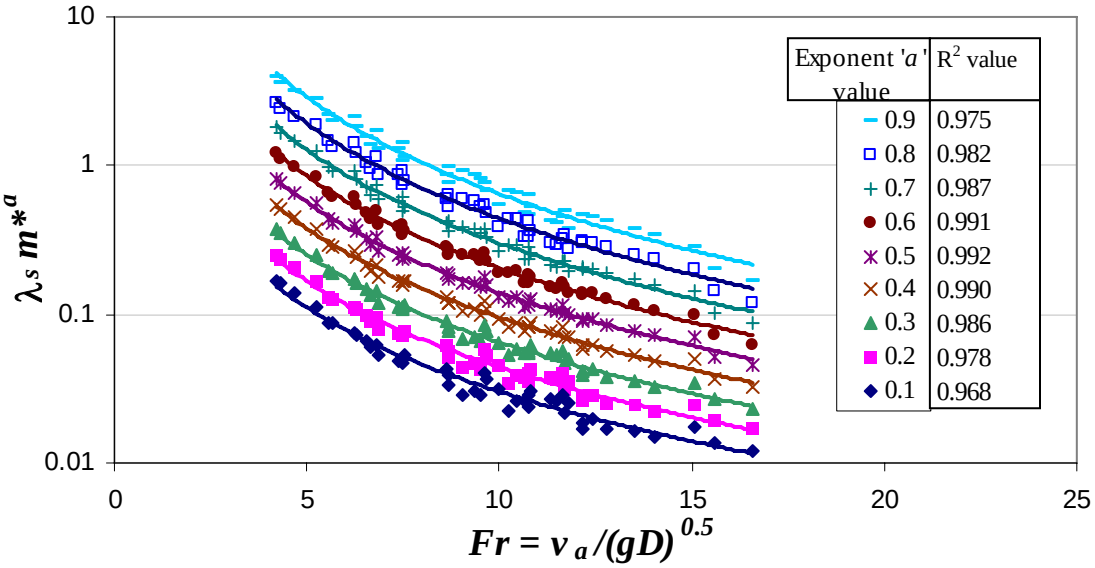
10
1
0.1
0.01
0
5
10
15
20
25
$\lambda_s m^{*a}$
$Fr = v_a/(gD)^{0.5}$
Exponent 'a' value
$R^2$ value
0.9 0.975
0.8 0.982
0.7 0.987
0.6 0.991
0.5 0.992
0.4 0.990
0.3 0.986
0.2 0.978
0.1 0.968

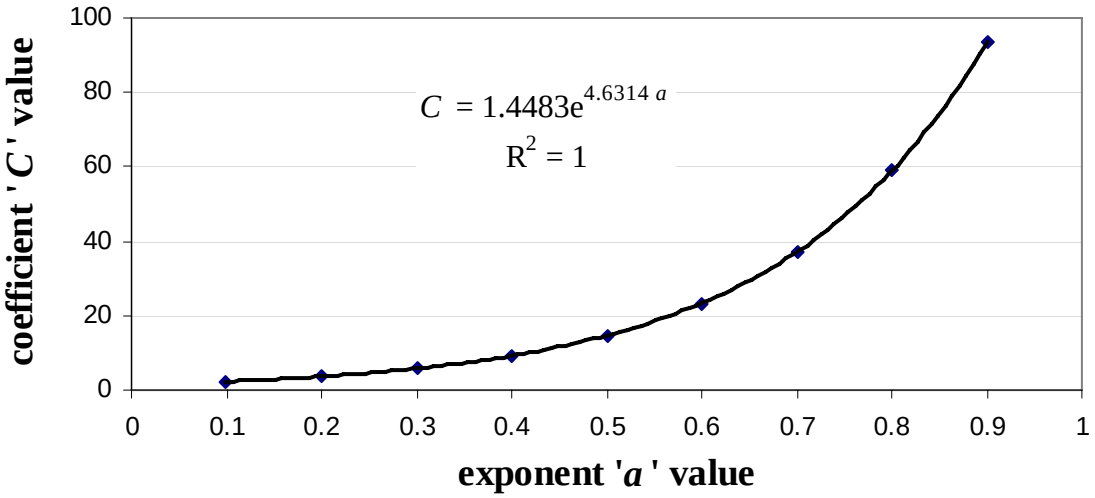
100
80
60
40
20
0
0
0.1
0.2
0.3
0.4
0.5
0.6
0.7
0.8
0.9
1
coefficient 'C' value
$C = 1.4483e^{4.6314\,a}$
$R^2 = 1$
exponent 'a' value

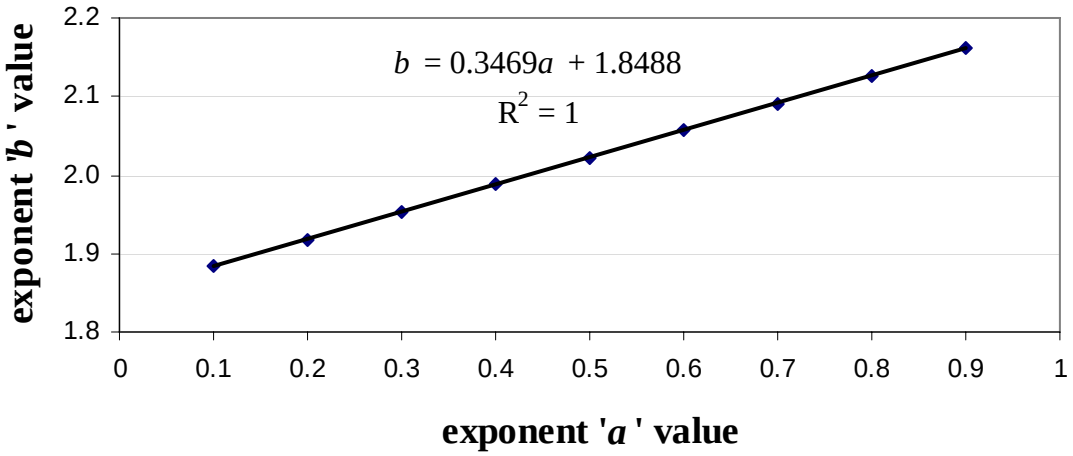
2.2
2.1
2.0
1.9
1.8
0
0.1
0.2
0.3
0.4
0.5
0.6
0.7
0.8
0.9
1
exponent 'b' value
$b = 0.3469a + 1.8488$
$R^2 = 1$
exponent 'a' value

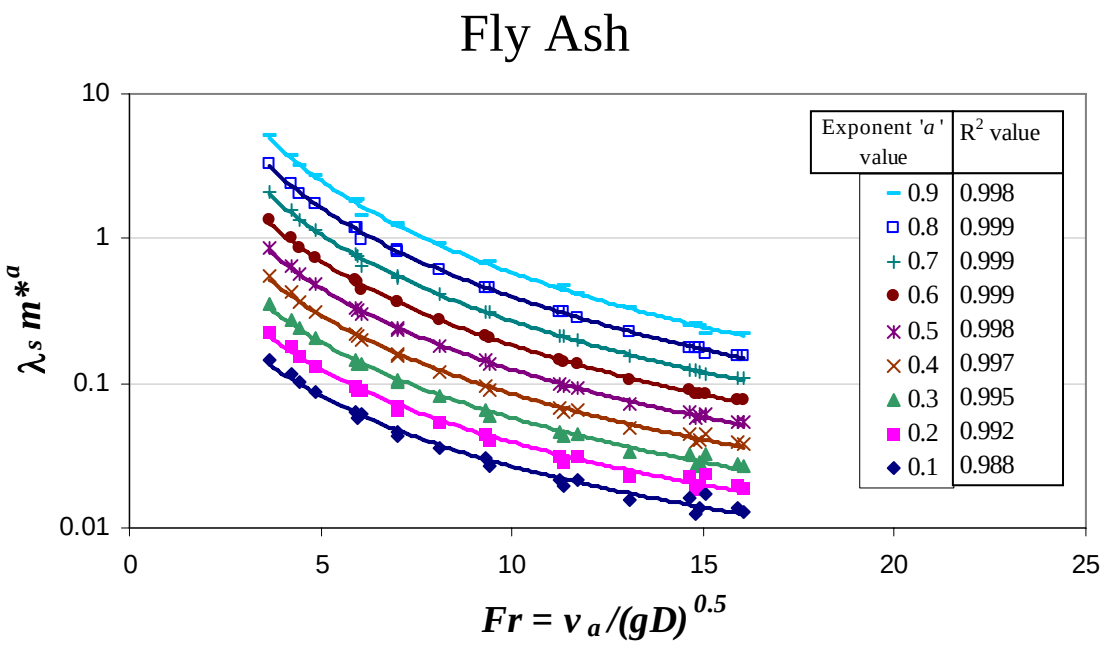
Fly Ash
10
1
0.1
0.01
0
5
10
15
20
25
$\lambda_s m^{*a}$
$Fr = v_a/(gD)^{0.5}$
Exponent 'a' value
$R^2$ value
0.9 0.998
0.8 0.999
0.7 0.999
0.6 0.999
0.5 0.998
0.4 0.997
0.3 0.995
0.2 0.992
0.1 0.988

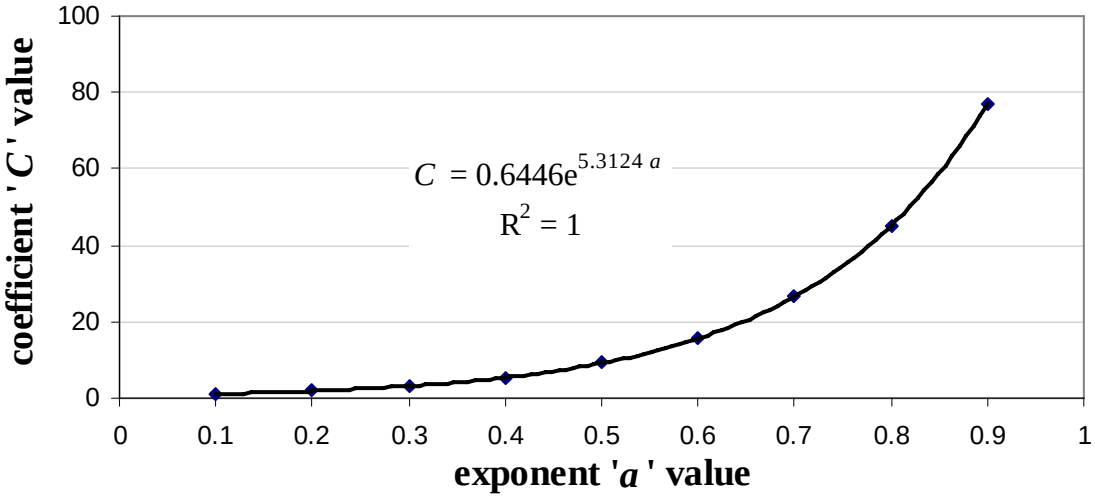
100
80
60
40
20
0
0
0.1
0.2
0.3
0.4
0.5
0.6
0.7
0.8
0.9
1
coefficient 'C' value
exponent 'a' value
$C = 0.6446e^{5.3124\,a}$
$R^2 = 1$

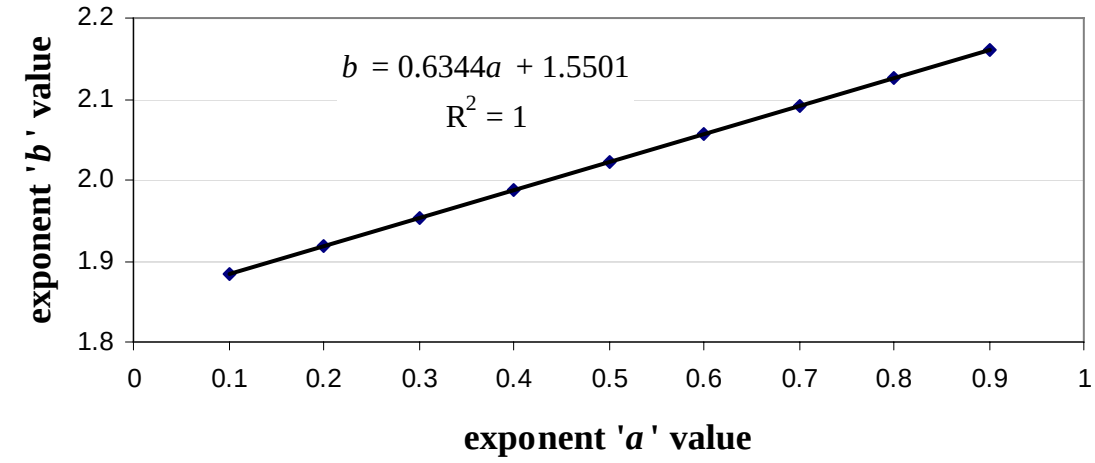
2.2
2.1
2.0
1.9
1.8
0
0.1
0.2
0.3
0.4
0.5
0.6
0.7
0.8
0.9
1
exponent 'b' value
exponent 'a' value
$b = 0.6344a + 1.5501$
$R^2 = 1$

# Alumina

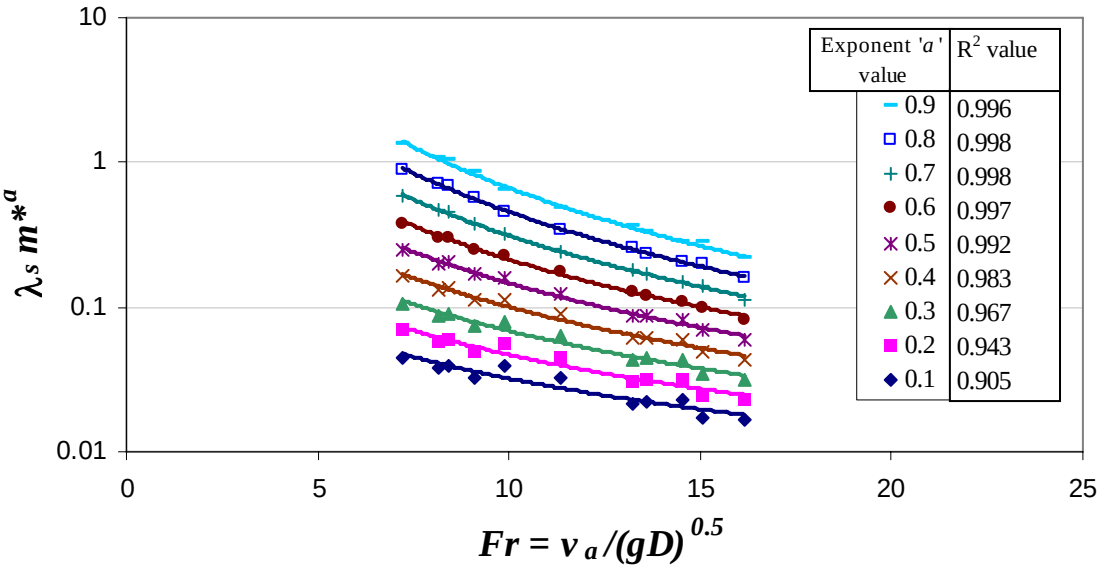
Exponent 'a' value
R2 value
0.9 0.996
0.8 0.998
0.7 0.998
0.6 0.997
0.5 0.992
0.4 0.983
0.3 0.967
0.2 0.943
0.1 0.905
λs m*a
Fr = va/(gD)0.5

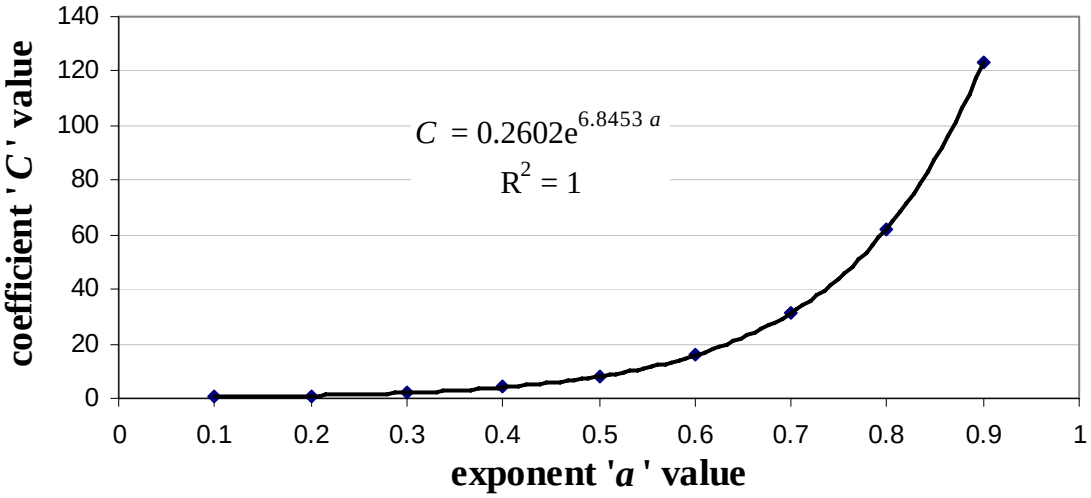
C = 0.2602e6.8453 a
R2 = 1
coefficient 'C' value
exponent 'a' value

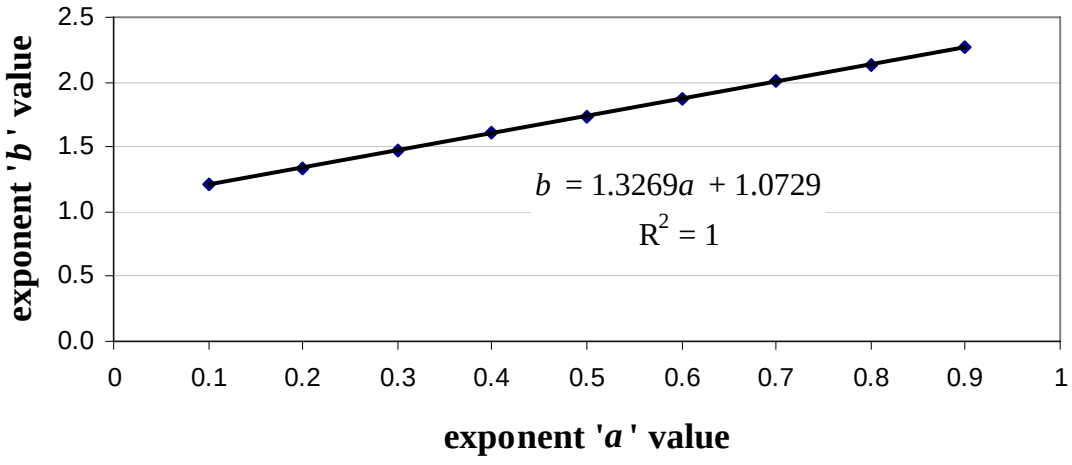
b = 1.3269a + 1.0729
R2 = 1
exponent 'b' value
exponent 'a' value

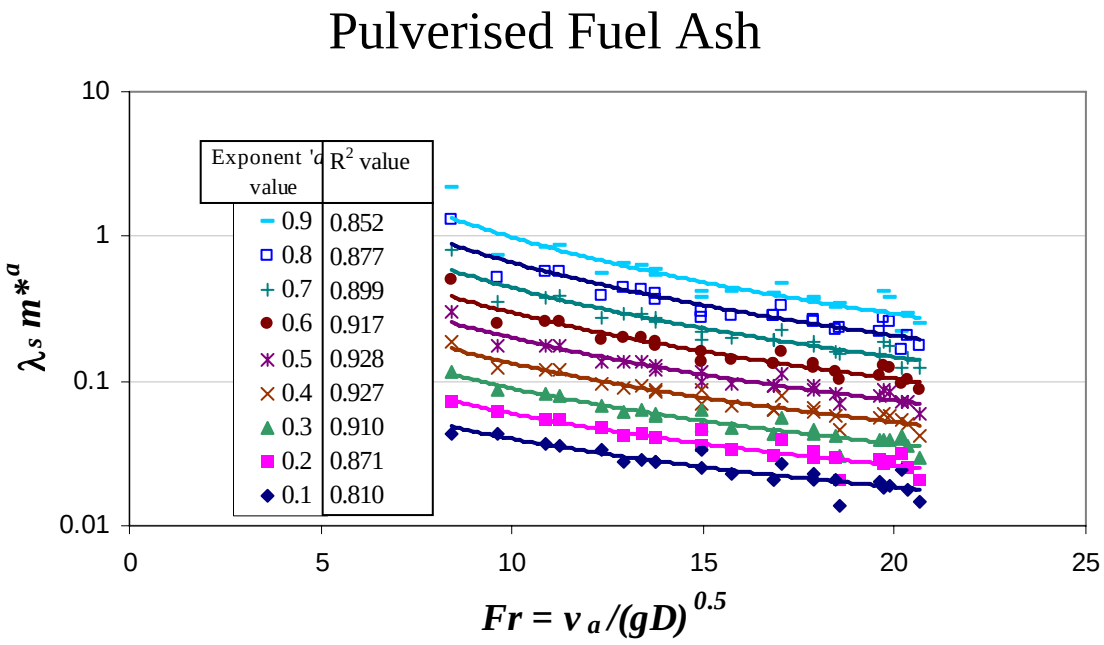
Pulverised Fuel Ash
Exponent 'a' value
R2 value
0.9 0.852
0.8 0.877
0.7 0.899
0.6 0.917
0.5 0.928
0.4 0.927
0.3 0.910
0.2 0.871
0.1 0.810
λs m*a
Fr = va/(gD)0.5

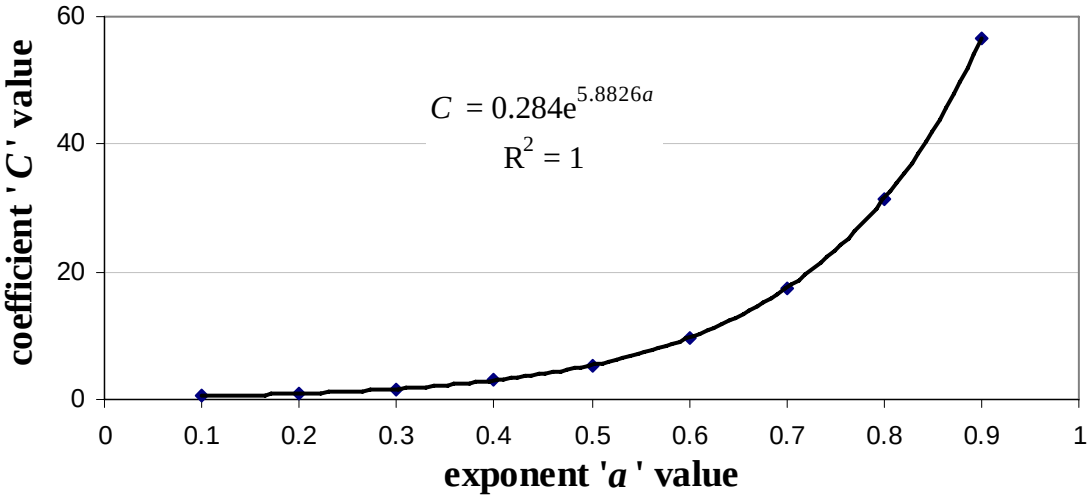
C = 0.284e5.8826a
R2 = 1
coefficient 'C' value
exponent 'a' value

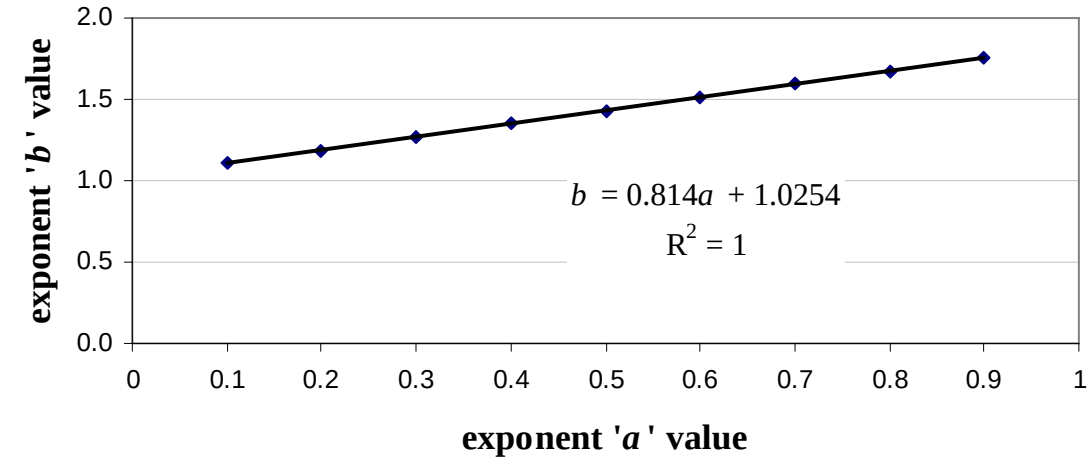
b = 0.814a + 1.0254
R2 = 1
exponent 'b' value
exponent 'a' value

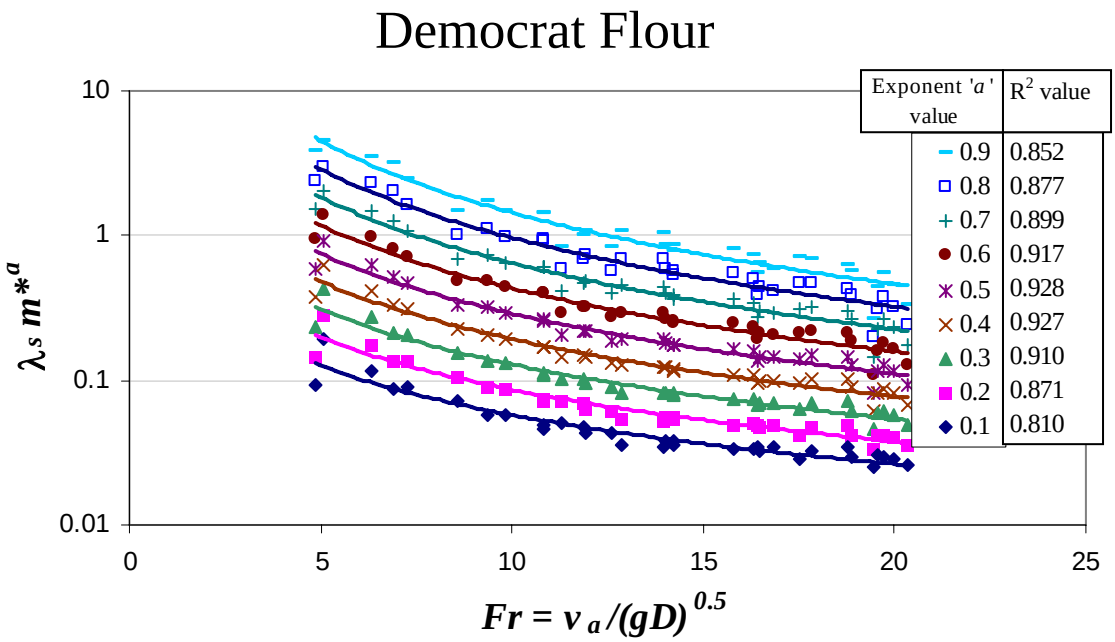
Democrat Flour
Exponent 'a' value
R2 value
0.9 0.852
0.8 0.877
0.7 0.899
0.6 0.917
0.5 0.928
0.4 0.927
0.3 0.910
0.2 0.871
0.1 0.810
λs m*a
Fr = va/(gD)0.5

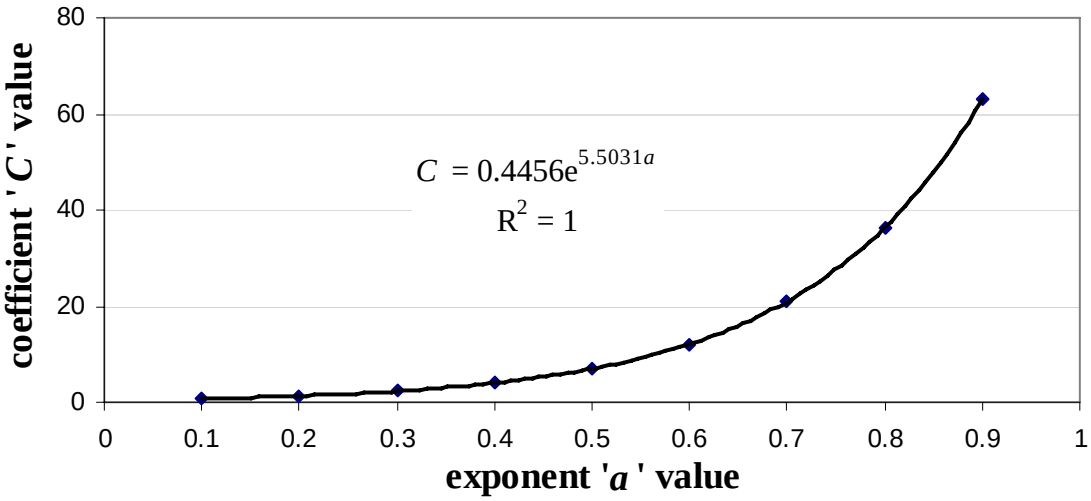
C = 0.4456e5.5031a
R2 = 1
coefficient 'C' value
exponent 'a' value

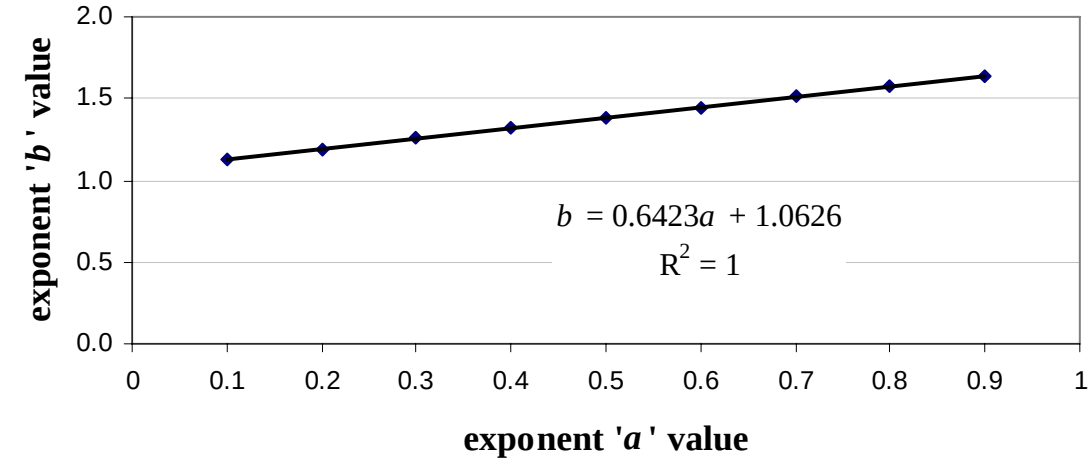
b = 0.6423a + 1.0626
R2 = 1
exponent 'b' value
exponent 'a' value

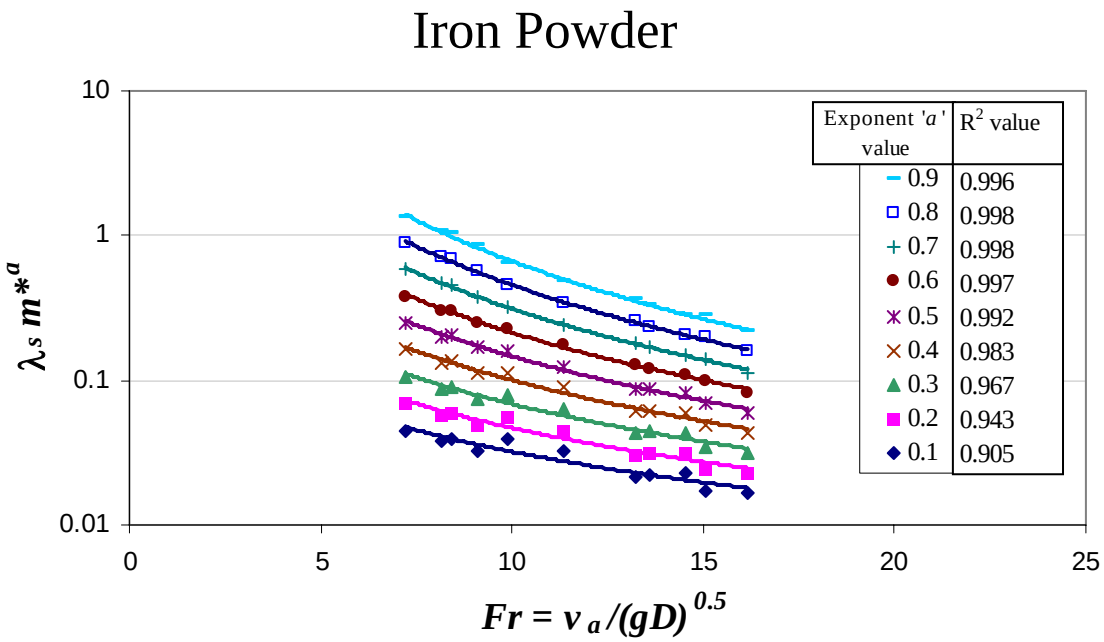
Iron Powder
10
1
0.1
0.01
0
5
10
15
20
25
$\lambda_s m^{*a}$
$Fr = v_a/(gD)^{0.5}$
Exponent 'a' value
$R^2$ value
0.9 0.996
0.8 0.998
0.7 0.998
0.6 0.997
0.5 0.992
0.4 0.983
0.3 0.967
0.2 0.943
0.1 0.905

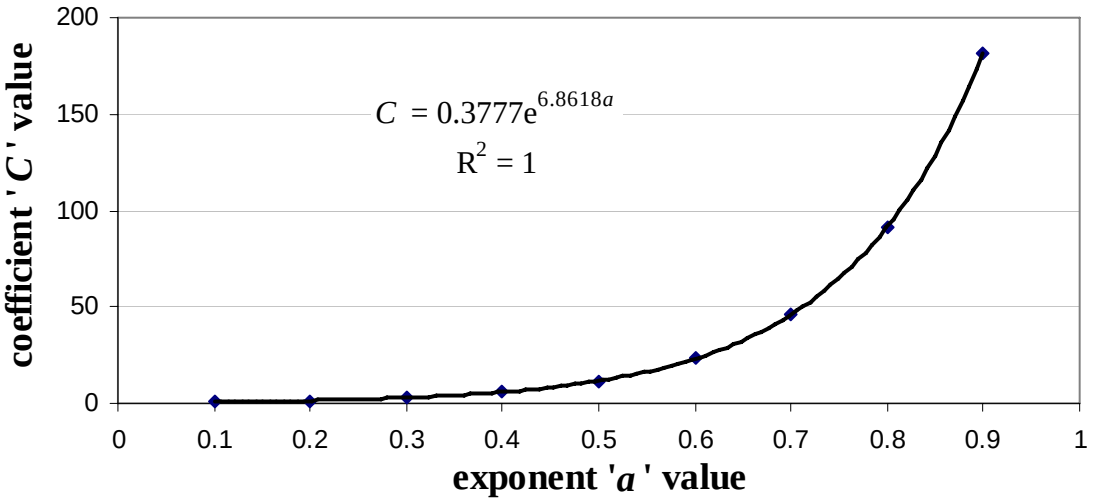
200
150
100
50
0
0
0.1
0.2
0.3
0.4
0.5
0.6
0.7
0.8
0.9
1
coefficient 'C' value
exponent 'a' value
$C = 0.3777e^{6.8618a}$
$R^2 = 1$

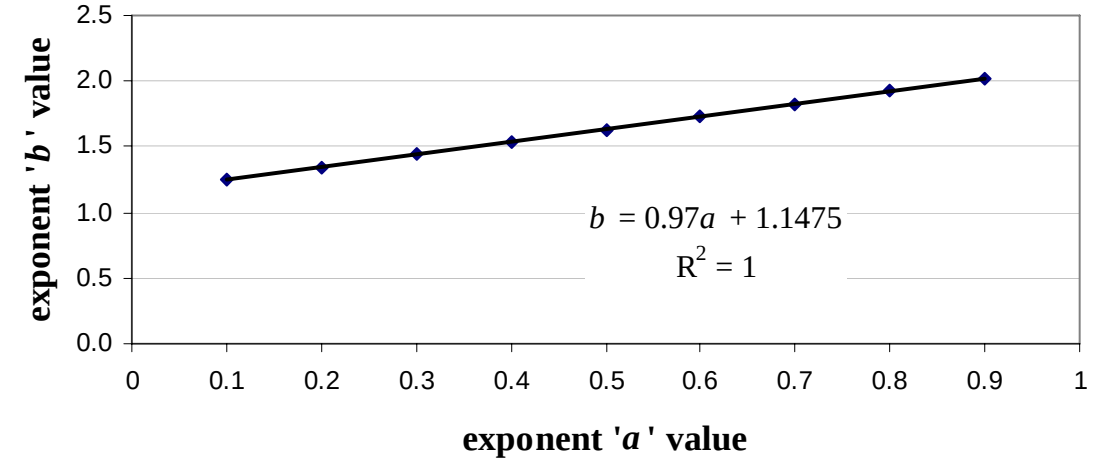
2.5
2.0
1.5
1.0
0.5
0.0
0
0.1
0.2
0.3
0.4
0.5
0.6
0.7
0.8
0.9
1
exponent 'b' value
exponent 'a' value
$b = 0.97a + 1.1475$
$R^2 = 1$

# APPENDIX D

# Derivation of solids velocity differential equations

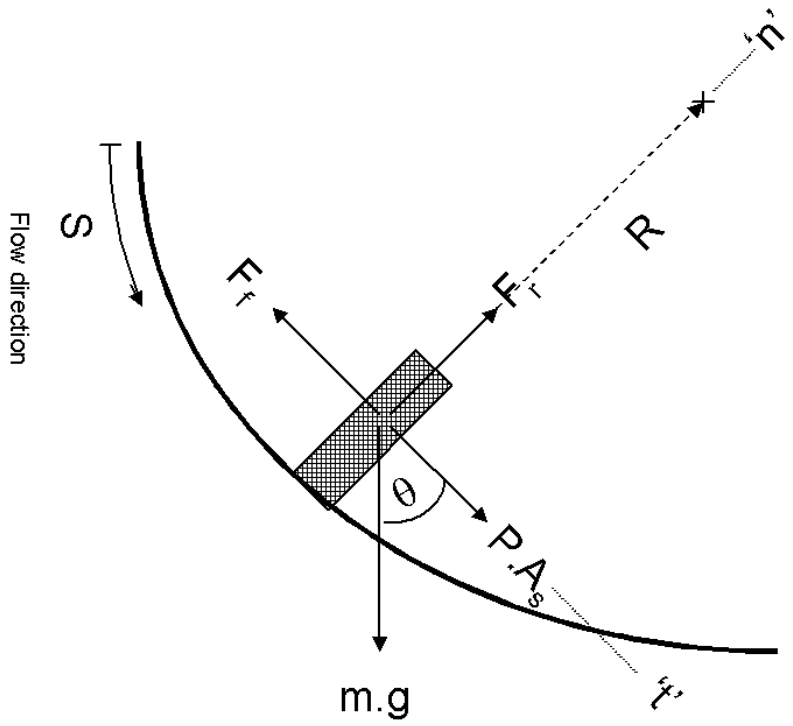


If we consider an elemental slice of material at some position and time flowing around a bend (as shown above), the sum the forces in the 't' direction of the moving coordinate system are;

$$\Sigma F_t = ma_t = P.A_s - F_f + mg\cos\theta \tag{D1}$$

By considering the acceleration of the slice and applying the differential equation chain rule, the tangential acceleration can be defined as;

$$a_t = \frac{dv_s}{dt} = \frac{dS}{dt}\frac{dv_s}{dS} = v_s\frac{dv_s}{dS} \tag{D2}$$

While, the sum of the forces in the radial direction are:

$$\Sigma F_n = ma_n = F_R - mg\sin\theta = m\frac{v_s^2}{R} \tag{D3}$$

where the frictional force ($F_f$) and the radial force ($F_R$) are defined as:

$$F_f = \lambda_s F_R \tag{D4}$$

$$F_R = m\left(\frac{v_s^2}{R} + g\sin\theta\right) \tag{D5}$$

Substituting equations D2 to D5 into D1 produces the basic differential structure of the elemental slice:

$$mv_s \frac{dv_s}{dS} = PA_s - \tau_s m \frac{v_s^2}{R} - \tau_s mg\cos\theta + mg\sin\theta \tag{D6}$$

Assuming that the elemental slice of material flow remains in a steady state condition and the motive pressure force acts solely in the 't' direction, then by applying conservation of mass, the following continuity relationship is used:

$$m = \rho_{fb} A_s s \tag{D7}$$

So dividing both sides by the mass and subsequent substitution of equation D7 into equation D6 gives:

$$v_s \frac{dv_s}{dS} = \frac{1}{\rho_{fb}} \frac{P}{S} - \tau_s \frac{v_s^2}{R} - \tau_s g\cos\theta + g\sin\theta \tag{D8}$$

Finally, assuming a constant pressure drop around each bend and straight section (including the appropriate bend factor *B*) as defined:

$$\frac{\Delta P}{\Delta S} \approx \frac{P}{S} = z \qquad (\textit{straight sections}) \tag{D9}$$

$$\frac{\Delta P}{\Delta S} \approx \frac{P}{S} = z(1+B) \qquad (\textit{for each bend}) \tag{D10}$$

Gives the differential form for the downward to horizontal bend:

$$v_s \frac{dv_s}{dS} = \frac{z(1+B)}{\rho_{fb}} - \lambda_e g\left(\frac{v_s^2}{Rg} + \sin\theta - \frac{\cos\theta}{\lambda_e}\right) \qquad (\textit{d-h bend}) \tag{D11}$$

Using a similar analysis, the differential equation for the other 4 bends and straight sections are defined in Equations D12 to D16 with a more detailed derivation of the differential equations shown in Appendix D.

$$v_s \frac{dv_s}{dS} = \frac{z(1+B)}{\rho_{fb}} - \lambda_e g\left(\frac{v_s^2}{Rg} + \cos\theta + \frac{\sin\theta}{\lambda_e}\right) \qquad (\textit{h-u bend}) \tag{D12}$$

$$v_s \frac{dv_s}{dS} = \frac{z(1+B)}{\rho_{fb}} - \lambda_e g\left(\frac{v_s^2}{Rg} + \sin\theta + \frac{\cos\theta}{\lambda_e}\right) \qquad (\textit{u-h bend}) \tag{D13}$$

$$v_s \frac{dv_s}{dS} = \frac{z(1+B)}{\rho_{fb}} - \lambda_e g\left(\frac{v_s^2}{Rg} + \cos\theta - \frac{\sin\theta}{\lambda_e}\right) \qquad (\textit{h-d bend}) \tag{D14}$$

$$v_s \frac{dv_s}{dS} = \frac{z(1+B)}{\rho_{fb}} - \lambda_e g\left(\frac{v_s^2}{Rg} + 1\right) \qquad (\textit{hor bend}) \tag{D15}$$

$$v_s \frac{dv_s}{dS} = \frac{z}{\rho_{fb}} - \lambda_e g\left(\frac{\sin\theta}{\lambda_e} + \cos\theta\right) \qquad (\textit{straight section}) \tag{D16}$$

# APPENDIX E

# Matlab scripts for solids flow velocity

### *Main Script*

The following MATLAB script determines the geometry of each pipeline segment and calls the relevant function and m.files which subsequently calculates the solids flow velocity

**pipe173mVR.m**

```
% This program represents the geometrical configuration of the 176m variable
% radius pipeline detailed in Chapter 3. The program calls two different
% m.files; 'straight.m' for the straight sections and 'bends.m' for the bend sections

global le pb g dp vo vai r D mstar ma ms P L dp_ds

% calls the global parameters m file
glob

% determine the initial velocity (initial assumption is that it is 90% of
% the initial superficial gas velocity)
vo=(0.9*vai)

% the first vertical straight pipe assumes initial velocity (vo) stays
% constant to start of bend for initial feeding of the system
s=[0:0.05:4.05];
v=s-s+vo;   % initialise matrix  v with size of displacement (s) along pipe
Le=4.05     % initialise pipe length

% Plotting the length and section orientation of the pipe where 'up' is a
% vertical up straight section
pipex=[0 0 s(end) s(end)];
pipey=[0 1 1 0];
fill(pipex,pipey,'w')
text(0,.5,'up')
hold on

% bend #1
bend='uh';      % bend orientation - upward to horizontal
r=0.065;        % bend radius of curvature (m)
bends           %  calling m file 'bends.m'

L=8.35-2*r;     % determining the actual straight length of pipe
straight='hor'; % straight pipe orientation (horizontal)
straights

% bend #2
bend='hd';      % horizontal to downward flow bend
r=0.065;
bends

% first downward drop
L=6.20-2*r;
straight='dro'; % downward flow straight pipe
straights

% bend #3
bend='dh';      % downward to horizontal flow
r=0.065;
```

```
% horizontal and bend sections
L=20.20-r-0.85;
straight='hor'; % horizontal straight pipe
straights
bend='h';       % horizontal to horizontal bend
r=0.85;
bends

L=14.86-r-1.0;
straight='hor';
straights
bend='h';
r=1.0;
bends

L=9.73-r-0.85;
straight='hor';
straights
bend='h';
r=0.85;
bends

L=14.70-r-1.0;
straight='hor';
straights
bend='h';
r=1.0;
bends

L=8.35-r-.85;
straight='hor';
straights
bend='h';
r=0.85;
bends

L=15.00-r-1.0;
straight='hor';
straights
bend='h';
r=1.0;
bends

L=18.06-r-0.85;
straight='hor';
straights
bend='h';
r=0.85;
bends

L=14.86-r-0.85;
straight='hor';
straights
bend='h';
r=0.85;
bends
```

```
L=24.66;-r-0.85
straight='hor';
straights
bend='h';
r=0.85;
bends

L=8.36-r-0.065;
straight='hor';
straights
bend='hu';      %horizontal to upward bend
r=0.065;
bends

L=6.35-2*r;
straight='upp'; %upward flow straight pipe
straights
bend='uh';      %upward to horizontal bend
r=0.065;
bends

L=2.65-r;
straight='hor';
straights
%end of pipeline

%put labels on graph
grid on
ylabel('solids velocity (m/s)')
xlabel('distance along pipeline (m)')
plot(s,v)
hold off
```

The m file which determines what type of straight section equation to use and calls the appropriate function

**straights.m**

```
% This program determines what type of straight pipe it is and calculates
% the velocity along the straight

% if block to determine the type of straight pipe
if straight=='hor'                    %horizontal flow
   [s1,vs]=ode45('horizontal',[0 L], vo);  %compute velocity up L

   % fill bottom of graph with letter for indication of straight pipe
   % orientation
   pipex=[s(end) s(end) s(end)+s1(end) s(end)+s1(end)];
   pipey=[0 1 1 0];
   fill(pipex,pipey,'w')
   text(s(end)+s1(end)/2,.5,'h')

elseif straight=='upp'                %vertical upward flow
   [s1,vs]=ode45('up',[0 L], vo);
   pipex=[s(end) s(end) s(end)+s1(end) s(end)+s1(end)];
   pipey=[0 1 1 0];
   fill(pipex,pipey,'w')
   text(s(end)+s1(end)/2,.5,'u')

elseif straight=='dro'                %vertical downward flow
   [s1,vs]=ode45('drop',[0 L], vo);
   pipex=[s(end) s(end) s(end)+s1(end) s(end)+s1(end)];
   pipey=[0 1 1 0];
   fill(pipex,pipey,'w')
   text(s(end)+s1(end)/2,.5,'d')

else ('error')
   disp('error in straight pipe orientation')
   exit
end

% re-initialising the end velocity of the pipe segment to be the initial
% velocity of the next computed segment
vo=vs(end);

% Build the pipe length displacement matrix (s), the material flow velocity
% matrix (v) and the scalar pipe length value (Le)
s=[s s(end)+s1'];
v=[v vs'];
Le=Le+L
```

The m file which determines what type of bend orientation equation to use and calls the appropriate function

**bends.m**

```
%this m file determines what type of bend it is and calculates the velocity
%around the bend

global vo r dpb

%if block for the 173m variable radius bends where the bend factor is 1.5
%for the short radius bends (r=0.053m) and bend factor is 0.5 for the long
%radius bends (r=0.85m and 1.0m)
if r<D*2
   dpb=dPb/(8*pi*r/2)
else
   dpb=dPb/(24*pi*r/2)
end

%if block to determine what type of bend orientation to compute the flow
%velocity
if bend=='hu'
   [s1,vs]=ode45('bend_hu',[0 r*pi/2], vo);
elseif bend=='uh'
   [s1,vs]=ode45('bend_uh',[0 r*pi/2], vo);
elseif bend=='hd'
   [s1,vs]=ode45('bend_hd',[0 r*pi/2], vo);
elseif bend=='dh'
   [s1,vs]=ode45('bend_dh',[0 r*pi/2], vo);
elseif bend=='h'
   [s1,vs]=ode45('bend_h',[0 r*pi/2], vo);
else ('error')
   disp('error in bend pipe orientation')
   exit
end

%re-initialising the end velocity of the pipe segment to be the initial
%velocity of the next computed segment
vo=vs(end);

%plot the segment section at the bottom of the graph with empty text
pipex=[s(end) s(end) s(end)+s1(end) s(end)+s1(end)];
pipey=[0 1 1 0];
fill(pipex,pipey,'w')
text(s(end),.5,' ')

%Build the pipe length displacement matrix (s), the material flow velocity
%matrix (v) and the scalar pipe length value (Le)
s=[s s(end)+s1'];
v=[v vs'];
Le=Le+r*pi/2
```

An example of the bend orientation function for downward to horizontal flow.

**bend_dh.m**

```
function dv=bend_dh(s,v)
% This function program uses differential equations defined in Chapter 6 to
% determine the differential velocity (dv) send the paramteric information
% of friction (le), radius (r), acceleration due to gravity (g) pressure
% drop per unit length (dp_ds) and pressure drop for a bend (dpb) for use by
% the Runge-Kutta Algorithm

% Global variables so they can be set and used outside m file
global le r dp_ds pb g dpb

%calling the friction equation m.file
friction

% The differential equation for the bend
% Note: the velocity solution is set to a minimum of 0.1 m/s to allow the
% program to run to the end of the pipeline so that the zero velocity point
% can be determined
dv=((dp_ds+dpb)/pb+g*cos(s/r)-le*max(v,0.1)^2/r-le*g*sin(s/r))/max(v,0.1);

return
```

The above function utilises the friction component m file

**friction.m**

```
% This program deteremines the frictional component (le) at a specific distance
% (s) along the pipeline and is dependant on the acceleration due to
% gravity (g), pipe diameter (D), solids loading ratio (mstar), the pressure
% drop per unit length (dp_ds), the initial (or inlet) air velocity (vai)
% and air density (rhoi) to  each pipe section after the pipe length
% distance (Le)

global g D mstar dp_ds P rhoi vai Le le C a b

rho=rhoi*(P-dp_ds*(Le+s))/P; %calculates the local air density

va=vai*rhoi/rho; %calculates the local superficial air velocity

fr=va/(g*D)^0.5; %calculates the local froude number (fr)

le=C/(fr^b*mstar^a); %friction factor equation defined in Chapter 5
```